



**Università degli Studi di Salerno**

Dipartimento di Ingegneria dell'Informazione, Ingegneria  
elettrica e matematica applicata

Dottorato di Ricerca in Ingegneria dell'Informazione  
XIII Ciclo – Nuova Serie

Tesi di dottorato

**Organic semiconductor material and device  
characterization by low-frequency noise  
and admittance spectroscopy of  
polymer:fullerene solar cells and  
silicon/organic thin film heterodiodes**

Candidato: **Giovanni Landi**

Tutor: **Prof. Dr. Heinrich C. Neitzert**  
Co-tutor: **Prof. Dr. Wolfgang R. Fahrner**  
Coordinatore: **Prof. Maurizio Longo**

Anno accademico 2014-2015



Submission date: June 23, 2014

Disputation date: August 28, 2014

Committee in charge:

Prof. Dr. Wolfgang R. Fahrner, University of Hagen, Germany

Prof. Dr. Heinrich C. Neitzert, University of Salerno, Italy



To my family



# CONTENTS

|   |           |
|---|-----------|
| <b>1. Introduction.....</b>   | <b>1</b>  |
| 1.1. Organic photovoltaics: state-of-the-art, future prospective and limits.....  | 1         |
| 1.2. Characterization of a new combination of quantum dots and carbon nanotubes as additive to polymer:fullerene solar cell.....  | 2         |
| 1.3. Recombination kinetics in the polymer:fullerene solar cells.....   | 3         |
| 1.4. Low frequency noise spectroscopy.....  | 4         |
| 1.5. Investigation of a new type of blue emitting organic material with ambipolar conduction.....   | 5         |
| <b>2. Impedance spectroscopy characterization of polymer:fullerene solar cells.....</b>   | <b>7</b>  |
| <b>3. Noise spectroscopy: a non-destructive technique for the characterization of transport properties and the thermal ageing of polymer:fullerene solar cells.....</b> | <b>11</b> |
| 3.1. Materials and methods.....   | 11        |
| 3.1.1. Solar cell preparation.....  | 11        |
| 3.1.2. Characterization techniques.....   | 12        |
| 3.1.3. AC modelling of polymer:fullerene solar cells for noise analysis.....  | 14        |
| 3.1.4. Electronic parameters extraction by noise spectroscopy.....  | 16        |
| 3.1.5. Charge carrier mobility measurements.....  | 19        |
| 3.1.6. Degradation experiments.....   | 20        |
| 3.2. Results and discussion.....  | 21        |
| 3.2.1. Characterization of polymer:fullerene solar cells by noise   |           |

|   |           |
|---|-----------|
| spectroscopy.....   | 21        |
| 3.2.2. Thermal ageing of polymer:fullerene solar cells investigated by electric noise analysis.....                         | 26        |
| 3.2.2.1 Electronic transport properties.....  | 26        |
| 3.2.2.2. Voltage-noise characterization.....  | 30        |
| 3.2.3. Investigation of the solvent influence on polymer:fullerene solar cells by low-frequency noise spectroscopy.....     | 36        |
| 3.3 Summary.....  | 40        |
| <b>4. Zn-complex based on ambipolar oxadiazole / carbazole structure: Synthesis, optical and electrical properties.....</b> | <b>43</b> |
| 4.1. Experimental.....  | 43        |
| 4.1.1. Materials and synthesis.....   | 43        |
| 4.1.2. Synthesis of 4-(4'-carbazol-9-yl-butoxy)-benzoic methylester (1).....  | 44        |
| 4.1.3.Synthesis of 4-(3-(9H-carbazol-9-yl-butoxy) benzohydrazide (2).....   | 44        |
| 4.1.4. Synthesis of 1-(4-(4'-carbazol-9-yl-butoxy)-benzoyl)-2-(2-methoxybenzoyl) hydrazine (3).....                         | 45        |
| 4.1.5.Synthesis of 9-(3-(4-(5-(2-methoxyphenyl)1,3,4-oxadiazol-2-yl)phenoxy)buthyl)-9H-carbazole (4).....                   | 45        |
| 4.1.6.Synthesis of 2-(5-(4-(3-(9H-carbazol-9-yl)butoxy)phenyl)-1,3,4-oxadiazol-2-yl)phenol (5): ligand OC.....              | 46        |
| 4.1.7.Synthesis of complex Zn(OC) <sub>2</sub> (6).....   | 46        |
| 4.2 Characterization techniques.....  | 47        |
| 4.2.1. Film preparation and structure characterization.....   | 48        |
| 4.2.2 Electronic device preparation and electrical  |           |



|   |           |
|---|-----------|
| Contents  | IX        |
| characterization.....   | 49        |
| 4.3. Results and discussion.....  | 49        |
| 4.3.1. Structural and thermal characterization.....   | 49        |
| 4.3.2. Optical characterization of solution and films.....  | 52        |
| 4.3.3. Current density-voltage analysis of silicon-organic layer<br>heterostructures.....                                     | 53        |
| 4.3.4. Electrical dc and ac characteristics.....  | 56        |
| 4.3.5. Comparison of the charge carrier mobility in-plane and<br>perpendicular to the organic film.....                       | 60        |
| 4.4. Summary.....   | 63        |
| <b>5. Investigation of the characteristics of a combination of<br/>InP/ZnS-quantum dots with MWCNTs in a PMMA matrix.....</b> | <b>65</b> |
| 5.1. Experimental details.....  | 65        |
| 5.1.1. Materials.....   | 65        |
| 5.1.2. Characterization.....  | 66        |
| 5.1.3. Substrate preparation.....   | 67        |
| 5.2. Results and discussion.....  | 67        |
| 5.2.1. Photoluminescence studies.....   | 67        |
| 5.2.2. Optical transmittance measurements.....  | 70        |
| 5.2.3. Electrical characterization of hetero-diodes with organic<br>emitter.....  | 77        |
| 5.3. Summary.....   | 79        |
| <b>6. Conclusions.....</b>  | <b>81</b> |
| <b>7. Bibliography.....</b>   | <b>83</b> |
| <b>8. List of publications.....</b>   | <b>95</b> |

**9. Acknowledgments.....99**  
**10. Curriculum vitae.....101**

## Abstract

The main focus of the present work is addressed to the field of organic electronics, which has attracted increasing interest for the development of flexible, large area and low cost electronic applications, from light emitting diodes to thin film transistors and solar cells. The present work describes initially, the application of low-frequency electronic noise spectroscopy for the characterization of organic electronic devices as an innovative and non-destructive technique. In particular the role of the modification induced by thermal stress on the electronic transport parameters under dark conditions of a bulk-heterojunction polymer solar cell have been investigated in detail.

The investigated organic solar cell is based on a blend between poly(3-hexylthiophene) (P3HT) and [6,6]-phenyl-C61-butyric acid methyl ester (PCBM), representing the classical reference structure regarding the polymer:fullerene type devices. Before the irreversible modification of the active layer, the solar cell has been modeled at low frequencies as a parallel connection between a fluctuating resistance  $R_X(t)$  and a capacitance  $C_X$ . Under dc biasing, the carriers injected into the active layer modify the equivalent electrical impedance thus changing the noise spectra. The experimental spectral trace can be interpreted by means of a theoretical model based on the capacitance  $C_\mu$ , which takes into account the excess of minority carriers in the blend, and the device resistance  $R_{rec}$ . The measured electric noise is of

1/f-type up to a cut-off frequency  $f_x$ , after which a  $1/f^3$  dependence has been observed. The analysis of  $f_x$  gives information regarding the recombination lifetime of the electrons in the active layer, while the voltage dependence of the  $C_\mu$  provides information about the density of states for the lowest unoccupied molecular orbital (LUMO) level in the PCBM material. Furthermore, the voltage fluctuations spectroscopy has been used to detect modifications of the active layer due to thermal stress. The temperature has been identified as one of the external parameters that can accelerate the parameter degradation. The analysis of the flicker and the thermal noise at low frequency reveals a decrease of the charge carrier zero-field mobility after a thermal cycle. This effect has been related to morphological changes of the solar cell active layer and the interface between the metal contact and the blend. Moreover, the influence of the solvent additives during the film preparation stage on the electronic transport in the solar cells has been studied by means of noise spectroscopy, and a detailed comparison of the optoelectronic properties of solar cells prepared with different blends has been made.

On one side, a P3HT/PCBM based bulk heterojunction solar cell is one of the most prominent candidates for a polymer solar cell, but on the other side, its conversion efficiency is limited by poor long-wavelength absorption. One way to increase the conversion efficiency is to modify the active layer absorption by the addition of materials, that increase the absorption of light in the red and infrared spectral region. One of the most promising materials for this task are inorganic quantum dots (QDs). In the present study we choose InP/ZnS quantum

dots with an emission peak wavelength of about 660 nm. Additionally we added multi-walled carbon nanotubes in order to favor charge carrier separation and enhance the lateral conduction of the films. The films have been deposited by spin-coating in a non-conducting polymer matrix (PMMA) in order to investigate the interplay between the quantum dots and the carbon nanotubes and their electrical conductivity independently of the future host material in the polymer solar cell. We kept the QD concentration constant and varied the concentration of the CNTs in the deposited films. The characterization of the film morphology by scanning electron microscopy imaging and of the optical properties by photoluminescence and transmittance measurements revealed a rather complex interplay between nanotubes and quantum dots. In particular we found a strong tendency of the nanotubes with high concentration of CNTs to agglomerate in spherical configuration. Electrical conductivity measurements in sandwich configuration enabled to verify the degree of increase of the sample conductivity by the nanotube addition. In particular the measurements in sandwich configuration, where the PMMA/CNT films have been deposited directly on top of a crystalline silicon substrate, revealed the formation of a Schottky-type diode and a monotonic decrease of the conduction inset voltage with increasing CNT content. In addition, the decrease in optical transmittance of the films with increasing CNT concentration is less pronounced, when QDs are added. The optical transmittance in a wavelength range between 380 nm and 800 nm of the composites could be expressed empirically as a simple second order polynomial function.

The penultimate part of the work contains the synthesis and the characterization by means of elemental and thermal analyses and infrared spectroscopy of a new type of small molecule,  $\text{Zn(OC)}_2$ , that has been synthesized by colleagues at Salerno University. Current-voltage measurements of  $\text{Ag/Zn(OC)}_2/\text{p-Si}$  and  $\text{Ag/Zn(OC)}_2/\text{n-Si}$  heterostructures, have been performed and compared to that of reference structures with the same metal contacts but without the insertion of the  $\text{Zn(OC)}_2$  layer. Good rectification behavior has been observed for both hetero-diodes, independent of the silicon substrate doping type, confirming that the metal-organic layer can act both as electron or hole-conductor.  $\text{Zn(OC)}_2$  complex displayed blue photoluminescence in solution and in film. Current-voltage characteristics and capacitance voltage measurements have been used for the determination of the organic layer dielectric and hole conduction parameters.

In addition, the small molecules is used as active layer in an organic diode and in an organic field effect transistor (OFET) in order to evaluate the charge carrier mobility as a function of the electric field orientation.

# Chapter 1

## Introduction

### 1.1. Organic photovoltaics: state-of-the-art, future prospective and limits

In the last few decades, conjugated polymers have emerged as a new class of semiconductors which combine unique optoelectronic properties and the key technological advantages of plastics [1], like for example solution processing at low temperature. They represent a promising alternative to the existing photovoltaic technology due to the low manufacturing cost, low material consumption, and thin film architecture [2–4].

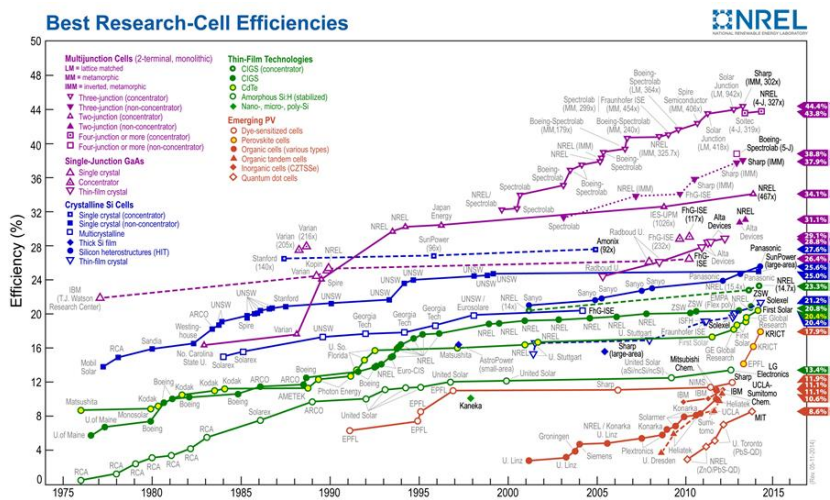
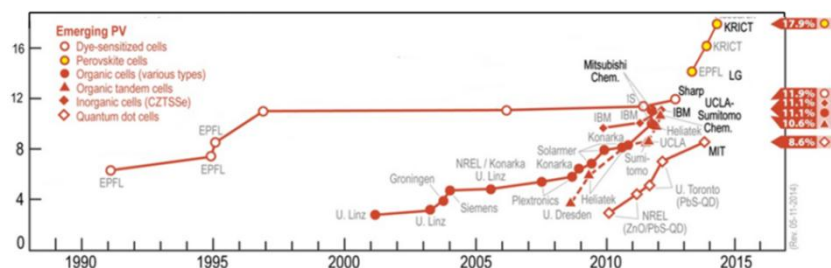


Fig.1. Illustration of the best research cell efficiencies as a function of time. (source: NREL).

Solar cells based on organic materials have already been reported in the late 70's, although with very poor conversion efficiencies. These early organic photovoltaic (OPV) devices were based on a single organic photovoltaic (OPV) device sandwiched between two electrodes, thus forming a Schottky diode. For a review of such devices, the reader is for

example referred to the work of G.A. Chamberlain in 1983 [5]. In 1986 Tang reported the first organic solar cell based on the donor-acceptor concept in a bilayer structure [6]. In the 90's, the introduction of the bulk heterojunction (BHJ) concept allowed enhancing the device efficiency to about 3% [7], marking a breakthrough in the field of OPV.



**Fig. 2.** Zoom into the emerging photovoltaics. (source: NREL).

In the BHJ, the active layer consists of an intermixing of the donor and acceptor materials so that a fine interpenetrating network builds up with extended donor-acceptor interfaces distributed in the bulk. The reference system in BHJ cells is represented by a composite between the conjugated polymer poly(3-hexylthio-phenylene) (P3HT) and [6,6]-phenyl-C61-butyric acid methyl ester (PCBM), a soluble derivative of the fullerene  $C_{60}$ . Solar cells based on P3HT:PCBM have demonstrated efficiencies of about 5% [8]. Recently, the highest efficiencies of organic solar cells has been recently reported with a value of 10.6% for small molecule based tandem cells [9], but polymer based solar cells with only slightly lower efficiencies of 9.1% have been reported as well [10], thanks to the development of new low-bandgap polymers that allow for better light harvesting [11] (as shown in Fig. 2).

## 1.2. Characterization of a new combination of quantum dots and carbon nanotubes as additive to polymer:fullerene solar cells

The maximum efficiency of this type of solar cell is limited by poor long wavelength absorption. One way to increase the conversion



efficiency of polymer solar cells is to modify the active layer absorption by the addition of materials that increase the light absorption in the red and infrared spectral region. One of the possibilities to achieve this goal is the addition of inorganic quantum dots (QDs) to the polymer active layer. The use of quantum dots gives the possibility to tune the absorption spectra by simply changing the quantum dot diameter [12-13]. Another advantage is their large surface-to-volume ratio, which leads to enhanced charge carrier transfer rates [14-15]. A possible measure to improve the efficiency regarding the charge carrier transport is the introduction of carbon nanotubes (CNTs) into the active layer. Solar cells, based on the combination of CdSe quantum dots (QDs) and P3HT have been reported with an efficiency of 2.1% and it has been shown that for the combination of the same type of QDs with a low-bandgap polymer, such as Poly[2,6-(4,4-bis-(2-ethylhexyl)-4H-cyclopenta[2,1-b;3,4-b']dithiophene)-alt-4,7(2,1,3-benzothiadiazole)] (PCPDTBT), a still higher efficiency of 2.7% can be obtained [16]. A combination of CdSe QDs and CNTs has been shown to facilitate exciton dissociation, however the reported device efficiencies, when combined in a poly(3-octylthiophene) (P3OT) based solar cell, were rather low [17]. Interesting results have been reported, when using PbS QDs combined with multi-walled carbon nanotubes in P3HT based solar cells [18]. In this latter case, due to the QD related enhanced absorption in the IR-region of the solar spectrum and the CNT enhanced efficient charge carrier transport to the contacts, a higher energy conversion efficiency as compared to the classical P3HT/PCBM reference cell has been measured.

### **1.3. Recombination kinetics in the polymer:fullerene solar cells**

Polymer–fullerene solar cells use a donor–acceptor mechanism to split excitons into free carriers [19]. In such devices, the most challenging aspect is to minimize the recombination between the electrons in the acceptor's lowest unoccupied molecular orbital (LUMO) and holes in the donor's highest occupied molecular orbital (HOMO). The principal loss mechanisms involve the breaking up of the exciton at the donor–acceptor interface, and the subsequent processes of

recombination and charge collection [20]. As recombination and transport in the active layer are influenced by the film ordering [21], one possible way to improve the efficiency of the bulk heterojunction solar cell is to control the nanoscale morphology of the blend. An optimization of the blend structure is also necessary to improve the charge carrier separation [22]. It is well known that the morphology of the active layer is very sensitive to the processing conditions, and strongly depends on the choice of solvent [23, 24] and possible additives [25].

#### **1.4. Low frequency noise spectroscopy**

For the development of advanced devices based on these complex materials, the multi-parameter process optimization, at present rather poor, is a fundamental requirement. In this respect, low-frequency electric noise analysis can be used to reveal possible strategies to lower the intrinsic noise generation. It has been used as a tool for non-destructive analysis of the transport processes in several systems, such as polymer/carbon nanotubes composites, [26] crystalline silicon solar cells, [27] and polymer-based light-emitting diodes (LED).[28] Conversely, there are few reports on noise measurements of polymer solar cells. Bag et al. [29] performed a noise analysis under illumination to evaluate light-induced degradation processes. However, fluctuation spectroscopy has never been used under dark conditions, where important information about defect states and their role as trapping or recombination centers can be obtained, without further degrading the material. Charged defects within the gap modify the electrical field profile in the active layer and might reduce the electrical field as driving force for the carrier transport. Consequently, an inefficient charge carrier collection at the contacts reduces drastically the solar cell performances.

The present work aims to study the noise properties of organic solar cells, not only providing a contribution to understand the electronic transport phenomena, but also being used as a powerful tool to optimize the processing conditions and to design novel photovoltaic devices.

## **1.5. Investigation of a new type of blue emitting organic material with ambipolar conduction**

While conventional semiconductor based photodiodes use the junction of differently doped semiconducting layers, in organic semiconducting devices, the electron and hole conducting species often coexist in a single active layer and the rectifying characteristics is mainly due to the different work functions of the injecting or collecting contact layers. The active layer is often fabricated by simply mixing the electron and hole conducting materials. This is for example the case in the BHJ organic solar cell concept, explained before. In this case, however, the final device characteristic is strongly dependent on the morphology of the active layer, that depends on a large variety of deposition parameters such as temperature, solvent type and concentration and donor/acceptor ratio. Often, further annealing steps after deposition are required and the annealing conditions strongly influence the device performance [30–32] and the active layer morphology [33]. Another approach, that results in a more reproducible active layer morphology, is the synthesis of small molecules containing electron as well as hole conducting groups chemically bound together [34]. Small molecule based thin films have a variety of applications in optoelectronics. Regarding electro-optic light emitting devices, for example, efficient blue emitting organic light emitting devices have been reported [34–36]. Up to few years ago, record efficiencies for organic photovoltaic devices were obtained by polymer based devices [37–42]. Today, however, high conversion efficiencies of organic solar cells are obtained using small molecule based devices [43–45]. Recently we showed the realization of UV sensitive photodiodes using carbazole and oxadiazole units in the same molecule [34,46–50], where the carbazole molecule is the hole-conducting and the oxadiazole the electron-conducting moiety. Heterodiodes are usually prepared by deposition of thin film organic semiconductors on top of classical inorganic semiconductors. This type of heterostructure - in particular when an inorganic semiconductor like crystalline silicon (c-Si) is used as inorganic substrate material - is a typical test structure for the determination of the electronic properties of the organic material [47]. Nevertheless, this kind of heterodiodes may also have practical applications such as

---

the preparation of polyaniline/c-Si heterodiode solar cells with high conversion efficiency [51], and also the fabrication of bistable memory devices operating at very low voltages has been reported [39]. Recently some complexes have been reported in which the Zn ligands contain both electron-donor and -acceptor moieties [52,53].

## Chapter 2

# Impedance spectroscopy characterization of polymer:fullerene solar cells

In this chapter, a brief description of the charge carrier recombination and diffusion processes in the frequency domain will be given.

In Fig. 1 the band diagram structure of the polymer:fullerene solar cell at different bias conditions is schematically shown. The band bending in Fig. 1a at the aluminum-blend interface is due to the p-doping of the P3HT, when exposed to air and/or moisture [54,55]. Under forward bias, the band bending at the cathode contact decreases, and at  $V = V_{bi}$  (built-in voltage) the depletion capacitance disappears. As a consequence, the electrons are injected into the LUMO level and recombine with the holes in the HOMO level. The diffusion and the recombination processes can be described by the distributed equivalent circuit, reported in Fig. 1c. The recombination kinetics can be described by the resistive element  $r_{rec}$ , the modulation of the stored excess of minority carriers gives origin to the distributed chemical capacitance,  $c_n$ , and the electron transport can be modelled by the  $r_t$ .  $R_S$  and  $C_g$  are the series resistance and the geometrical capacitance, respectively. The characteristic densities are  $10^{15}$ - $10^{17}$   $\text{cm}^{-3}$  and a depletion layer is formed at the contact. As mentioned before, the P3HT-aluminum contact shows a Schottky diode like behavior and the related Mott-Schottky curve, reported in Fig. 2a, exhibits a straight line which enables to determine the built-in-potential,  $V_{bi}$ , and the doping concentration,  $N_A$ . The corresponding values, extrapolated from the data, shown in Fig. 2a, are:  $V_{bi} = 0.43$  V and  $N_A = 3.5 \times 10^{16}$   $\text{cm}^{-3}$ . In Fig. 2b the measured capacitance at low frequency as a function of the bias voltage is shown. The injection of the charge carriers results in an increase of the device capacitance. Here, the contribution of the depletion capacitance disappears at  $V > V_{bi}$ . Fig. 3 shows the ac electrical impedance at different bias voltages. The experimental data are fitted, using the equivalent circuit model, reported in Fig. 1c. The typical semi-circles at low frequency are due

to the recombination processes in the active layer of the device under test, DUT.

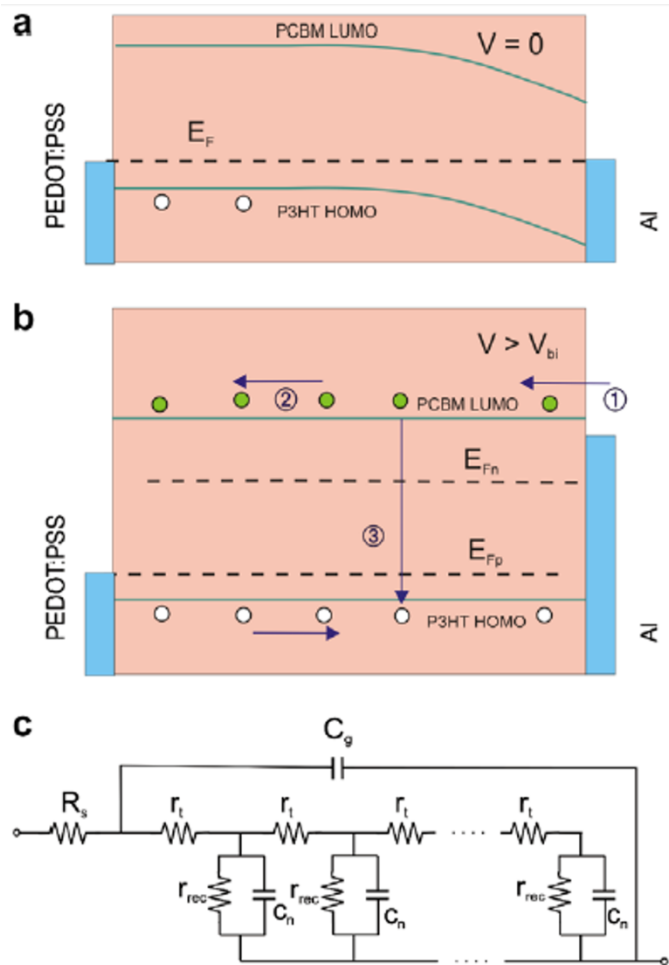


**Fig. 1.** (a) Band structure of the P3HT:PCBM heterojunction in equilibrium ( $V=0$ ). (b) Injection of the electrons (minority carriers) from the cathode into the LUMO level. The holes (majority carriers) populate the active layer. (c) Distributed equivalent circuit of the polymer:fullerene solar cell.  $C_g$  has to be assumed negligible. [56]

The corresponding time constant can be simplified as the product of the recombination resistance  $r_{rec}$  and the capacitance  $c_n$ , which gives the effective lifetime  $t_n = r_{rec} \times c_n$ . The values range between 0.8 and 0.2 ms for the polymer:fullerene solar cells.

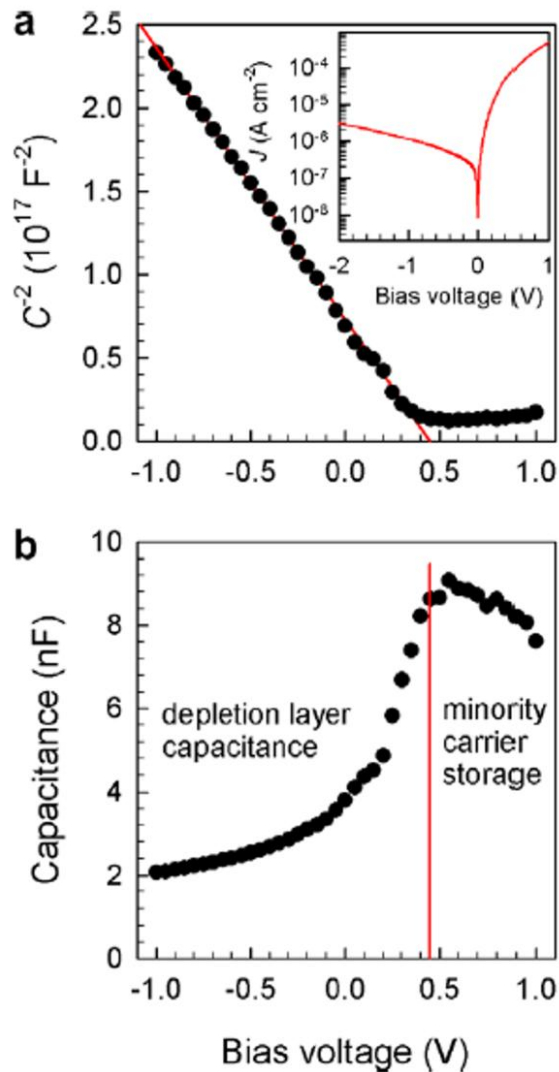


**Fig. 2.** (a) Mott-Schottky plot, measured at 100 Hz for a P3HT:PCBM solar cell. In inset the current density-voltage characteristics under dark conditions is given. (b) Capacitance as a function of the bias voltage, measured at 100 Hz. [56]

At high voltages, the dominant process is the diffusion of the electrons within the blend.

In conclusion, the equivalent circuit of the organic solar cell, as shown in Fig. 1c, cannot be directly used in the low-frequency noise analysis. Nevertheless, since the recombination processes occur at low frequencies, from the point of view of the generated noise, they can be

modelled as a simple parallel branch of the distributed capacitance and the recombination resistance. Furthermore, in order to extract the diffusion component of the charge carriers in the blend, a numerical integration procedure has to be performed on the voltage-spectral traces, as will be discussed later in Chapter 3.

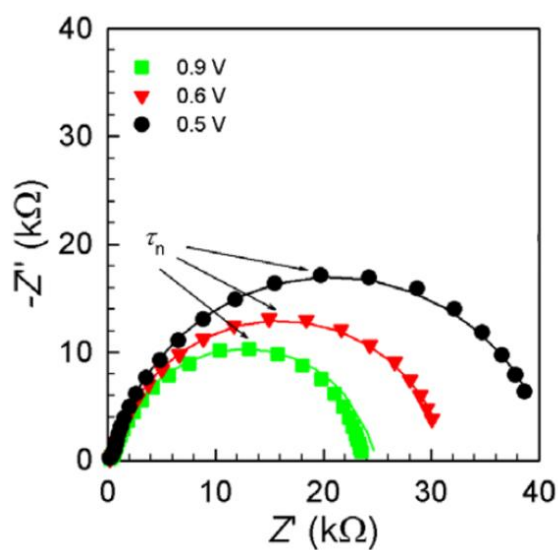


**Fig. 3.** (a) Impedance spectra, measured under dark conditions for different bias voltage values. Experimental points are fitted (full lines), using the equivalent circuit model, reported in Fig. 1a [56].



## Chapter 3

# Noise spectroscopy: a non-destructive technique for the characterization of transport properties and the thermal aging of polymer:fullerene solar cells

In this chapter, the first part contains the details of the sample preparation, a brief description of the setup used for characterization and the modelling aspects of the organic solar cell through the low frequency noise analysis are given. The second part contains a detailed electric noise investigation of polymer:fullerene solar cells, at 300 K and under dark conditions. The experimental noise results are interpreted in terms of a model taking into account the device capacitance and recombination resistance. Relevant parameters of the solar cells can be computed through fluctuation spectroscopy, and the results have been compared with those obtained by alternative techniques. In addition, the dynamic behavior of the charge carriers has been successfully monitored by studying the fluctuation mechanisms. The influence of the solvent additives addition during the film preparation stage has also been studied by means of noise spectroscopy, and a comparison between blends prepared with the reference solvent has been made.

### 3.1. Materials and methods

#### 3.1.1 Solar cell preparation

The reference blend was a mixture of poly(3-hexylthiophene) (P3HT) and [6,6]- phenyl-C61-butyric acid methyl ester (PCBM) dissolved in 1,2-dichlorobenzene (oDCB), a solvent in which P3HT and PCBM are both readily soluble. We used 1,2,3,4-tetrahydronaphthalene (THN), which has a higher boiling point (207 °C) than oDCB (180 °C) as solvent additive. PCBM is more soluble in THN than P3HT [58], and

the preparation of the solar cells with the solvent additive is therefore expected to allow for a better ordering of the polymer domains. P3HT and PCBM were dissolved in oDCB or in oDCB+THN in a 1:1 ratio in weight and stirred at 70°C overnight before use [59]. To fabricate the photovoltaic cells, indium tin oxide (ITO) coated glass slabs were patterned, etched in an HCl bath in order to define the anode area, and ultrasonicated several times in isopropyl alcohol. An oxygen plasma treatment was also performed in order to remove organic residues from the surface. Poly(3,4-ethylenedioxythiophene) (PEDOT) :poly(styrenesulfonate) (PSS) was then spun on top of the ITO and dried at 180 °C for 10 min in air. To complete the devices, the samples were transferred to a nitrogen filled glovebox where spin coating and thermal annealing (150 °C for 10 min) of the active layer (P3HT:PCBM), as well as cathode evaporation (Ca/Al) took place. The resulting device area is about 0.5 cm<sup>2</sup>, with four contact strips of length  $d = 12$  mm and width  $w = 4$  mm each. The top view of the sample and the cross section of a single strip are shown in Fig. 1a and Fig. 1b respectively.

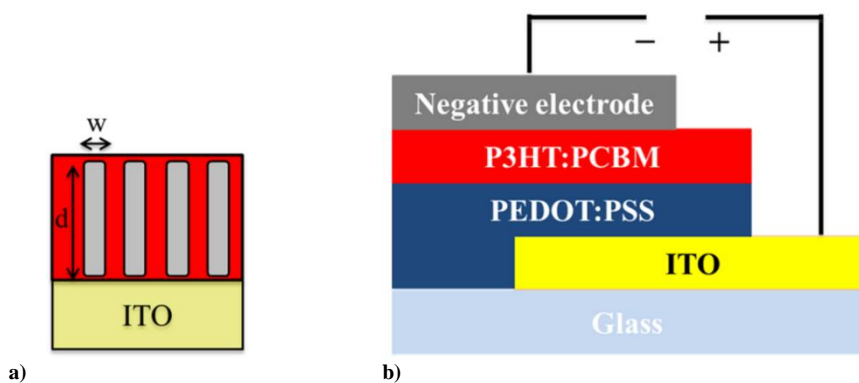


**Fig. 1.** Top view of the sample (a) and cross section of a single strip (b).

### 3.1.2 Characterization techniques

All the experimental investigations were carried out by using a thermoelectric cooler (i.e., Peltier device), with a temperature range of operation between 270 and 360 K. The temperature was stabilized with a computer-controlled PID loop to better than 0.1 K. The current-

voltage measurements were made in current-pulsed mode by using an active dc current source (model Keithley 220), and by recording the voltage response with a digital nanovoltmeter. The noise measurements have been made using a digital dc current source for the biasing of the samples, while the output voltage signal has been amplified by a low-noise preamplifier and subsequently analyzed using a HP35670A spectrum analyser, as shown in Fig. 2. The spectral density  $S_V$  has been measured in the frequency range 10 – 100000 Hz,

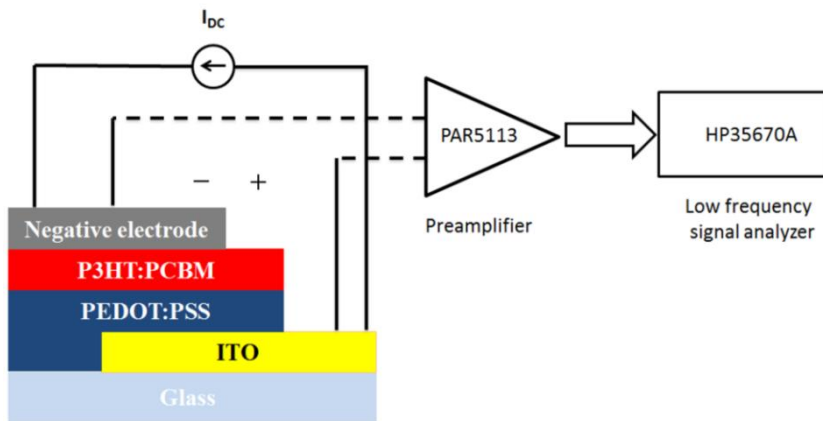


**Fig. 2.** Sketch of the noise measurement setup.

with an instrumental background noise  $C$  of  $1.4 \times 10^{-17} \text{ V}^2/\text{Hz}$ . All the measurements have been made in dark conditions at 300 K, by using a four-point probing bridge. The spectral density of the voltage fluctuations was calculated by averaging a large number ( $\geq 100$ ) of measured traces. The used standard four-probe technique, alone, does not eliminate completely the external noise contributions due to contact resistance fluctuations. In order to avoid the presence of spurious noise components in the real spectral trace of the samples, a specific experimental technique, based on a sequence of four-probe and two-probe noise measurements, was used to determine the contact noise contributions. The details of the experimental setup are reported in [60]. The photovoltaic performance under illumination was calculated from the current-voltage curves measured with a Keithley 4200 semiconductor characterization system. The standard reference spectrum AM 1.5G was provided by a class A solar simulator from

P.E.T. Inc. calibrated with a reference silicon solar cell from Fraunhofer ISE (Freiburg, Germany). The data were recorded on twin samples of the ones used for the degradation studies, in order to avoid the undesirable effect of the light exposure that is necessary for the current-voltage measurements.

### 3.1.3 AC modelling of polymer:fullerene solar cells for noise analysis

Several studies of the polymer solar cell admittance have shown that the ac electrical impedance can be modelled as an RC sub-circuit at low frequencies [61-63]. From the noise point of view, this circuit can be regarded as a parallel connection between a fluctuating resistance  $R_x(t)$  and the equivalent capacitance  $C_x$ , which is the sum of the geometrical capacitance  $C_g$  and the chemical capacitance  $C_\mu$ .  $C_g$  represents the dielectric contribution of the active layer and the hole transport layer (HTL) and consists in the series of two capacitances  $C_{Blend}$  and  $C_{Pedot:PSS}$ . The value computed from the device size is  $9.2 \text{ nF cm}^{-2}$ , in agreement with the value of  $10 \text{ nF cm}^{-2}$  reported in literature for a similar P3HT:PCBM solar cell [66]. In Fig. 3 the equivalent circuit of the noise measurement setup and of the device under test are shown. To enhance the current coupling with the solar cell, an input low pass filter formed by the resistance  $R_1$  and the capacitor  $C_1$  was inserted after the input bias current source, with a cut-off frequency of  $(2\pi R_1 C_1) = 1.5 \text{ Hz}$  to reduce externally generated noise. The effect of the  $R_t$  induces an increase of the time constant due to the recombination processes into the solar cell  $\tau_n' = C_g(R_t + R_{rec}) + C_\mu R_{rec}$ . Given that, the dielectric contribution of the organic layers is negligible, the resulting effective lifetime becomes  $\tau_n = C_\mu R_{rec}$ . As a consequence,  $C_g$  and  $R_t$  can be excluded from the impedance calculation. The ac equivalent noise impedance  $Z_n$ , in the Laplace domain ( $s = j\omega$ ), is the parallel connection between the equivalent impedance of the solar cell  $Z_x = R_s + R_x / (1 + j\omega C_\mu R_x)$  and the equivalent impedance of the input filter  $Z_1 = (1 + j\omega C_1 R_1) / j\omega C_1$ . The resulting  $Z_n$  can be expressed as:

$$\frac{1}{Z_n(s)} = \left[ \frac{s C_1}{1 + s C_1 R_1} + \frac{1 + s C_\mu R_x}{R_s (1 + s C_1 R_1) + R_x} \right]. \quad (1)$$

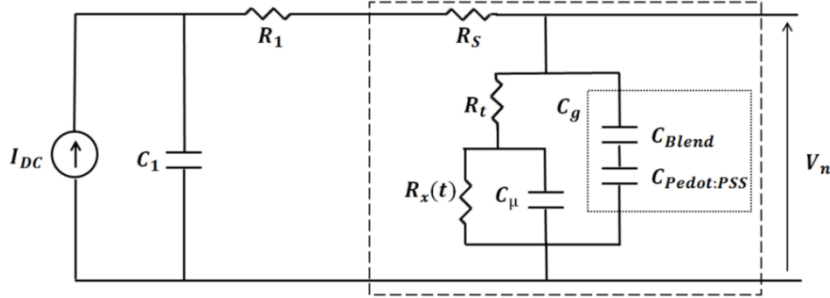


**Fig. 3.** The noise measurement setup with the sample equivalent circuit in a dashed box.

Given  $R_1 \gg R_S, R_x$ , in this case more than two orders of magnitude, from the point of view of the generated voltage noise  $V_n$  the whole circuit reduces to a parallel  $R_x C_\mu$  connection. The  $Z_n$  can be reduced to:

$$Z_n(s) = R_S + \frac{R_x}{1 + sC_\mu R_x}. \quad (2)$$

The resistance  $R_x$  can be expressed as a constant average value plus a small fluctuating random function:

$$R_x(t) = \langle R_x \rangle + \delta R_x. \quad (3)$$

The mean value corresponds to the recombination resistance  $R_{\text{rec}}$  of electrons and holes [64], defined as  $R_{\text{rec}} = (dV_F/dI_{\text{DC}})$ , where  $I_{\text{DC}}$  is the dc bias current and  $V_F = V_{\text{DC}} - I_{\text{DC}}R_S$  is the forward voltage without the contribution of the device series resistance  $R_S$  [65].

$$(\delta Z) = \left( \frac{\delta R_x}{1 + sC_\mu R_{\text{rec}}} \right) \quad (4)$$

Under dc current biasing, the fluctuations of  $R_x$  are the source of the voltage noise of the device. The spectral density results in:

$$S_Z = \frac{S_R}{1 + (\omega C_\mu R_{\text{rec}})^2}. \quad (5)$$

In the frequency domain this contribution is of 1/f-type, given by  $S_R(f) = \frac{K}{f^\gamma} R_{rec}^2$ . Here, K is the noise amplitude and  $\gamma$  is an exponent close to unity [67]. Being  $S_V(f) = S_Z I_{DC}^2$ , it is then straightforward to compute the expected voltage-spectral density, obtaining:

$$S_V(f) = \frac{K}{f^\gamma} \times \frac{(R_{rec} I_{DC})^2}{1 + \left(\frac{f}{f_x}\right)^2} + C. \quad (6)$$

In which the cut-off frequency is

$$f_x = \frac{1}{2\pi R_{rec} C_\mu}, \quad (7)$$

and C is the instrumental background noise of  $1.4 \times 10^{-17} \text{ V}^2/\text{Hz}$ . The equation (6) reveals a general trend of the voltage noise, that is, a 1/f dependence for frequencies below  $f_x$  and a  $1/f^3$  dependence at higher frequencies [68].  $C_\mu$  takes into account the excess minority carriers and increases as a function of  $V_F$  [56]. By forward biasing the devices, the injection of charge carriers produces a modification of  $R_{rec}$  and  $C_\mu$ , which influences the low-frequency electric noise spectrum.

### 3.1.4 Electronic parameters extraction by noise spectroscopy

One important point for the analysis of electronic properties of the active layer in polymer:fullerene solar cells is the relationship between the average electron density and the electrochemical potential.

The latter describes the population of electrons (holes) separately in the LUMO (HOMO) level, when their population is displaced from equilibrium, and therefore can be defined as a Fermi energy ( $E_F$ ). One of the methods for determination of density of states (DOS) is based on the measurement of the variation of the density of electrons (holes) caused by a variation of  $E_{Fn}$  ( $E_{Fp}$ ) [69]. We consider the simple system in which the energy of a state does not depend on Fermi potential, i.e. we neglect interactions between the electrons (holes) and with surrounding media [69]. At a given electronic state with energy E in

the LUMO level, the average occupancy is described by the Fermi–Dirac distribution function [69]

$$f(E - E_{Fn}) = \frac{1}{1 + e^{[(E - E_{Fn})/k_B T]}} \quad (8)$$

where  $k_B$  is the Boltzmann's constant and  $T$  is the temperature. In disordered organic semiconductors, the DOS is usually modelled with a Gaussian distribution [70]

$$g(E) = \frac{N}{\sqrt{2\pi}\sigma_n} e^{-\frac{(E - E_0)^2}{2\sigma_n^2}}, \quad (9)$$

where  $N$  is the total electron density per unit volume,  $E_0$  is the center of DOS, and  $\sigma_n$  is the disorder parameter.

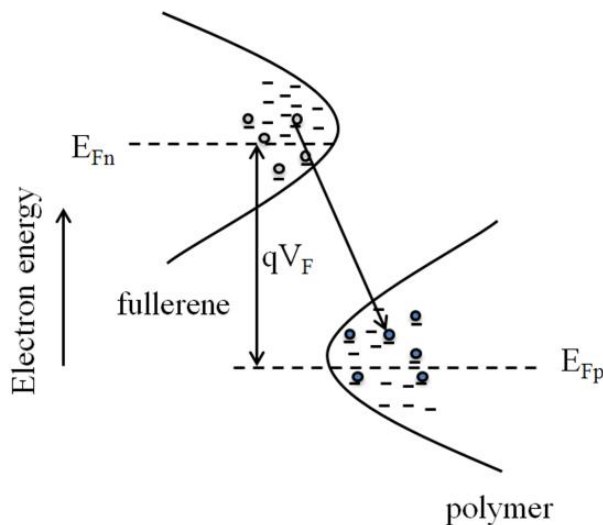


**Fig. 4.** Scheme of the electron density in the blend of the polymer:fullerene solar cell.

In Fig. 4 the energy scheme of the polymer:fullerene solar cell is shown.  $E_{Fn}$  is the Fermi level for the electrons in the fullerene material and  $E_{Fp}$  is the Fermi level for the holes in the polymer material. The splitting of the Fermi level is due to the external forward bias voltage  $qV_F = E_{Fn} - E_{Fp}$ , [64] where  $q$  is the elementary charge. The arrow

corresponds to the recombination event occurs between two localized states in the LUMO and HOMO levels, respectively.

When we consider the distribution of states  $g(E)$ , the chemical capacitance is obtained integrating all the contributions through the bandgap [69].

$$C_\mu = q^2 \int_{-\infty}^{+\infty} g(E) \frac{df}{dE_{Fn}} dE. \quad (10)$$

Using  $df(E - E_{Fn})/dE_{Fn} = -df(E - E_{Fn})/dE$  and integrating by parts, we arrive at

$$C_\mu = q^2 \int_{-\infty}^{+\infty} \frac{dg}{dE} f(E - E_{Fn})/dE. \quad (11)$$

Taking into account only the contribution of the occupied states,  $E \leq E_{Fn}$ , (i.e. by using the zero-temperature approximation of the Fermi function at occupancy  $>1\%$ ), the chemical capacitance follows the shape of the electron DOS and we obtain [69]

$$C_\mu = q^2 \int_{-\infty}^{E_{Fn}} \frac{dg}{dE} dE = q^2 g(E_{Fn}). \quad (12)$$

As shown in Fig. 4, a displacement of the  $E_{Fn}$  causes a variation of the states occupancy, as the Fermi level approaches the LUMO level, due to the bias voltage  $V_F$ , the electron density ( $n$ ) increases in the active layer. As a consequence, an enhancement of the related chemical capacitance  $C_\mu$  is induced. The electron density of the LUMO level can be described by  $n = n_0 e^{\left(\frac{E - E_{Fn}}{k_B T}\right)}$ , [64] hence,  $C_\mu$  takes an exponential growth behavior [71]:

$$C_\mu = dQ/dV_F \rightarrow C_\mu = -q \frac{dn}{dV_F} = q^2 \frac{dn}{dE_{Fn}} \rightarrow C_\mu = C_0 e^{\frac{qV_F}{k_B T}}. \quad (13)$$

On the other hand, also the current density ( $J$ ) of the solar cell measured in dark condition follow an exponential behavior

$$J = J_0 \left[ e^{\left(\frac{qV_F}{k_B T}\right)} - 1 \right]. \quad (14)$$



It is defined as recombination current in the  $\beta$ -recombination model [64]. Here  $\beta$  takes into account the deviation from the diode ideal equation (inverse of diode ideality factor). From the point of view of noise analysis, under bias current, the random fluctuation of the differential resistance  $R_X(t)$  generates the  $1/f$  type noise [66]. Therefore, the recombination resistance is defined from the recombination current derivative:

$$R_{rec} = \left( \frac{dJ}{dV_F} \right)^{-1} = \frac{k_B T}{q} \frac{1}{\beta} J^{-1}. \quad (15)$$

Since the  $R_{rec}$  depends by the inverse of the current density, it can be written as:

$$R_{rec} = R_0 e^{-\beta \frac{qV_F}{k_B T}}. \quad (16)$$

From equation (7), the recombination lifetime for the electrons in the PCBM material shows an exponential decay, being  $\alpha < \beta$  [71]

$$\tau_n = C_\mu R_{rec} = \tau_0 e^{\frac{qV_F}{k_B T}(\alpha - \beta)}. \quad (17)$$

### 3.1.5 Charge carrier mobility measurements

$S_V$  is characterized by the presence of two distinct noise components. The first, in the low-frequency region, is the "flicker noise"  $S_V^{flicker}$ , which is associated with the fluctuation of the electrical conductivity. It has an amplitude proportional to the energy gained by charge carriers from the electric field [66], when hopping transport is assumed as the conduction mechanism for OPV device. The second component, at high frequencies, is the "thermal noise"  $S_V^{thermal}$ , which is associated with the carrier interactions with the polymeric chains, taking into account the charge carrier energy loss due to the scattering processes [66]. The flicker noise has a frequency dependence, reproduced by modeling the photovoltaic device with a simple RC circuit as proposed in Eq. (6). The thermal noise, instead, is frequency independent and has the following expression [66]:

$$S_V^{thermal} = 4k_B T R_{resc} \quad (18)$$

For this purpose, voltage-noise allows to make a direct evaluation of the electron mobility  $\mu$  as [66,72–73]

$$\mu = \frac{S_V^{flicker}}{S_V^{thermal}} \times \frac{k_B T}{e \tau_n E^2} \quad (19)$$

where  $\tau_n = (2\pi f_x)^{-1} = R_{resc} C_\mu$  is the electron lifetime for the lowest unoccupied molecular orbital (LUMO) level in the PCBM material, and  $E = V_F/t$  is the applied electric field (being  $t = 255$  nm the active layer thickness). Therefore, the mobility values can be computed in Eq. (19) from the amplitude of flicker noise. The latter is obtained by integrating the spectral density curves over the whole frequency range where flicker noise appears, i.e., from 1 Hz to the intersection frequency with thermal noise.

### 3.1.6 Degradation experiments

One major weak point of OPV devices is the poor stability of the organic photoactive materials under operating conditions [74]. Most of the conjugated polymers rapidly degrade when exposed to ambient air and light, thus limiting the lifetime of the whole device. Indeed, it has been widely reported that degradation pathways, due to unstable morphologies, photo-oxidation, indium diffusion, and thermal stress occur at every layer and interface of OPV devices [75, 76]. In particular, temperature has been identified as one of the most important external parameters that can accelerate the degradation rate [74, 77]. Regarding P3HT, it is well-known that thermal annealing after active layer deposition can favour the formation of an ordered polymer phase [78, 79]. This ordering of the polymeric chains due to thermal treatment, however, makes P3HT more prone to oxidation. The temperature increase may induce phase separation between P3HT and PCBM, leading to an undesirable vertical structure which can drastically influence the solar cell performance [78, 79]. Degradation studies performed using Fourier transform infrared spectroscopy (FTIR), ultraviolet photo-electron spectroscopy (UPS), angle-resolved X-ray photoelectron spectroscopy (AR-XPS) have been reported in literature [80, 81]. However, these techniques, specific for the

structural characterization of the organic films and interfaces, need to be accompanied by complementary measurements that can provide additional information regarding the electronic transport in the material. In this respect, the study of the low-frequency electric noise spectrum has already proven to be a powerful and non-destructive spectroscopic analysis useful to investigate electric transport processes in several systems, such as manganites [82], novel superconductors [83], and graphene devices [84].

## 3.2. Results and discussion

### 3.2.1. Characterization of polymer:fullerene solar cells by noise spectroscopy

As reported in previous paragraph, the ac electrical impedance at low frequency of the polymer:fullerene solar cell can be modelled as a parallel connection between a dynamic resistance  $R_X(t)$  and an equivalent capacitance  $C_X$  [67]. The voltage-spectral noise generated by the device is related to the mean value of  $R_X(t)$ :  $R_{rec}=(dV_F/dI_{DC})$ , in which  $I_{DC}$  is the dc bias current and  $V_F=V-(R_S \cdot I_{DC})$  is the forward bias voltage without the effect of the device series resistance [65].  $V_F$  appears, under bias current, as a consequence of the splitting of the separate Fermi levels in the active layer. The 1/f-type noise generated by  $R_X(t)$  is modified by the effect of the parallel device capacitance  $C_X$  and the resulting noise spectra  $S_V$  can be modeled using the equation (6), where  $f_X=(2\pi R_{rec} C_X)^{-1}$  is a cut-off frequency, assuming negligible the dielectric contribution to the overall capacitance of the organic layers. The experimentally measured noise-spectral traces are shown in Fig. 5 for two different dc bias current values (0.01 mA and 0.05 mA, respectively) at a temperature of 300 K. The theoretical model of Eq. (6) (green dashed curves in Fig. 5) well describes the experimental data, once the instrumental background noise (curve (1) in Fig. 5) is taken into account. The small uncertainty associated, by the best fitting procedure, to the values of the parameters  $K=(1.4\pm 0.1)\times 10^{-9}$  and  $\gamma=(1.00\pm 0.02)$  confirms the original hypothesis, assuming a 1/f-type of noise spectral density. A similar noise spectrum has been reported for aluminium-polymer diodes, although characterized by

higher noise levels. Curve (2) in Fig. 5 has been recorded without biasing the device and represents the contribution due to resistance temperature fluctuations (Johnson noise).

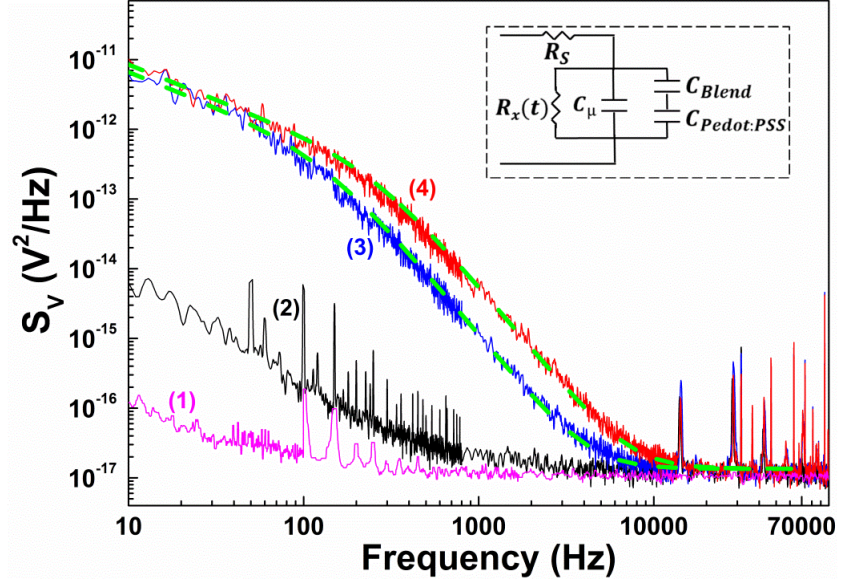


**Fig. 5.** Voltage-spectral traces measured at 300 K and at different forward bias current values. Curve (1) (magenta) is the system background noise, curve (2) (black) is for  $I_{DC}=0$  mA, curve (3) (blue) is for  $I_{DC}=0.01$  mA, and curve (4) (red) is for  $I_{DC}=0.05$  mA. Dashed green curves are the best fits of spectra (3) and (4) with Eq. (6). In the inset the solar cell equivalent circuit is shown.

For a standard resistance the Johnson noise should be frequency-independent and, in the case here investigated, should have a value of  $S_V = 4.2 \times 10^{-15} \text{ V}^2/\text{Hz}$ , being  $R = 250 \text{ K}\Omega$  the zero bias device resistance. At zero bias, P3HT:PCBM devices have an interface capacitance, whose value in this case is  $= 40 \text{ nF}$ , that is related to the intrinsic Schottky barrier at the cathode generated by the hole depletion [85]. The effect of such a capacitance is to introduce a cut-off frequency of  $\cong 10 \text{ Hz}$  above which the noise amplitude is strongly reduced. It is worth noting that a similar noise behavior has also been proposed in the case of tunnel junctions characterized by a frequency-independent loss tangent [86]. An additional feature of noise spectroscopy is the ability to determine physical parameters of the solar cells. Indeed, it allows to compute the values of  $f_X$  from which it is possible to derive  $C_X$ , once  $R_{rec}$  is known from the current-voltage

characteristics.

The chemical capacitance  $C_\mu$  can be extracted from  $C_X$ , being known the value of  $C_g$  [56]. The dependence of  $C_\mu$  on  $V_F$  is shown in Fig. 6. A monotonic increase is found, in agreement with results from literature [87]. The experimental dependence of  $R_{rec}$  on the forward voltage  $V_F$  is also shown in Fig. 6. A monotonic decrease is observed and compatible with that already reported in literature for similar solar cells but under illumination [87].

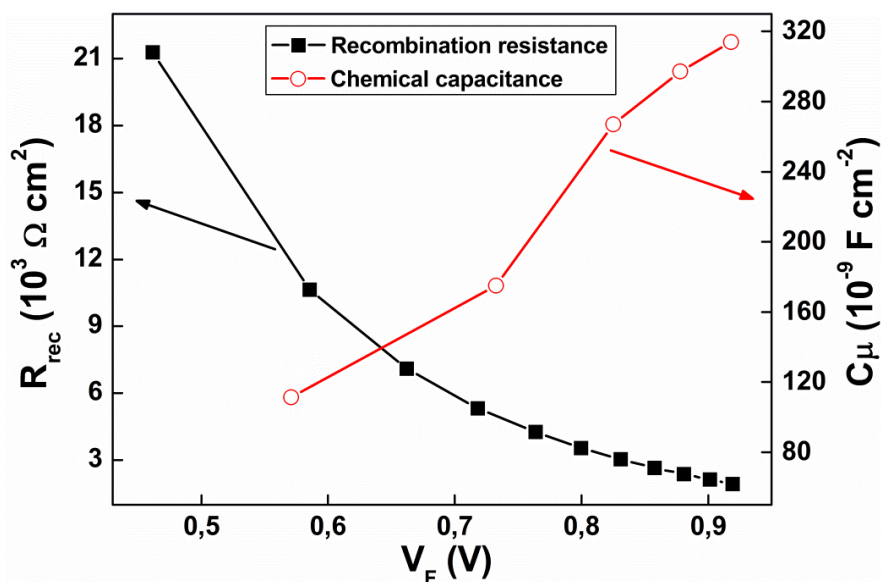


**Fig. 6.** Forward bias voltage dependence of  $R_{rec}$  (black full squares) and  $C_\mu$  (red open circles).

The change of  $R_{rec}$  and  $C_\mu$  is essentially due to the change of the storage of minority carriers in the active layer of the solar cell when increasing the forward voltage. This results in an enhancement of the cut-off frequency  $f_X$  with increasing bias current, visible in Fig. 5 in curves (3) and (4). The analysis of  $R_{rec}$  and  $C_\mu$  gives the possibility to evaluate the electronic density of states (DOS) at a given position of the electron Fermi level as  $g(E) = C_\mu t^{-1} e^{-2}$  (being  $t$  the active layer thickness and  $e$  the electron charge) and the electron lifetime  $\tau_n = R_{rec} \times C_\mu$  for the LUMO level in the PCBM material [61,87]. The experimental values of the DOS as a function of the applied bias

voltages are shown in Fig. 7.

In disordered organic semiconductors, the DOS is usually modelled with a Gaussian distribution [70]

$$g(E) = \frac{N}{\sqrt{2\pi}\sigma_n} \times \exp\left[-\frac{(E-E_0)^2}{2\sigma_n^2}\right] + g_0, \quad (20)$$

Here  $g_0$  represents the DOS background level. Its value has been determined to  $3.3 \times 10^{16} \text{ eV}^{-1} \text{ cm}^{-3}$  from the corresponding interface capacitance. The best fit to the experimental data using Eq. (20) is shown in Fig. 7 as solid curve. Although the higher energy states have not been experimentally investigated, a good agreement between experiment data and fit has been obtained. The fitting procedure with Eq. (20) gives the following results:  $N = (2.1 \pm 0.2) \times 10^{17} \text{ cm}^{-3}$ ,  $E_0 = (0.92 \pm 0.04) \text{ eV}$  and  $\sigma_n = (122 \pm 12) \text{ meV}$ . The value of  $\sigma_n$  is in good agreement with the one found for most semiconducting polymers (100 meV) [88].

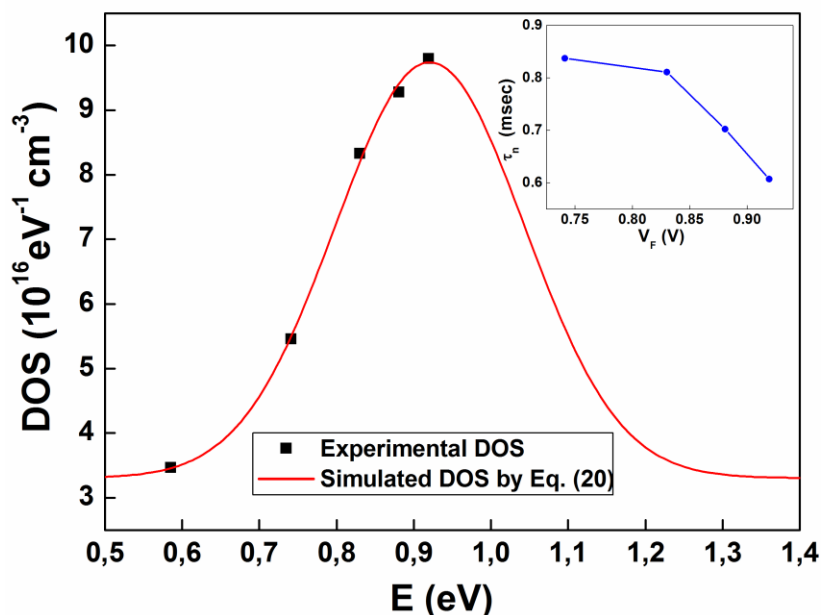


**Fig. 7.** Experimental DOS computed from noise measurements, shown as black full squares. The red solid curve is the best fit from Eq. (20). In the inset the experimental electron lifetime dependence on the forward voltage  $V_F$  is reported.

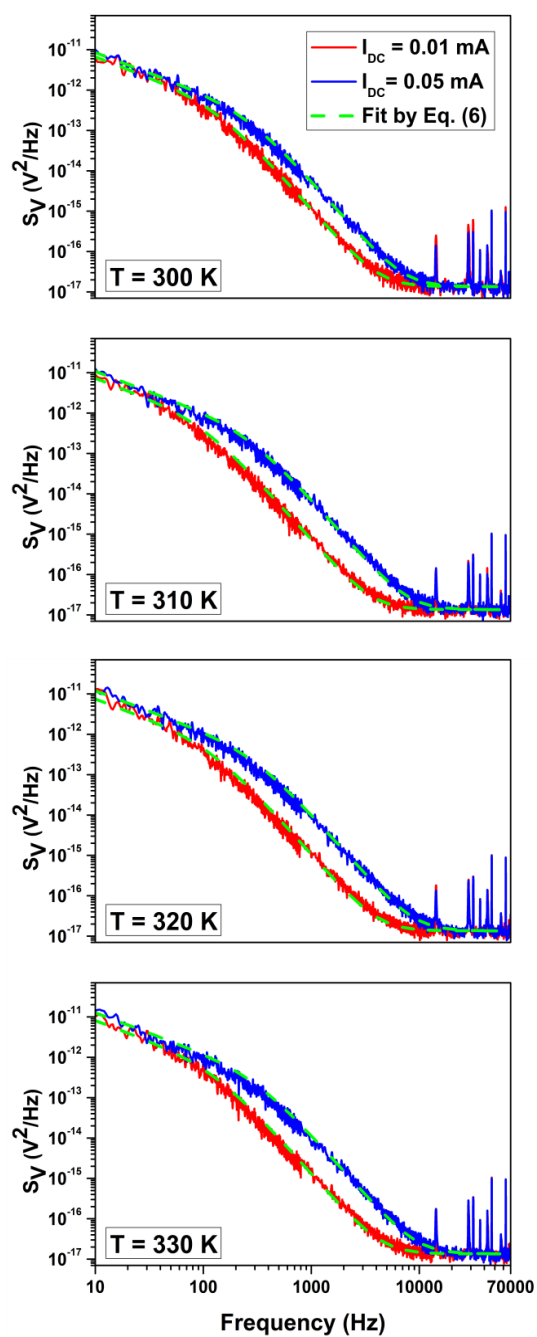


**Fig. 8.** Voltage-spectral traces measured from 300 K to 330 K with 10 K intervals and bias currents as in Fig. 5. Dashed green curves are the best fit with Eq. (6).

The total electron density is much lower than the expected value in the case of pure PCBM, i.e.,  $10^{20}$ - $10^{21}$  cm<sup>-3</sup>; however, it is similar to that found in P3HT:PCBM solar cells [89]. The Gaussian DOS center corresponds to half occupation of the electron DOS and is theoretically defined as  $E_g = E_{\text{LUMO}} - E_{\text{HOMO}}$ , whose value is usually reported to be 1.1 eV [19]. HOMO means the highest occupied molecular orbital. The observed difference between the expected theoretical value  $E_g$  and the experimental value  $E_0$  is due to the splitting of the Fermi levels in the blend for the DOS of PCBM (the LUMO level) and of P3HT (the HOMO level) and gives an estimate of the energetic level uncertainties.

In this case the difference is 0.18 eV, very close to the value of 0.2 eV, reported in literature for P3HT:PCBM blends [89-91]. Beside the DOS, also the electron lifetime dependence on  $V_F$  can be extracted from noise spectroscopy and is shown in the inset of Fig. 7. Its value ranges between 0.8 and 0.4 ms, decreasing as the bias increases [56]. Alternative methods to investigate charge carriers lifetime, such as impedance spectroscopy and photoinduced absorption, give similar values [92]. In Fig. 8 the voltage spectral traces measured at different current levels and in the temperature range of 300-330 K are reported. The model in Eq. (1) describes well also the temperature dependence of the spectral traces of the solar cell.

### **3.2.2 Thermal aging of polymer:fullerene solar cells investigated by electric noise analysis**

Electric noise measurements are sensitive to structural changes of the materials. Therefore, voltage-noise analysis has been performed before and after a thermal stress has been induced in the cell by increasing its temperature up to 340 K. It is well known that thermal treatments may produce a non-reversible modification of the blend morphology, with a consequent increase of the roughness at the interface between the cathode and the organic blend [93].

#### **3.2.2.1 Electronic transport properties**

Several studies of P3HT:PCBM photovoltaic devices have shown that these cells can be seen as Schottky diodes from the point of view of



the current transport [93–95]. Therefore, I-V curves can be modelled using the classical Schottky-Richardson emission law [96]:

$$I_{DC} = AA_R T^2 \exp\left(-\frac{\Delta}{k_B T}\right) \left[ \exp\left(\frac{eV_F}{nk_B T}\right) - 1 \right], \quad (21)$$

where  $A$  is the area of the cell active layer ( $0.5 \text{ cm}^2$  for the case here reported),  $A_R$  the effective Richardson constant,  $T$  the absolute temperature,  $\Delta$  the barrier energy at the metal-blend interface,  $n$  the ideality factor,  $e$  the electron charge and  $k_B$  the Boltzmann constant. The I-V characteristics of a typical P3HT:PCBM solar cell, investigated in this work, under dark conditions and at temperatures between 300 and 340 K, are shown in Fig. 9. A monotonic decrease of  $R_{\text{rec}}$  is found with increasing temperature (full symbols), whereas a modification occurring in the device active layer is clearly evident at 337 K. Indeed, the measurements performed after this 1st thermal cycle, and at the same temperatures (open symbols) as before, show a strong reduction of  $R_{\text{rec}}$ . Whether the event seen at 337 K represents an effective "breakdown" of the photovoltaic device is still an open question. The best fitting curves to the I-V experimental data (Fig. 9 solid lines) are obtained by using Eq. (21). The corresponding fitting parameters are reported in Table 1, where the first column refers to the time elapsed between subsequent measurements. On this short time scale, moisture and thermo-oxidation do not play a decisive role without light exposure [97, 98]. A strong reduction of  $R_S$  and  $n$  is found when the temperature of 337 K is approached. All these experimental evidences may be regarded as an increase of the solar cell electrical conduction, as a consequence of the heat treatment and the relative ordering of the P3HT polymeric chains [78, 79]. It is worth noting here, that before the heat treatment the twin devices, prepared within the same batch as the investigated ones, are characterized by the following parameters: short circuit current density ( $J_{\text{SC}} = (7.3 \pm 0.2) \text{ mAcm}^{-2}$ ), open circuit voltage ( $V_{\text{OC}} = (589 \pm 3) \text{ mV}$ ), fill factor ( $\text{FF} = (69 \pm 2)\%$ ), and power conversion efficiency ( $\eta = (3.0 \pm 0.2)\%$ ). These parameters have not been measured after the thermal cycle, since their temperature dependence is largely reported in literature [74, 77], and in this work the interest is more focused on the material rather than the final device. However, the clear enhancement of the barrier height  $\Delta$ , shown in Fig. 10,

indicates that a degradation occurred at 337 K. This becomes more evident after the subsequent cooling of the devices to room temperature. The  $\Delta$  values are computed assuming  $A_R = 120 \text{ A cm}^{-2} \text{ K}^{-2}$  for free electrons [96]. An estimation of the Richardson constant value of about  $10.4 \text{ A cm}^{-2} \text{ K}^{-2}$  has been reported in the case of polymer:fullerene solar cells [99], that would result in a change of  $\Delta$  of less than 2%. It has been already observed that thermal stress may induce a non-reversible modification of the blend morphology, with a consequent increase of the roughness at the interface between the cathode and the organic blend [94]. Accordingly, the metal atoms may diffuse into the active layer and react with the blend, thus generating an interface dipole layer which directly gives origin to the band discontinuity  $\Delta$ .

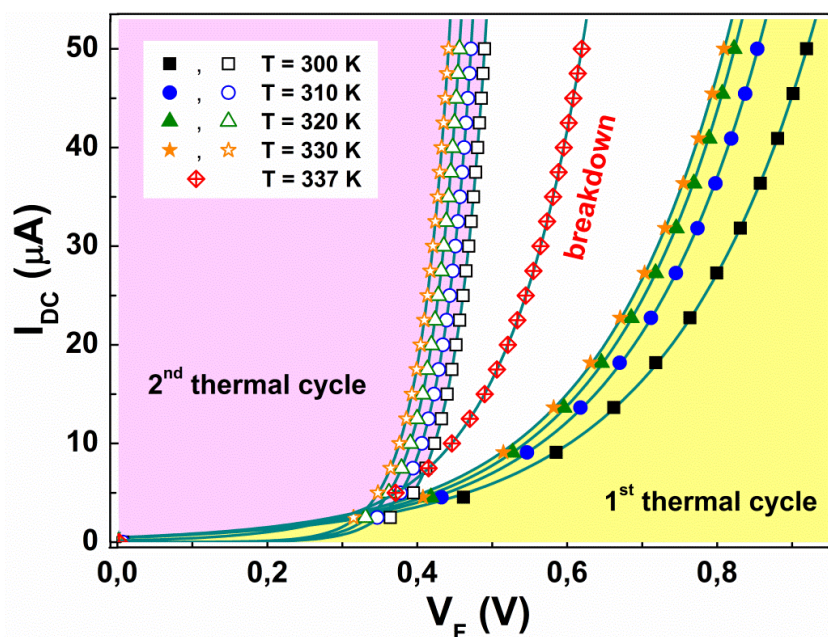


**Fig. 9.** Current-voltage characteristics of a typical device during the 1st (full symbols - yellow region) and the 2nd (open symbols - pink region) thermal cycles, respectively. A "breakdown", characterized by an active layer modification, occurs at 337 K. The best fitting curves with Eq. (21) are also shown as solid lines.

Therefore, the chemical interaction is not anymore negligible and has to be modeled by a specific interfacial density of states (IDOS). The dipole layer exhibits a negative charge on the organic side, which is

**Table 1**

Best fitting values of the parameters in Eq. (21), monitored in time and temperature. The Richardson constant  $A_R$  is fixed to a value of  $120 \text{ A cm}^{-2} \text{ K}^{-2}$ .

| Time (min) | T (K) | $R_S$ ( $\Omega$ ) | n                 | $\Delta$ (meV) |
|------------|-------|--------------------|-------------------|----------------|
| 0          | 300   | $3340 \pm 67$      | $7.62 \pm 0.04$   | $776 \pm 5$    |
| 10         | 310   | $3027 \pm 60$      | $6.74 \pm 0.04$   | $807 \pm 5$    |
| 20         | 320   | $3134 \pm 63$      | $6.27 \pm 0.04$   | $837 \pm 5$    |
| 30         | 330   | $2871 \pm 57$      | $6.12 \pm 0.03$   | $859 \pm 5$    |
| 40         | 337   | $2670 \pm 53$      | $3.709 \pm 0.003$ | $911 \pm 8$    |
| 50         | 300   | $453 \pm 9$        | $1.604 \pm .001$  | $962 \pm 6$    |
| 60         | 310   | $376 \pm 7$        | $1.534 \pm .001$  | $987 \pm 6$    |
| 70         | 320   | $308 \pm 6$        | $1.482 \pm .001$  | $1011 \pm 7$   |
| 80         | 330   | $263 \pm 5$        | $1.435 \pm .002$  | $1035 \pm 7$   |

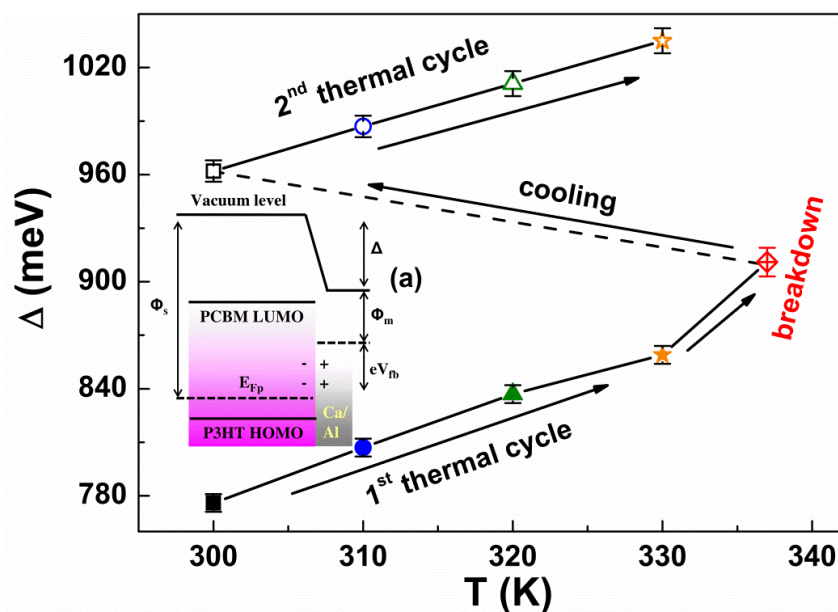


**Fig. 10.** Temperature dependence of the band discontinuity  $\Delta$  at the interface between the metal contact and the blend. The full and open symbols refer to the 1st and the 2nd thermal cycles, respectively. The energy levels of the organic materials (P3HT:PCBM) and cathode metals (Ca/Al) are shown in inset (a). Here,  $\Phi_S = 4.7 \text{ eV}$  and  $\Phi_m = 3.6 \text{ eV}$  are the blend- and metal- work functions, respectively, while  $V_{fb}$  is the flat-band voltage.

compensated by a positive charge at the metal contact [68], see inset (a) in Fig. 10. The modifications of the P3HT:PCBM blend, as a consequence of a thermal stress, are evidenced by the dc current transport analysis. However, more intrinsic properties of the solar cell, such as the charge carrier mobility, are difficult to extract with dc current transport measurements under dark conditions.

The noise level change with temperature is an effective probe for the monitoring of electronic device degradation phenomena, giving the possibility to evaluate specific parameters of the photovoltaic device during different thermal cycles [67].

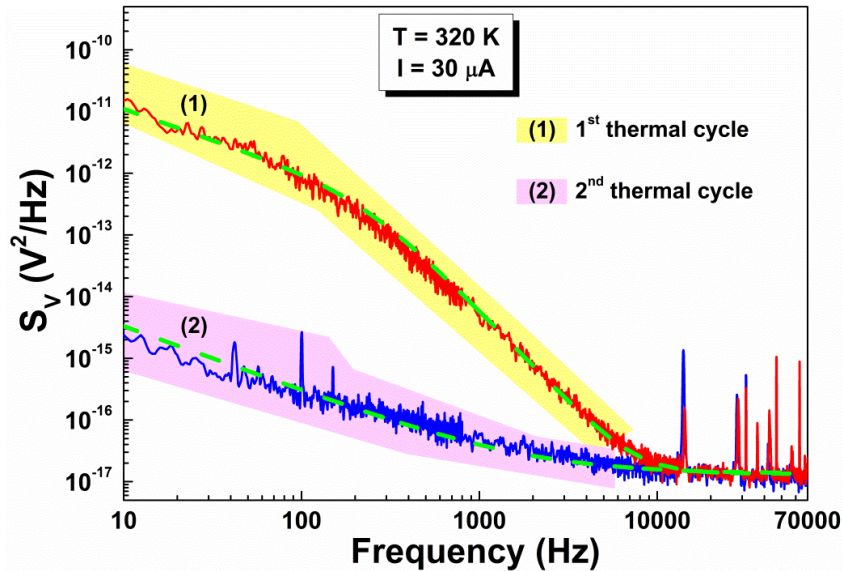
### 3.2.2.2 Voltage-noise characterization

Fig. 7 shows the typical voltage-spectral density  $S_V$  of voltage fluctuations processes in P3HT:PCBM solar cell as a function of the frequency, at fixed temperature (320 K) and bias current (30  $\mu$ A) values. The spectral shape is different when the electric noise is measured during the 1st thermal cycle (trace (1) in Fig. 11) and the 2nd thermal cycle (trace (2) in Fig. 11). This is reflected in the noise voltage-spectral density as a shift of  $f_X$  to frequencies higher than 100 kHz, above the experimental bandwidth. As a consequence,  $S_V$  has only the  $1/f$  component in the whole investigated frequency range and:

$$S_V(f) = \frac{K'}{f^{\gamma'}} \times (R'_{rec} I_{DC})^2 + C, \quad (22)$$

where  $K'$  and  $\gamma'$  are fitting parameters and  $R'_{rec}$  is experimentally evaluated from the current-voltage characteristics after the thermal treatment. In the same figure, the curves of the best fit with Eqs. (6,22) are shown as dashed green lines. In both cases, however,  $S_V$  is characterized by the presence of two distinct noise components. The first, in the low-frequency region, is the "flicker noise"  $S_V^{flicker}$ . The second component, at high frequencies, is the "thermal noise"  $S_V^{thermal}$  which is frequency independent and has the following expression [66]:

$$S_V^{thermal} = 4k_B T R_{rec}. \quad (23)$$



**Fig. 11.** Frequency dependence of the voltage-spectral density, at a fixed temperature (320 K) and bias current (30  $\mu\text{A}$ ), during the 1st thermal cycle, trace (1), and the 2nd thermal cycle, trace (2). The best fitting curves, obtained by using Eqs. (6) and (22) and by taking into account the instrumental background noise, are shown as dashed green lines.

By combining Eqs. (6,22) and (23), once the instrumental background noise  $C$  is taken into account, the best fitting curves to the experimental noise-spectral traces are obtained and shown in Fig. 11 as green dashed lines. Only a  $1/f$  component is visible in the spectra of the 2nd thermal cycle, due to the shift of  $f_x$  to frequencies higher than 100 kHz. This is above the experimental bandwidth and a direct consequence of the strong  $R_{\text{rec}}$  reduction [66]. The noise level  $K$  is extracted by fitting the measured voltage-noise, and is shown in Fig. 12 as a function of the time elapsed between subsequent measurements and the temperature, whose range is fixed to values lower than 380 K (the temperature usually used for annealing processes) in order to study the slow dynamics of the blend modification. This type of monitoring reveals the existence of a noise peak at 337 K and a strong decrease of  $K$  (more than two orders of magnitude), when cooling the devices subsequently down to room temperature. Fig. 12 clearly shows again that a non-reversible process took place within the active layer of the solar cell, between the 1st and the 2nd thermal cycles. Since the experiment is performed under dark

conditions, the photovoltaic performance of the devices can be estimated from the transport parameters, in order to understand the characteristic mechanisms driven by temperature and their time evolution in the BHJ structure.

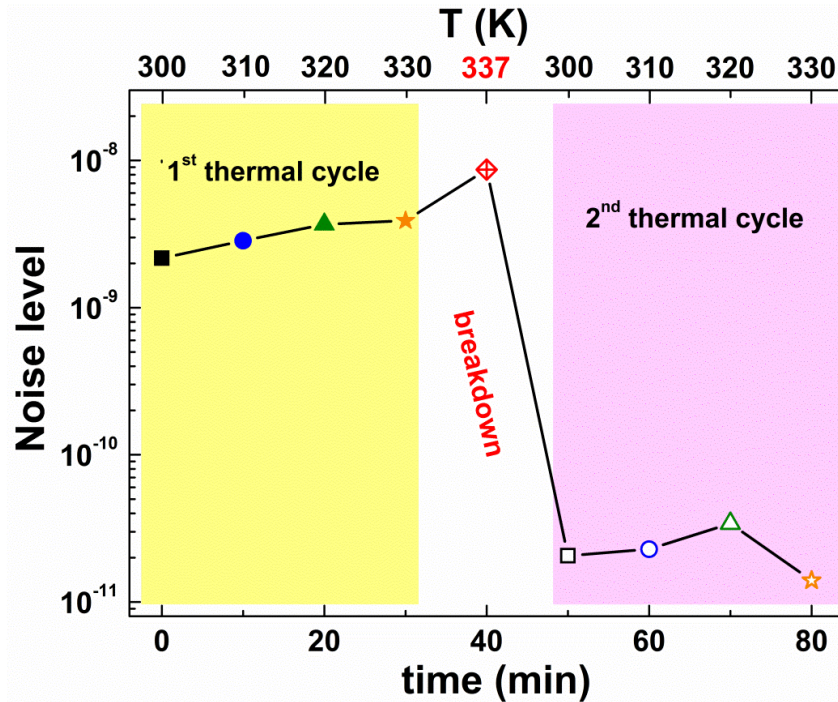


**Fig. 12.** Noise level evolution in temperature (top x axis) and time (bottom x axis). A noise peak is visible at the breakdown (337 K), while a strong noise reduction is observed in the 2nd thermal cycle.

For this purpose, voltage-noise allows to make a direct evaluation of the electron mobility  $\mu$  as [72-73] described in Eq. (19). The mobility values is obtained by integrating the spectral density curves over the whole frequency range where flicker noise appears, i.e., from 1 Hz to the intersection frequency with the thermal noise. A marked reduction of the electron mobility is clearly seen in Fig. 13, between the 1st and the 2nd thermal cycles. This is the direct consequence of the noise level reduction observed in Fig. 12, and gives a strong indication on the occurrence of degradation phenomena in the solar cell. A low charge carrier mobility detrimentally affects the power conversion

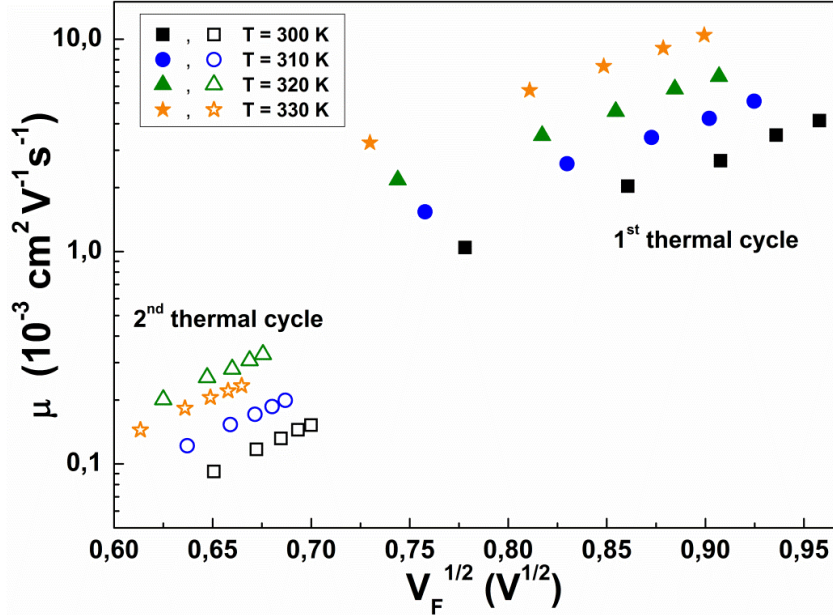


**Fig. 13.** Electron mobility, extracted by noise analysis, as a function of the square root of the forward voltage. A clear reduction of the mobility is evident between the 1st and the 2nd thermal cycles, while an exponential dependence on  $V_F^{1/2}$  is observed at all investigated temperatures.

efficiency of the devices. Moreover, Fig. 13 (note the logarithmic ordinate axis) shows an evident exponential  $\mu$ -dependence on  $V_F^{1/2}$ . This behavior is usually interpreted in terms of the Poole-Frenkel-type effect [96] as:

$$\mu = \mu_0 \exp \left[ \frac{e^{3/2}}{2k_B} \left( \frac{E}{\pi \epsilon_0 \epsilon_r} \right)^{1/2} \frac{1}{T_{eff}} \right], \quad (25)$$

where  $\mu_0$  is the zero-field mobility,  $\epsilon_0$  is the vacuum permittivity,  $\epsilon_r \approx 3$  the dielectric constant for P3HT:PCBM [56], and  $T_{eff}^{-1} = T^{-1} - T_{Gill}^{-1}$ , being  $T_{Gill}$  the temperature at which the mobility is independent of the electric field. The same framework of Eq. (25) has been extensively applied to describe the electric transport in P3HT diodes [100], in fullerene diodes and field effect transistors [101], and recently also in OPV cells [102]. There are only two fitting parameters in Eq. (25),  $\mu_0$  and  $T_{Gill}$ , whose temperature and time evolution is shown in Fig. 14. The value of  $\mu_0$  (left y axis in Fig. 14), extracted by

noise measurements on the pristine devices, is  $(2.68 \pm 0.09) \times 10^{-6} \text{ cm}^2 \text{ V}^{-1} \text{ s}^{-1}$ , very close to the value of  $2.3 \times 10^{-6} \text{ cm}^2 \text{ V}^{-1} \text{ s}^{-1}$ , reported by charge extraction with linearly increasing voltage (CELIV) measurements on similar samples [59]. An increase of  $\mu_0$  with temperature during a single thermal cycle is also observed and attributed to thermal activated processes. However, between the 1st and the 2nd heat treatments the zero-field mobility is reduced of less than two orders of magnitude. The same reduction is obtained by performing thermal annealing, which is usually considered as responsible of the electron mobility decrease by interrupting the conjugated structure of C<sub>60</sub> [103]. This indicates, again, that a device degradation can be induced by thermal stress. The simultaneous sensible increase of  $E_{GIII} = k_B T_{GIII}$  (right axis in Fig. 14) gives a further confirmation of the occurrence of a non-reversible active layer and interface modification between the two thermal treatments. In terms of the morphological model of P3HT:PCBM blends proposed by Tsoi and coworkers [79], the role played by temperature is to favor the ordering of P3HT chains. This effect is resulting in the reduction of the device series resistance and recombination resistance, between the different thermal cycles, as observed with dc current transport measurements. However, this reduction alone does not explain the overall noise level decrease in the 2nd thermal cycle. As a matter of fact, it has been widely demonstrated that crystallization of P3HT, induced by simple thermal annealing, makes P3HT molecules more susceptible to oxidation. Moreover, the ordering induces a vertical phase separation between P3HT and PCBM molecules, pushing PCBM further away from the film-metal interface. This leads to an undesirable vertical gradient with a nearly pure P3HT layer at the film-metal interface [79, 104]. Here, the vertical phase separation between P3HT and PCBM molecules is detected with voltage-noise analysis. For the devices, investigated in this work, a noise level peak is observed at 337 K, that is the temperature at which the crystallization process of P3HT is completed. The non-reversible morphological modification of the solar cell active layer after the cooling down to room temperature, as indicated by the increasing values of  $E_{GIII}$ , produces a change in the conventional transport mechanism of P3HT:PCBM.



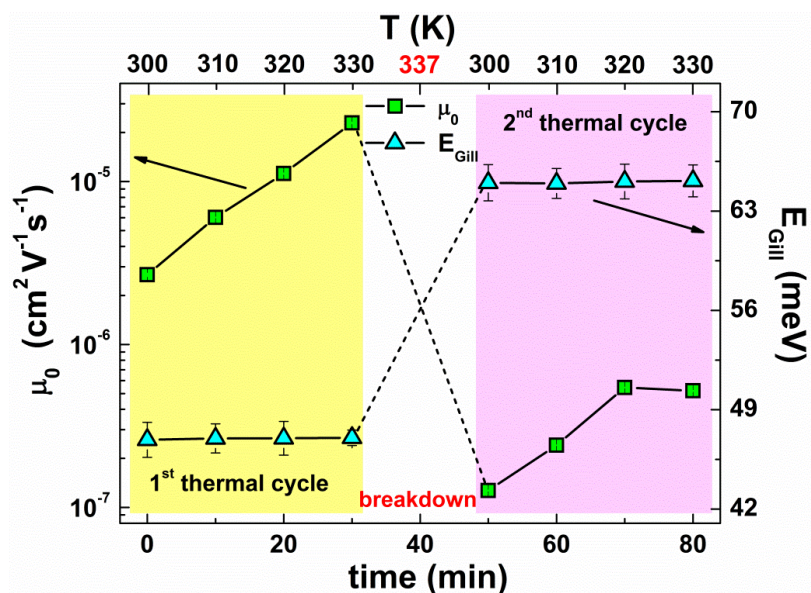


**Fig. 14.** Temperature and time evolutions of the zero-field mobility (left y axis) and of the Gill's energy (right y axis). Modifications of the transport properties of P3HT:PCBM solar cells are observed as the direct consequence of the thermal aging.

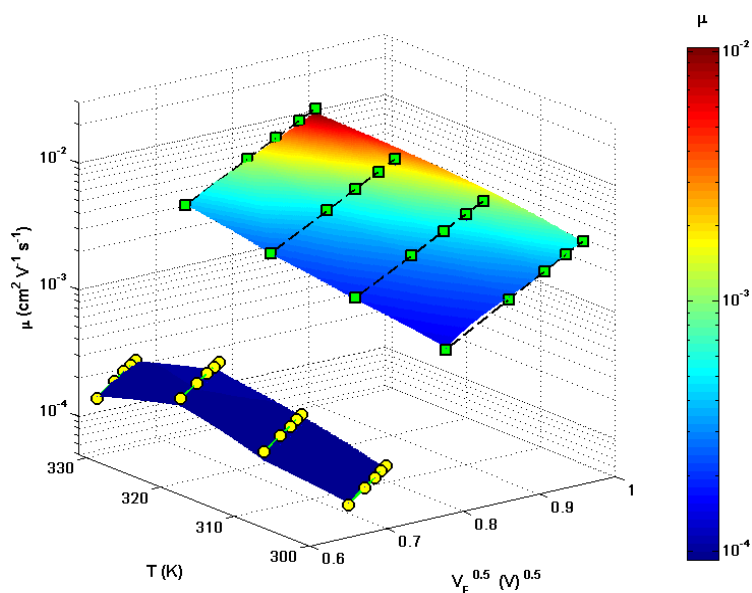


**Fig. 15.** Electron mobility as function of the temperature and bias forward voltage, computed through the flicker noise analysis, in the bulk heterojunction polymer:fullerene solar cells exposed to thermal stress.

In particular, an increase of the hopping energy barrier between the two nearest delocalized sites occurs, thus limiting the electron mobility to lower values. This is experimentally observed during the 2nd thermal cycle. The simultaneous reduction of the recombination resistance and the mobility is compatible with the strong noise level reduction, found after thermal annealing. It is shown that noise spectroscopy is a powerful experimental technique, very sensitive to degradation phenomena occurring in the OPV devices.

### 3.2.3 Investigation of the solvent influence on polymer-fullerene solar cells by low-frequency noise spectroscopy

The current density-voltage (J-V) characteristics of the solar cells under AM 1.5 illumination prepared with the oDCB reference solvent and oDCB + THN mixture solvent are shown in Fig. 16.

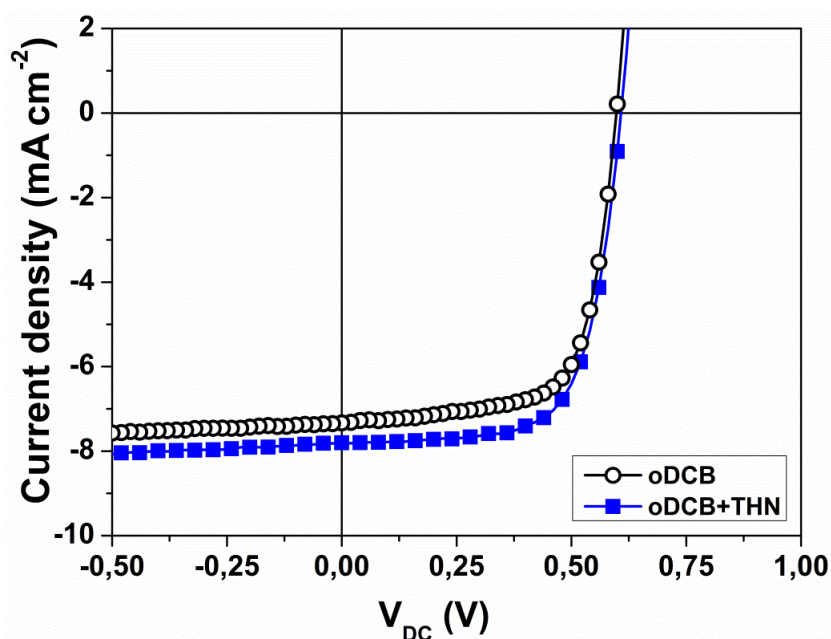


**Fig. 16.** Illuminated current–voltage characteristics of solar cells with active layers prepared using the solvents oDCB (open circles) and oDCB + THN (full squares).

The computed parameters for the oDCB-based devices are: short circuit current density ( $J_{SC}$ )  $\approx 7.3$  mA cm<sup>-2</sup>; open circuit voltage ( $V_{OC}$ )

$\approx 0.58$  V; fill factor (FF)  $\approx 69\%$ ; and power conversion efficiency ( $\eta$ )  $\approx 2.92\%$ . The same parameters for oDCB + THN are:  $J_{SC} \approx 7.8$  mA  $\text{cm}^{-2}$ ,  $V_{OC} \approx 0.59$  V, FF  $\approx 69\%$ , and  $\eta \approx 3.17\%$ . The difference observed in  $J_{SC}$  can be attributed to improvements in the crystallinity of the P3HT phase in the mixed solvent blends.

This is also confirmed by detailed atomic force microscopy and transmission electron microscopy analyses that give the indication of a phase separation between P3HT and PCBM driven by THN solvent addition [59]. Moreover, linear absorption spectra reveal that the relative intensity of the P3HT shoulder at 620 nm appears more pronounced in the blend deposited from oDCB + THN than from oDCB only. This is a further confirmation of the P3HT ordering. More information on the dynamic behavior of the photovoltaic devices, here characterized, can be extracted by electric noise spectroscopy.

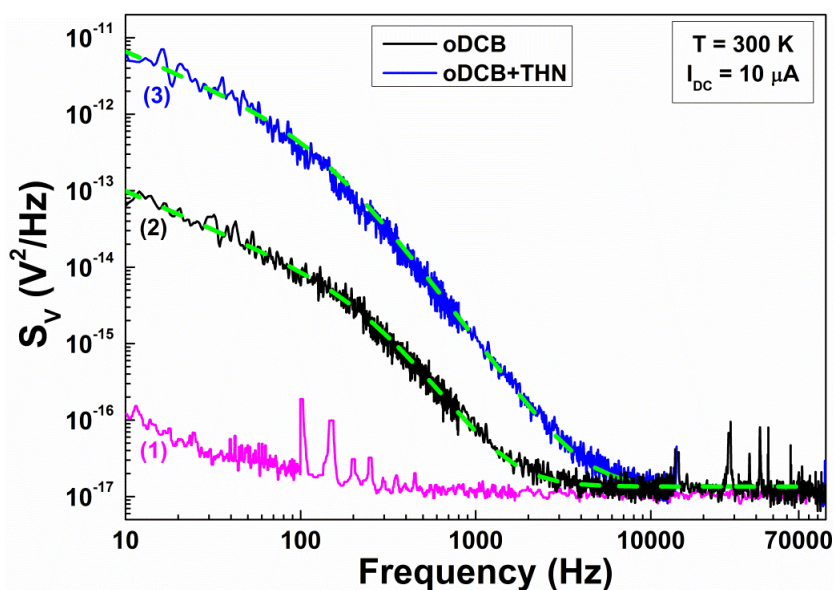


**Fig. 17.** Frequency dependence of the voltage spectral density, at a fixed temperature (300 K) and bias current (10  $\mu\text{A}$ ). Curve 1 is the system background noise spectrum, curve 2 refers to the device fabricated with oDCB as solvent, and curve 3 refers to the device fabricated with oDCB + THN as solvent mixture. The dashed curves are the best fit of spectra 2 and 3 by using equation (6).

In Fig. 16 the voltage spectral traces measured at 300 K and under dark conditions with a DC bias current of 10  $\mu\text{A}$  are shown. Curve 2 is

related to the blend fabricated with the reference solvent oDCB, while curve 3 is related to the blend fabricated with a mixture of oDCB + THN solvent. The theoretical model using eq. (6) (dashed curves in Fig. 17) describes the experimental data well. The corresponding values of the fitting parameters are  $K = (8.5 \pm 0.6) \times 10^{-11}$  and  $\gamma = (1.00 \pm 0.02)$  for the trace (2) and  $K = (1.4 \pm 0.1) \times 10^{-9}$  and  $\gamma = (1.00 \pm 0.02)$  for the trace (3). A shift of  $f_x$  to lower frequencies and an increase of  $K$  are observed when the THN solvent is added to the solution. At low values of current injection, the depletion capacitance,  $C_{\text{depl}}$ , related to the depletion layer at the interface between the blend and the cathode, is predominant. Conversely, at high DC bias currents the number of charge carriers accumulated in the active layer increases, thus producing the consequent enhancement of the chemical capacitance,  $C_{\mu}$ , compared to  $C_{\text{depl}}$ . By using the zero-temperature approximation of the Fermi function at occupancy  $>1\%$ , the chemical capacitance follows the shape of the electron DOS [69].

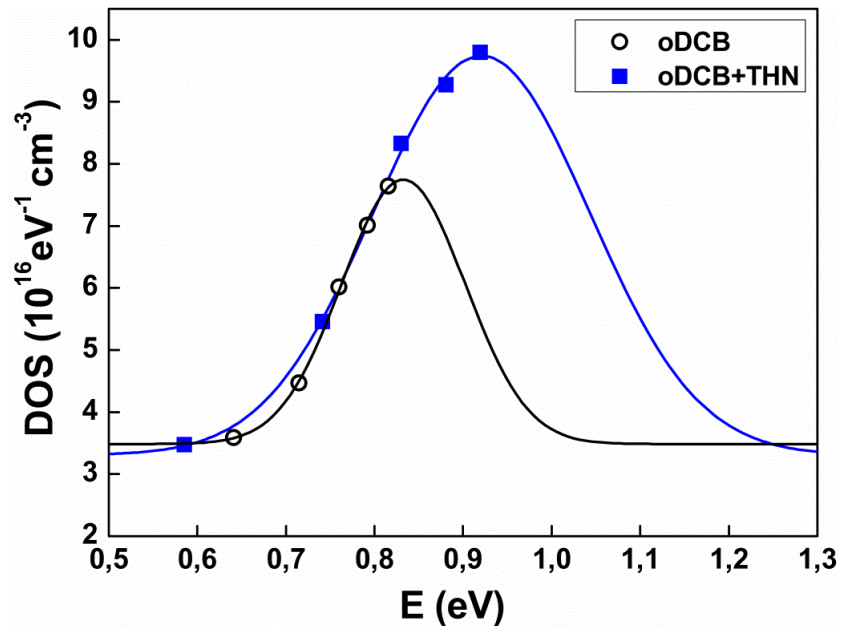


**Fig. 18.** Experimental DOS computed from noise measurements for solar cells fabricated with different solvent additives. The full squares refer to the oDCB + THN solvent mixture and the open circles refer to the oDCB solvent. The best fitting solid curves are obtained using (20).

By extracting the values of the cut-off frequency for different DC bias currents, the DOS  $g(E)$  and the electron lifetime  $\tau_n$  in the PCBM material can be computed [61, 85]. In Fig. 18 derived values of the DOS distribution for the two investigated samples, with and without solvent additive, are shown. In disordered organic semiconductors the DOS is usually modelled with a Gaussian distribution [70].

The value of  $g_0$  has been determined determined to be  $(3.3 \pm 0.1) \times 10^{-16} \text{ eV}^{-1} \text{ cm}^{-3}$  from the corresponding interface capacitance [21, 85]. The best fitting curves to the experimental data using (20) are shown in Fig. 18 as solid lines; the resulting best fitting parameters are listed in Table 2. The value of  $\tau_n$  is in good agreement with the value reported for most semiconducting polymers ( $\approx 100 \text{ meV}$ ) [105]. The values  $N$  and  $E_0$ , calculated for the device fabricated with the oDCB + THN mixture as solvent, are higher than the ones calculated for the device fabricated with the reference solvent.

**Table 2:** Best fitting values of the parameters in Equation (20). The DOS background level  $g_0$  is fixed to a value of  $3.3 \times 10^{-16} \text{ eV}^{-1} \text{ cm}^{-3}$  in the case of the solvent mixture and  $3.4 \times 10^{-16} \text{ eV}^{-1} \text{ cm}^{-3}$  in the case of the reference solvent.

| Solvent  | $N (\times 10^{17} \text{ cm}^{-3})$ | $E_0 (\text{eV})$ | $\sigma_n (\text{meV})$ |
|----------|--------------------------------------|-------------------|-------------------------|
| oDCB     | $0.8 \pm 0.1$                        | $0.82 \pm 0.03$   | $70 \pm 7$              |
| oDCB+THN | $2.1 \pm 0.2$                        | $0.92 \pm 0.04$   | $122 \pm 12$            |

This means that when using only oDCB as the solvent higher energy states are not accessible because the recombination kinetics severely limit the occupation of the DOS tail. This results in a lower  $\tau_n$  value [85]. The Gaussian DOS center  $E_0$  corresponds to the electron Fermi level in the PCBM material. In Fig. 19 the electron lifetimes as a function of  $V_F$ , extracted from the noise spectra as described earlier, for the two different types of polymer solar cells are shown. The values range between 0.8 and 0.2 ms, decreasing with increasing bias voltage (as also shown in inset of Fig. 7). Alternative methods for the determination of the charge carrier lifetimes in bulk heterojunction solar cells, such as impedance spectroscopy and photoinduced absorption, give similar results [92]. The lower values of the electron lifetime for the device fabricated with the reference solvent prove that strong recombination phenomena occur in the blend, thus limiting the charge carriers to occupy higher positions in the lowest unoccupied molecular orbital level and reducing the DOS population ( $N$ ).

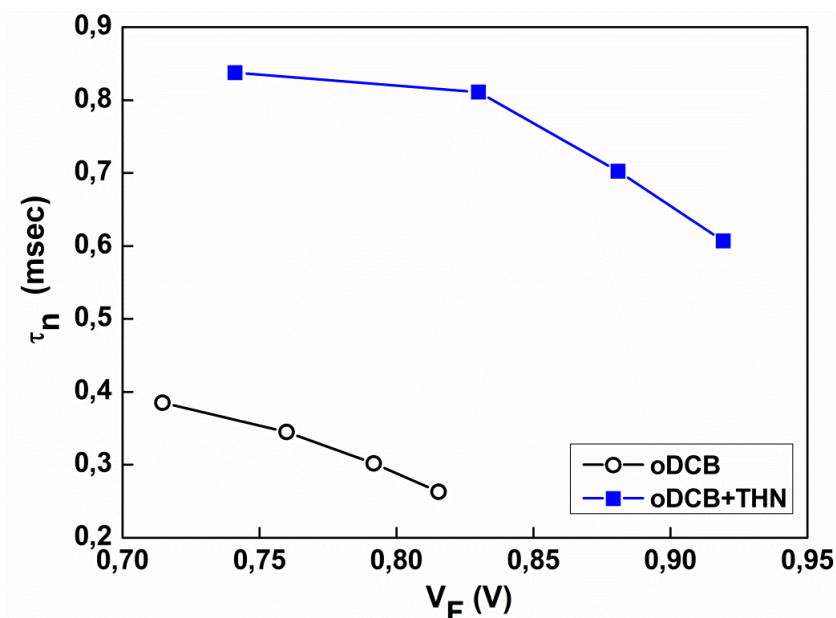


**Fig. 19.** Experimental electron lifetime dependence on the forward voltage  $V_F$  for solar cells fabricated with different solvent additives. Full squares refers to the oDCB+THN solvent and open circles refers to the oDCB solvent.

### 3.3. Summary

In conclusion, characterizations of P3HT:PCBM solar cells have been made by means of fluctuation spectroscopy at room temperature and in dark conditions. The experimental noise spectrum has been reproduced by modelling the photovoltaic device with a simple RC circuit, formed by the recombination resistance and the chemical capacitance of the active layer. Characteristic parameters, such as density of states and electron lifetime, have been extracted from noise measurements. The obtained results well compare with those reported in literature for similar organic heterostructures.

The current-voltage characteristics analysis is made in terms of the classical Schottky-Richardson emission law, in a temperature range between 300 and 340 K. It is found that the thermal stress induces an increase in the energy barrier height at the interface between the metal

contact and the blend. Simultaneously, a strong reduction of the series and recombination resistances of the charge carriers is found, when the temperature of 337 K is approached and after the cooling of the devices down to room temperature. These effects can be related to the well-known crystallization process of P3HT, due to a thermal treatment, and to the subsequent ordering of the P3HT chains occurring preferentially at the film-metal interface. The ordering of P3HT leads to a vertical phase separation between P3HT and PCBM, and to the formation of an undesirable structure with a P3HT rich region at the film-metal interface. This morphological modification is revealed by the noise level monitoring, which shows a peak at the temperature where P3HT crystallization is completed. Moreover, changes in the electrical conduction of the investigated devices are detected by computing the charge carrier mobility through the analysis of the flicker noise component. In particular, a decrease of the zero-field mobility is observed as a consequence of the thermal aging, thus inducing possible negative effects on the final device performance. The influence of the type of solvent used for the preparation of the P3HT:PCBM blend on important device parameters has been investigated using fluctuation spectroscopy at room temperature and in dark conditions. The increase of the P3HT ordering and the phase segregation between the polymer and fullerene in the active layer produce a strong reduction of the cut-off frequency,  $f_x$ , and an increase of the noise amplitude,  $K$ . An enhancement of the electron lifetime extracted from noise measurements for the blends prepared with the addition of THN to the reference oDCB solvent has been observed. This means that a more efficient charge carrier transport occurs in the active layer. The blends obtained using the oDCB solvent show a stronger charge carrier recombination at the donor-acceptor interface that limits the occupation of the upper energy states in the lowest unoccupied molecular orbital level. This is reflected in the DOS distribution, derived from noise measurements, which reveals a lower value of the disorder parameter than the device with the blend fabricated with an oDCB + THN mixture as the solvent.





## Chapter 4

# Zn-complex based on ambipolar oxadiazole / carbazole structure: Synthesis, optical and electrical properties

In the present chapter, we report on the preparation and characterization of a bi-functional mononuclear Zn(II) complex (named Zn(OC)<sub>2</sub>, (6) in the synthesis scheme of Section 4.1.7). In the organic ligands (OC=2-(5-(4-(4-(9H-carbazol-9-yl)butoxy)phenyl)-1,3,4-oxadiazol-2-yl) phenolate) both the carbazole hole transporter unit, and the oxadiazole electron transporter unit are covalently bonded. In the metal complex, the oxadiazole rings of the two ligands are bridged to the tetrahedral zinc(II) atom with the nitrogen atoms and two phenoxy groups. The Zn(OC)<sub>2</sub> complex exhibits blue luminescence in solution and in film and shows bipolar charge transport properties. In order to analyze the hole transport properties of the organic layer, a heterostructure between the Zn-organic compound complex and crystalline silicon (c-Si) has been prepared. Moreover, a comparison of the charge carrier mobility with the electric field planar and perpendicular to the Zn-organic thin film has been made.

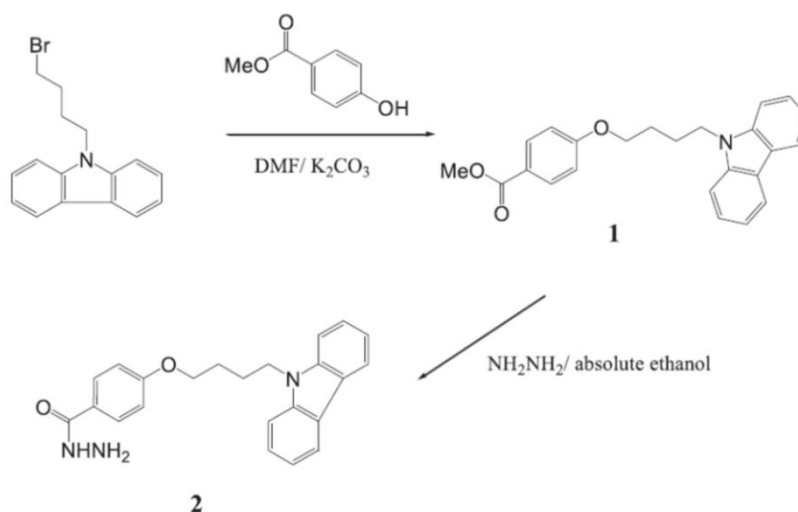
## 4.1. Experimental

### 4.1.1. Materials and synthesis

All reagents and solvents were purchased from Aldrich and Carlo Erba. N,N-dimethylacetamide (DMAc) and N,N-dimethylformamide (DMF) were refluxed on calciumhydride, distilled in vacuum and stored on 4 Å molecular sieves. Other reagents were used without further purification. N-(4-bromobutyl) carbazole was synthesized according to a previously reported procedure [34]. The OC ligand was obtained by the following synthetic steps:

### 4.1.2. Synthesis of 4-(4'-carbazol-9-yl-butoxy)-benzoic methylester (1)

Methyl 4-hydroxybenzoate (0.0300 mol) was dissolved in 250 mL of DMF; potassium carbonate was added and a solution of N-(4-bromobutyl) carbazole (0.0360 mol) in DMF (50 mL) was added drop wise to the first solution. The mixture was stirred at 150 °C for 16 h and then filtered into water (1200 mL). The aqueous solution was placed at 4 °C for 4 h and the solid crude product was filtered under vacuum and purified by crystallization from ethanol/water. The ester was collected with approximately 70% final yield. Proton nuclear magnetic resonance data ( $^1\text{H}$  NMR) are reported in the following.  $^1\text{H}$  NMR ( $\text{CDCl}_3$ ):  $\delta$  (ppm) = 8.13–8.01 (m, 2H); 7.99 (d, 2H); 7.50–7.45 (m, 2H); 7.36 (d, 2H); 7.27–7.22 (m, 2H); 6.88 (d, 2H); 4.43 (t, 2H); 4.02 (t, 2H); 3.92 (s, 3H); 2.12 (m, 2H); 1.91 (m, 2H).

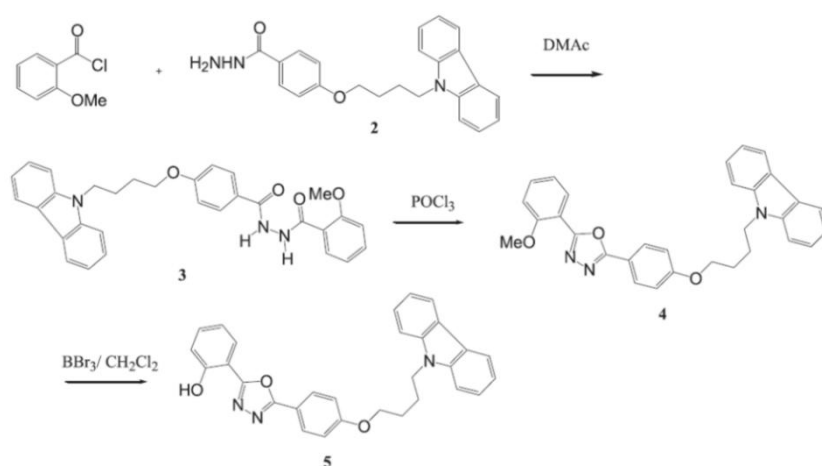


### 4.1.3. Synthesis of 4-(3-(9H-carbazol-9-yl)-butoxy)benzohydrazide (2)

Compound 1 (3.00 g) was dissolved in 100 mL of absolute ethanol and 100 mL of hydrazine monohydrate were added. The solution was stirred at reflux for 2 h, then cooled down in an ice bath. The precipitated solid was collected, repeatedly washed with boiling water,

and purified by crystallization from dioxane/water. The pure hydrazide was obtained with approximately 60% yield.  $^1\text{H}$  NMR (deuterated dimethyl sulfoxide,  $\text{DMSO-d}_6$ ):  $\delta$  (ppm) = 9.95 (s, 1H); 8.18 (d, 2H); 7.78 (d, 2H); 7.65 (d, 2H); 7.47 (t, 2H); 7.21 (t, 2H); 6.94 (d, 2H); 4.50 (t, 2H); 4.40 (m, 2H); 4.04 (t, 2H); 1.96 (m, 2H); 1.78 (m, 2H).

#### 4.1.4. Synthesis of 1-(4-(4'-carbazol-9-yl-butoxy)-benzoyl)-2-(2-methoxybenzoyl) hydrazine (3)



#### 4.1.5. Synthesis of 9-(3-(4-(5-(2-methoxyphenyl)1,3,4-oxadiazol-2-yl) phenoxy)butyl)-9H-carbazole (4)

The freshly synthesized 3 (0.55 g) was poured in 15 mL of phosphorous oxychloride ( $\text{POCl}_3$ ); the reaction was conducted at refluxing temperature for 5 h. The mixture was then slowly dropped into ice water (600 mL) and a precipitate was collected. The solid was washed and neutralized in 500 mL of aqueous  $\text{NaOH}$  0.1 M, and then purified by crystallization from DMF/water to obtain blue crystals, with m. p. = 158 °C, soluble in chloroform, ethanol, DMF and most organic solvents.  $^1\text{H}$  NMR ( $\text{DMSO-d}_6$ ):  $\delta$  (ppm) = 8.13 (d, 2H); 7.95 (d, 2H); 7.90 (d, 1H); 7.61 (m, 3H); 7.43 (t, 2H); 7.25 (d, 1H); 7.18 (t, 2H); 7.10 (m, 3H); 4.47 (t, 2H); 4.06 (t, 2H); 3.91 (s, 3H); 1.94 (m, 2H); 1.77 (m, 2H).

#### 4.1.6. Synthesis of 2-(5-(4-(3-(9H-carbazol-9-yl)butoxy)phenyl)-1,3,4-oxadiazol-2-yl)phenol (5): ligand OC

To a solution of 0.50 g (0.00102 mol) of compound 4 in 6.0 mL of  $\text{CH}_2\text{Cl}_2$  at  $-78\text{ }^\circ\text{C}$  was added drop-wise, over 10 min, 3 mL (0.0030 mol) of a  $\text{CH}_2\text{Cl}_2$  solution of  $\text{BBr}_3$ . The reaction mixture was allowed to warm slowly to room temperature. Water (7 mL) was added to the reaction mixture carefully, then the reaction mixture was extracted twice with 3 mL of  $\text{CH}_2\text{Cl}_2$ . The organic layer was dried over  $\text{Na}_2\text{SO}_4$ . The solvent was removed by evaporation to yield a blue solid. Purification of the residue from 20 mL of ethanol gave the product as a blue crystalline solid: 0.30 g (65%): m. p.  $192\text{ }^\circ\text{C}$ , soluble in DMSO,  $\text{CH}_2\text{Cl}_2$  and  $\text{CHCl}_3$ .

Anal. Calc. for  $\text{C}_{30}\text{H}_{25}\text{N}_3\text{O}_3$ : C,71.77; H,5.00; N,8.37. Found: C,71.77; H,4.55; N,8.37%.

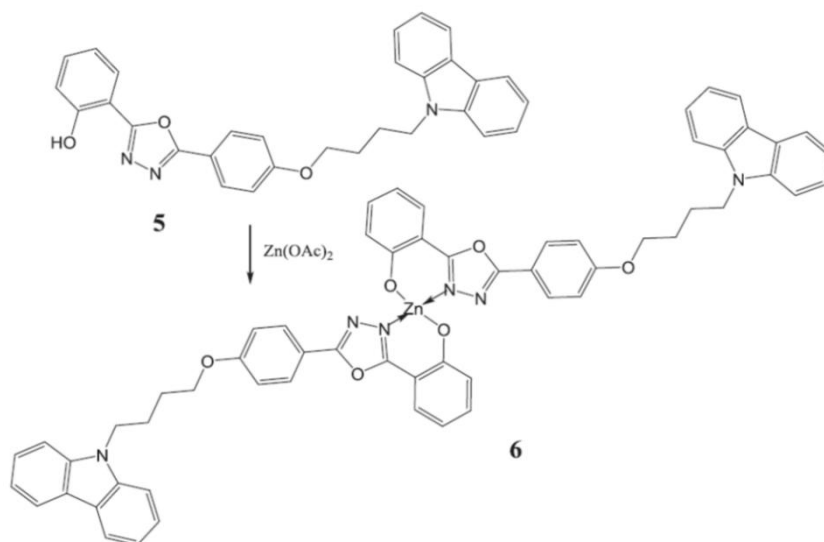
$^1\text{H}$  NMR ( $\text{DMSO-d}_6$ ):  $\delta$  (ppm) = 10.2 (s, 1H); 8.13 (d, 2H); 8.07 (d, 2H); 7.86 (d, 1H); 7.52–7.44 (m, 4H); 7.29–7.24 (m, 3H); 7.16 (d, 1H); 7.05 (t, 1H); 7.00 (d, 2H); 4.46 (t, 2H); 4.04 (t, 2H); 2.15 (m, 2H); 1.91 (m, 2H).

IR (KBr,  $\text{cm}^{-1}$ ): 3446 (w, v O-H); 3039 (w, v C-H); 2944 (w, v NC-H); 1616, 1509 (s, ar. v C = C); 1484 (s, al.  $\delta$  C-H); 1459 (s, v C-N); 1259 (s, v C-O); 748 (w, Ar.  $\delta$  C-H).

#### 4.1.7. Synthesis of complex $\text{Zn}(\text{OC})_2$ (6)

To a suspension of compound 2 (0.00134 mol, 0.5 g) in dry DMAc (7 mL) at room temperature, the 2-methoxybenzoylchloride (0.00134 mol, 0.199 mL) was added and the reaction was left to take place overnight under stirring. The reaction mixture was then poured into cold water (600 mL) and the resulting solid product was filtered, washed twice with water and dried under vacuum. m. p. =  $133\text{ }^\circ\text{C}$ . The product 3 was used in the subsequent intra-molecular ring closure reaction.  $^1\text{H}$  NMR ( $\text{DMSO-d}_6$ ):  $\delta$  (ppm) = 10.43 (s, 1H); 10.45 (s, 1H); 8.14 (d, 2H); 7.86 (d, 2H); 7.73 (d, 1H); 7.62 (2, 2H); 7.46 (m,

3H); 7.16 (m, 3H); 7.06 (t, 1H); 6.98 (d, 2H); 4.48 (t, 2H); 4.05 (t, 2H); 3.88 (s, 3H); 1.94 (m, 2H); 1.76 (m, 2H).



## 4.2. Characterization techniques

Thermal measurements were performed with a DSC-7 Perkin Elmer calorimeter under nitrogen flow at 10 °C/min rate. Thermogravimetric analysis (TGA) was performed with a TA Instruments SDT 2960 apparatus, in air at 20 °C/min. X-ray diffraction spectra were recorded using a flat camera with a sample-to-film distance of 90.0 mm (Ni-filtered Cu K $\alpha$  radiation). The FujifilmMS 2025 imaging plate and a Fuji Bio-imaging Analyzer System, mod. BAS-1800, were used for recording and digitizing the diffraction patterns. <sup>1</sup>H NMR spectra were recorded with a Bruker DRX/400 Spectrometer. Chemical shifts are reported relative to the residual solvent peak. UV-Vis measurements were performed with a Perkin-Elmer Lambda 800 Spectrophotometer and photoluminescence spectra in solution were recorded with a Jasco FP-750 Spectrofluorometer. Elemental analyses for the detection of Zn atom were carried out with an atomic absorption spectrophotometer (Model Analyst 100, Perkin Elmer) using solutions prepared by dissolving the samples in concentrated nitric acid. The C,

N and H atoms were analyzed by an Elemental Analyzer CHNS/O (Model Flash EA 1112, Thermo), equipped with a thermo-conductivity detector. IR spectra were recorded with a Thermo Nicolet 6700 FT-IR spectrometer. Measures were done using the Attenuated Total Reflection technique, using a performer plate ZnSe crystal, on powder samples or in transmission, using KBr Plates.

### 4.2.1. Film preparation and structure characterization

For the optical characterizations,  $\text{Zn(OC)}_2$  was dissolved in *o*-dichlorobenzene with a concentration of 5 mg/mL and stirred for 12 h at 70 °C. The film was deposited by drop-casting on top of sapphire substrates and dried for 5 min at 70 °C. In order to measure the photoluminescence, the sapphire samples were mounted on the cold finger of a nitrogen cooled cryostat and excited with a 377 nm diode laser from Coherent Inc. A Veeco Dektak 6 M stylus profiler was used to measure the thickness of the layers. A thickness of 800 nm was determined at the center of the films. For the preparation of the organic diode, indium tin oxide (ITO) coated glass substrates have been patterned, cleaned in acetone and isopropyl alcohol, and exposed to an oxygen plasma. A thin layer (55 nm) of poly(3,4-ethylenedioxythiophene) (PEDOT): poly(styrenesulfonate) (PSS) has then been spun on top of the ITO and dried at 180° C for 10 min. The active layer (800 nm) was spun on top of the PEDOT:PSS layer and annealed at 150° C for 10 min. The cathode was deposited by thermal evaporation of 20 nm of Ca and 130 nm of Al. The resulting device active area is  $A=0.1 \text{ cm}^2$ . The organic field effect transistor (OFET) has been fabricated on highly n-doped silicon substrates with a thermally grown layer of  $\text{SiO}_2$  with a thickness of  $230 \pm 10 \text{ nm}$ . The source-drain contacts are Au and have an interdigitated structure with channel lengths ( $L$ ) of 5  $\mu\text{m}$  and channel width ( $W$ ) of 1 cm. The fabrication of the transistor is reported in [106], and the respective sketch in the inset of Fig. 3. The source-drain current voltage characteristics ( $I_{\text{ds}}-V_{\text{ds}}$ ) have been recorded using a Keithley 236 and the gate voltage ( $V_{\text{g}}$ ) has been regulated with a Keithley 2400 source measurement unit.

## 4.2.2. Electronic device preparation and electrical characterization

In order to investigate the electrical properties of the organic material, organic/inorganic hetero-diodes have been prepared by drop-casting the  $\text{Zn}(\text{OC})_2$  on top of differently doped crystalline silicon (c-Si) substrates. In particular n-type, phosphorous doped  $\langle 110 \rangle$  oriented c-Si with a resistivity of 7–13  $\Omega \text{ cm}$  and p-type, boron doped  $\langle 100 \rangle$  oriented c-Si (7–13  $\Omega \text{ cm}$ ) were used as substrates. The natural oxide on the Silicon wafers has been removed with a 2 s dip in 48% HF and the substrates have then been rinsed for 2 min with distilled water and successively dried with nitrogen. After drop casting the organic material, the resulting heterostructure has been dried on a hot plate at 90 °C for 80 s. Finally, top and back electrode contacts were realized using silver paste. The top electrode has been in the case of the heterodiode applied on top of the  $\text{Zn}(\text{OC})_2$  film and in case of the reference structure directly on the c-Si wafer. The device area was about 0.1  $\text{cm}^2$ . Current density–voltage (J-V) measurements have been performed without illumination, using the Keithley Model “2400” source-measurement unit. The admittance spectroscopy characterization has been done using an HP 4109 impedance/gain-phase analyzer in the frequency range between 100 Hz to 1 MHz and under varying dc bias between -1 V to 1.5 V with an ac-signal amplitude of 50 mV.

## 4.3. Results and discussion

### 4.3.1. Structural and thermal characterization

In Fig. 1, the molecular structure of  $\text{Zn}(\text{CO})_2$  complex is shown. The complex was investigated by means of the VAMP software from Accelrys, with the PM6 functional. We performed a single-point energy calculation on the minimized geometry and we calculated highest occupied molecular orbital (HOMO) and lowest unoccupied molecular orbital (LUMO) of the complex (Fig. 1, HOMO shown in blue, LUMO in yellow). IR (KBr) and  $^1\text{H}$  NMR (DMSO- $d_6$ ) spectra of all compounds were in good agreement with the postulated structures.

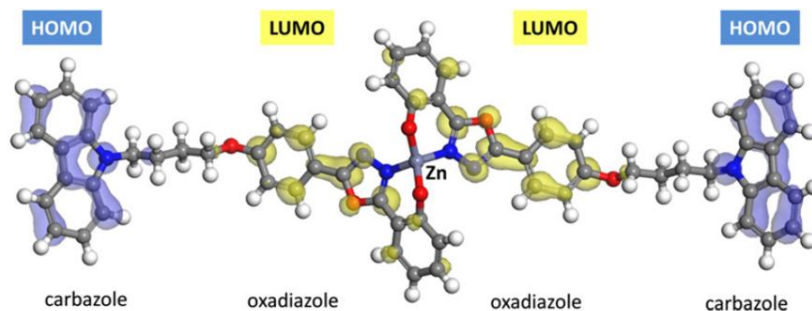


**Fig. 1.** Chemical structure of  $\text{Zn}(\text{OC})_2$  and visualization of HOMO and LUMO orbitals.

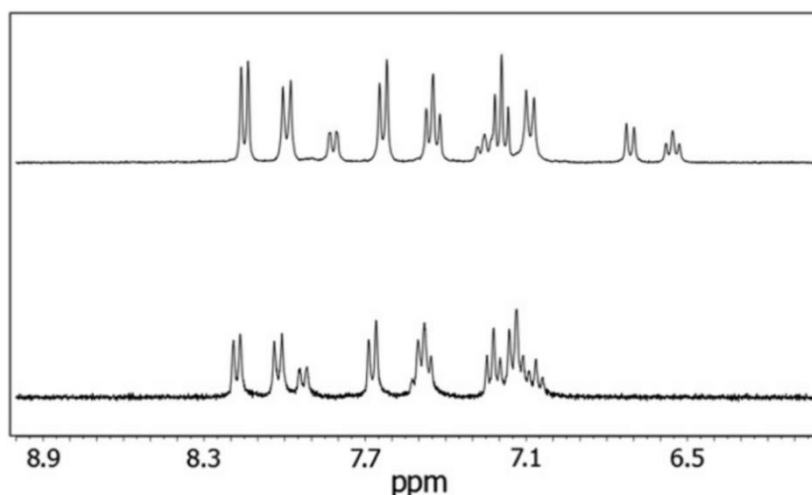


**Fig. 2.** <sup>1</sup>H NMR spectra of (a)  $\text{Zn}(\text{OC})_2$  complex and (b) OC ligand in  $\text{DMSO-d}_6$  (9–6 ppm region).

In particular, in Fig. 2, <sup>1</sup>H NMR patterns for complex and ligand are compared. In the spectrum of the  $\text{Zn}(\text{OC})_2$  complex, four signals relative to aromatic protons are shifted at higher delta (ppm) respect to the analog protons in the ligand OC. The elemental analysis of the Zn content of the complex (see Section 4.1.7.) is slightly lower than the nominal Zn content, (probably due to a small amount of complex degradation) but substantially consistent with it. Thermodynamic properties of ligand OC (**5**) and complex  $\text{Zn}(\text{OC})_2$  (**6**) are given in Table 1. Ligand OC (**5**) and complex  $\text{Zn}(\text{OC})_2$  (**6**), as obtained from the synthesis, are crystalline materials. We observed that OC ligand



exhibits solid-state polymorphism, as confirmed by X-ray analysis at room temperature and after crystallization from the melt (Fig. 3a and b), and from differential scanning calorimetry (DSC) analysis.

OC ligand crystallizes from ethanol solution in a crystal form ( $T_{m1} = 192.0\text{ }^{\circ}\text{C}$ ,  $\Delta H_{m1} = 70.6\text{ J g}^{-1}$ ), and it crystallizes from the melt in a different form ( $T_{m2} = 196.0\text{ }^{\circ}\text{C}$ ,  $\Delta H_{m2} = 67.5\text{ J g}^{-1}$ ). The complex  $\text{Zn(OC)}_2$ , during the first heating, shows a crystallization phenomenon not reported in Table 1, at  $201.17\text{ }^{\circ}\text{C}$  ( $\Delta H_c = 13.35\text{ J/g}$ ), followed by the melting peak at  $309\text{ }^{\circ}\text{C}$  ( $\Delta H_m = 88.4\text{ J g}^{-1}$ ).

**Table 1.** Calorimetric data of ligand OC and complex  $\text{Zn(OC)}_2$  from DSC and TGA analyses.

| Sample                              | $T_m$<br>( $^{\circ}\text{C}$ ) <sup>a</sup> | $\Delta H_m$<br>( $\text{J/g}$ ) | $T_c$<br>( $^{\circ}\text{C}$ ) <sup>b</sup> | $\Delta H_c$<br>( $\text{J/g}$ ) | $T_{m2}$<br>( $^{\circ}\text{C}$ ) <sup>c</sup> | $\Delta H_{m2}$<br>( $\text{J/g}$ ) | $T_d$<br>( $^{\circ}\text{C}$ ) <sup>d</sup> |
|-------------------------------------|--|----------------------------------|--|----------------------------------|---|-------------------------------------|--|
| <b>OC</b>                           | 192.0  | 70.60                            | 145.0  | 65.15                            | 196.4   | 67.54                               | 363.5  |
| <b><math>\text{Zn(OC)}_2</math></b> | 309.5  | 88.45                            | -  | -                                | -   | -                                   | 329.3  |

<sup>a</sup> First heating run.

<sup>b</sup> Cooling run.

<sup>c</sup> Second heating run.

<sup>d</sup> Initial decomposition temperature, at 5% weight loss.

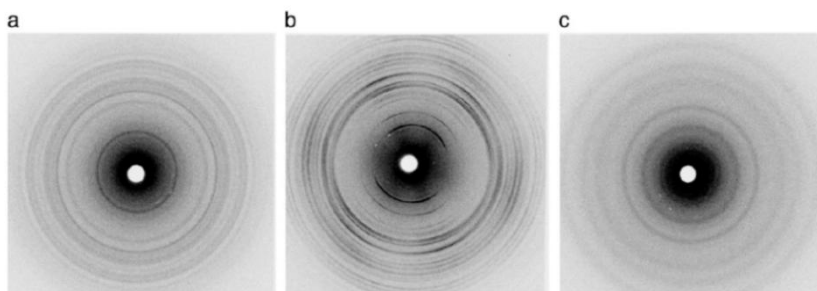


**Fig. 3.** X-ray diffraction patterns recorded at room temperature on powder sample of: (a) ligand OC crystallized from solution, (b) ligand OC crystallized from the melt, (c) complex  $\text{Zn(OC)}_2$  crystallized from solution.

After melt, in the cooling run, crystalline phase is not restored; this may be accounted for the complex molecular geometry of the investigated compound. The X-ray diffraction pattern of virgin samples of  $\text{Zn(OC)}_2$  and OC, recorded at room temperature (Fig. 3a and c), shows different reflection patterns at low angle diffraction region, confirming the different crystalline structures of the two

compounds. In the thermogravimetric trace of OC and  $\text{Zn(OC)}_2$ , the complete degradation process is observed around 400 °C (Table 1). OC shows a complete weight loss at 750–800 °C, while at the same temperature the Zn complex shows a residual metal content.

### 4.3.2. Optical characterization of solution and films

Fig. 4 shows the UV-Vis absorption spectrum of  $\text{Zn(OC)}_2$  in ortho-dichlorobenzene solution ( $10^{-5}$  M). The spectrum of  $\text{Zn(OC)}_2$  is the result of different absorption of carbazole and oxadiazole units, as already observed for similar compounds [34,50].

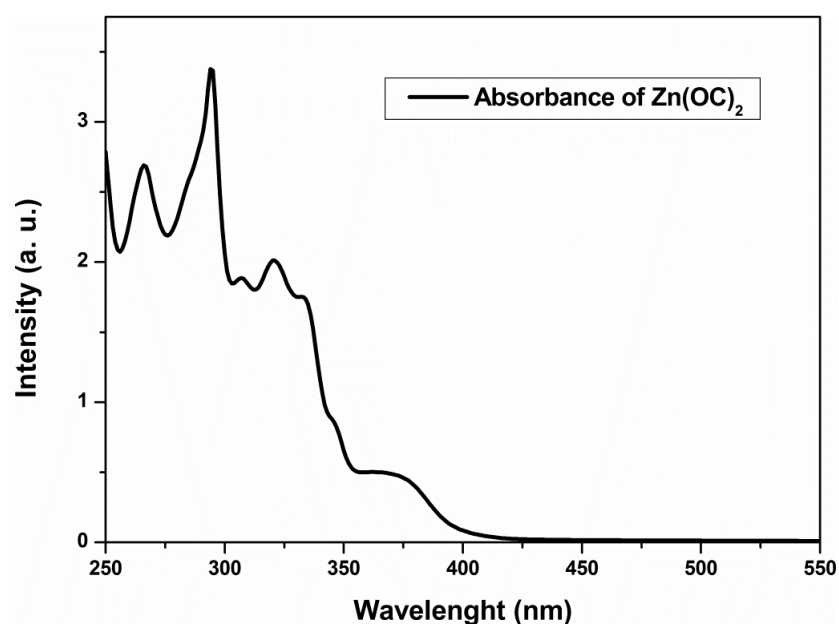
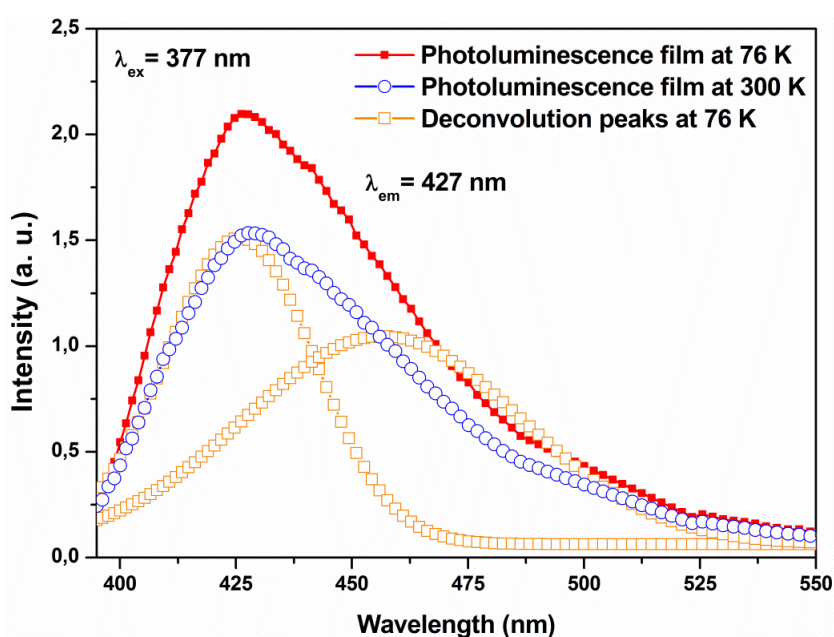


Fig. 4. UV-Vis absorption spectrum of  $\text{Zn(OC)}_2$  in ODCB solution.

The carbazole moiety absorbs at 295 nm, while the oxadiazole unit shows strong and broad peaks at 321 and 370 nm.  $\text{Zn(OC)}_2$  displays a well detectable fluorescence emission above 400 nm (maximum at 425 nm) in solid state. Fig. 5 shows the comparison of the photoluminescence of the thin film sample at two different temperatures. The full line and filled squares curve shows the

photoluminescence on film sample at 76 K, and the full line and open circle curve refers to the one at 300 K. All the spectra are characterized by a broad emission between 400 and 500 nm. The deconvolution procedure, performed on the experimental curve measured at 76 K, gives two peaks, centered at 424 nm and 460 nm. The peak intensity at 300 K is reduced by a fluorescence quenching effect, as already observed for other organic molecules [107].



**Fig. 5.** Photoluminescence spectra on Zn(OC)<sub>2</sub> in film at 76 K and 300 K, excited with a 377 nm diode laser.

### 4.3.3. Current density-voltage analysis of silicon-organic layer heterostructures

In order to investigate the ambipolar character of the material, we deposited the Zn(OC)<sub>2</sub> complex film on to two different crystalline silicon (c-Si) substrates, n-type and p-type respectively, forming in this way two organic/c-Si heterojunctions with the same emitter but different base material. For further comparison we deposited the silver-paste based top metal films on the two different types of c-Si substrates. In order to show that the heterojunction characteristic is not

compromised by the formation of electrical shunts between the top metal and the substrate (see Figs. 6 and 7) we report a comparison of the electrical characteristics of these reference structures, without the organic layer, with the organic/c-Si heterojunctions. Comparing the current density–voltage characteristics of the resulting devices, with and without  $\text{Zn}(\text{OC})_2$ -based layer, we observed a diode type behavior with a relatively high rectification ratio ( $>200$  at applied voltages of 1 V) for both heterojunction devices, independent of the c-Si doping type. In the case of the p-type c-Si/organic heterojunction, the forward characteristic is observed for a negative voltage applied to the top electrode (Fig. 6) and a rectification ratio of 270 between forward and reverse current density at an applied voltage value of 1 V has been measured. This means that, in this case, the organic film behaves in this case as n-type material. The respective reference structure, with direct deposition of the silver paste on the p-type c-Si substrate, is behaving as a Schottky-diode, though with a very low rectification ratio at 1 V of only 5.

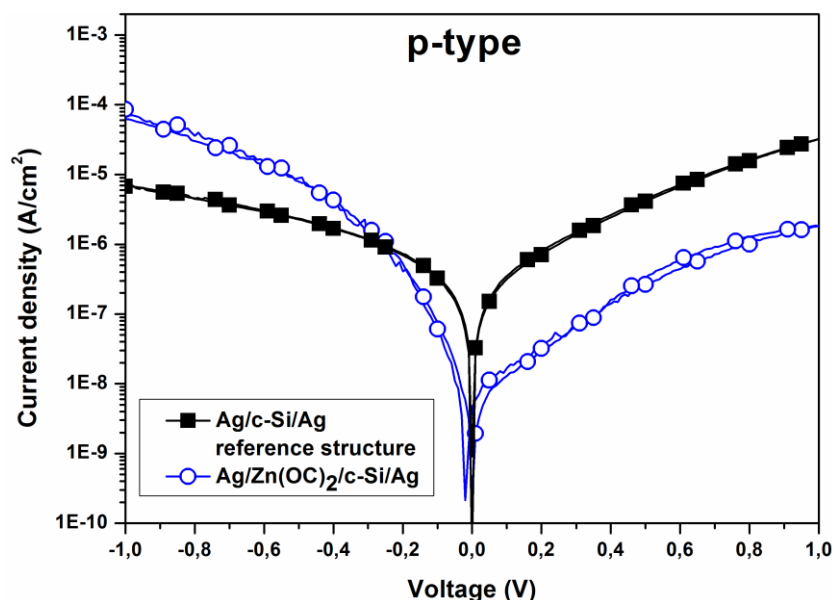


**Fig. 6.** Dark current density–voltage characteristics with (open circles) and without (filled squares) insertion of  $\text{Zn}(\text{OC})_2$  complex drop casted onto the p-type crystalline silicon substrate.

When depositing the organic layer on top of the n-type c-Si substrate, the resulting heterojunction has a current density at positive voltage higher than that measured when applying a negative voltage to the top metal contact (Fig. 7). In this case, the organic layer behaves as p-type material and a rather slightly lower rectification ratio of 85 at 1 V has been obtained. As in the case of a classical p-n diode, the characteristics almost saturates for reverse bias voltages around 1 V and in the forward bias regime an exponential increase of the diode current density with increasing applied voltage can be observed for voltages between 0.1 V and 0.6 V. In the case of the device with direct depositing of the top silver paste on top of the n-type c-Si substrate, the resulting current density–voltage characteristics shows almost perfect ohmic behavior without clear diode formation.

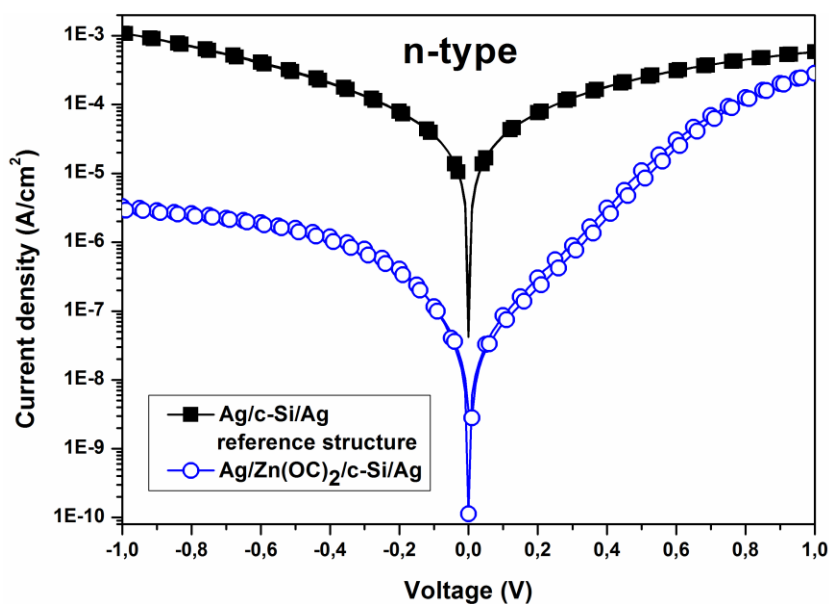


**Fig. 7.** Dark current density–voltage characteristics with (open circles) and without (filled squares) insertion of  $\text{Zn}(\text{OC})_2$  complex drop casted onto the n-type crystalline silicon substrate.

All the current density–voltage characteristics, shown in here, have been performed with two voltage slopes, starting always with an applied voltage of  $-1$  V to the top metal contact and increasing

subsequently the voltage first stepwise (10 mV steps) up to +1 V and decreasing it then with the same step width down to -1 V. For n-type c-Si/organic layer heterojunction we have observed a small hysteresis (in Fig. 7 the arrows indicates the voltage slope direction for forward biased diode), whereas for n-type c-Si/organic layer heterojunction we observed almost no hysteresis. This means that charge carrier trapping either in the organic material or at the hetero-interface does not dominate the electrical characteristics of these diodes.

#### 4.3.4. Electrical dc and ac characteristics

In Fig. 8 the current density-voltage (J-V) and the Mott-Schottky plot of the  $\text{Zn(OC)}_2/\text{c-Si}$  heterostructure are shown. From the Mott-Schottky analysis of the capacitance-voltage (C-V) measurements, as shown in Fig. 8a, a value of the dopant concentration of the silicon substrate ( $N_D$ ) of  $4.32 \times 10^{14} \text{ cm}^{-3}$  [96] has been deduced in the reverse bias voltage range between -0.2 and -0.9V. It is in good agreement with the nominal silicon wafer resistivity. The linear slope in the reverse bias region changes to a steeper slope in the forward bias regime due to the presence of the acceptor levels (with  $N_A$  concentration) in the forbidden band gap of the silicon, which results in a modification of the equivalent doping concentration to  $N_D - N_A = 2.06 \times 10^{14} \text{ cm}^{-3}$ . As reported by Goodman [108], the frequency dependence of the Mott-Schottky plot, shown in Fig. 8a, is due to the series resistance of the  $\text{Zn(OC)}_2/\text{c-Si}$  heterodiode. It is found that the extracted built-in voltage ( $V_{bi}$ ) increases with increasing measurement frequency. A similar frequency dependence, at low and for intermediate frequencies, is also reported by Stallinga [109] for a Metal-Insulator-Semiconductor structure based on organic layer used as insulating layer. In order to obtain a real value of the barrier height ( $\Phi_b$ ) at the  $\text{Zn(OC)}_2/\text{n-Si}$  interface, it is necessary to approximate the extracted voltage intercept ( $V^*$ ) in the relation:  $V^* = f(\omega^2)$ , where  $\omega = 2\pi f$  and  $f$  is the frequency. The zero frequency intercept gives an approximation value [110] of the barrier height of about 0.84 eV. As a consequence, the energetic position of the highest occupied molecular orbitals (HOMO) level for the organic layer can be estimated to have a value of 4.47 eV. Thus, the top metal contact works as an ohmic contact for the holes, while for the electrons there is an injection barrier of  $\Phi = 0.55 \text{ eV}$  at the c-Si/top metal interface, while at the

interface between the organic layer and the c-Si the electrons are blocked.

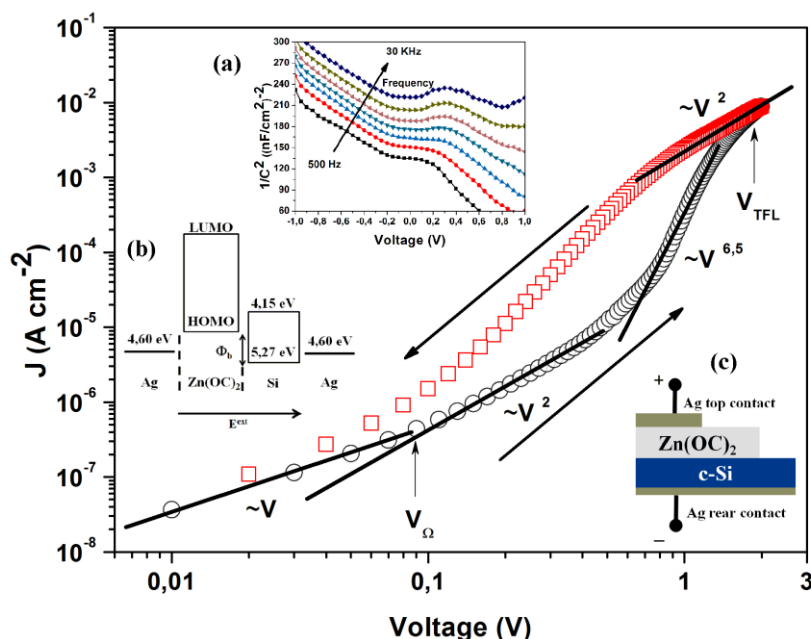


**Fig. 8.** Current density-voltage characteristics of the heterojunction between n-type c-Si and  $\text{Zn}(\text{OC})_2$  layer at room temperature. The Mott-Schottky plot, measured from 500 Hz up to 30 KHz, is shown in inset (a). The band-diagram of the heterodiode and the device cross section are shown in the insets (b) and (c) respectively. The energy levels are referred to the vacuum level.

At low frequencies and under reverse bias, the ac equivalent circuit of the heterostructure is simply composed by a series connection of the depletion capacitance ( $C_{\text{depl}}$ ) of the silicon substrate and the geometrical capacitance ( $C_g$ ) of the organic layer. The value of the capacitance due to the traps in the organic layer is negligible compared to  $C_g$ . The value of  $C_g$  can be estimated taking into account the value of  $C_{\text{depl}}$  at 500 Hz and zero applied bias voltage. Known the thickness of the organic layer, its relative dielectric constant ( $\epsilon_r$ ) has been estimated to a value of 4.66.

In Fig. 8 the voltage dependence of the current density suggests that the dominant conduction mechanism in the organic layer is the space charge limited current (SCLC) [111]. At low voltages, the curve follows an ohmic (linear) regime, due to the presence of the thermally

generated free carriers ( $n_0$ ), related to the shallow defect states, that at room temperature do not act as effective charge traps. With increasing applied voltage, at  $V = V_\Omega$ , the injected hole concentration exceeds that of the thermally generated free carrier concentration and the SCLC current becomes dominant. Thus, the current density can be expressed as  $J = 9/8\theta\mu_h\epsilon_0\epsilon_r V^2 d^{-3}$ , where  $\mu_h$  is the hole mobility and  $\epsilon_0$  is the dielectric constant of the vacuum.  $\theta = n/(n+N_t)$  is the trap parameter which takes the effect of the traps on the charge carrier mobility into account. It is the ratio between the free injected charge carriers ( $n$ ) and the trap density [111], because it can be assumed, that  $N_t \gg n$ . At high bias voltages, the current increases rapidly and reaches the trap-free regime value ( $\theta = 1$ ) at an applied bias  $V_{TFL} = qN_t d^2 \epsilon_0 \epsilon_r$ , where  $N_t = 2.13 \times 10^{16} \text{ cm}^{-3}$  is the density of traps and  $V_{TFL}$  has a value of about 1.8 V.  $\theta$  can be estimated by the ratio between the slopes of the J-V curve in the SCLC regime and in the SCLC trap-free regime.

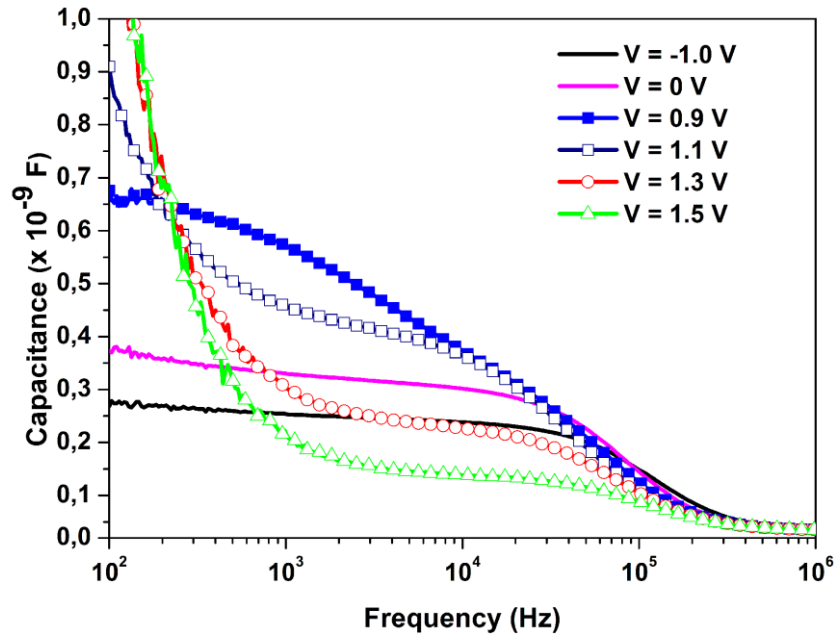


**Fig. 9.** Measured capacitance as a function of the frequency at different applied voltage. In reverse bias  $V = -1.0 \text{ V}$ ,  $0 \text{ V}$  (solid line) and in forward bias  $V = 0.9 \text{ V}$ ,  $1.1 \text{ V}$ ,  $1.3 \text{ V}$ ,  $1.5 \text{ V}$  (solid line with symbols).

The resulting value of  $\theta$  is  $2.47 \times 10^{-2}$ . Given the voltage  $V_\Omega = 0.1 \text{ V}$ , at



which the transition between the ohmic regime and the SCLC regime occurs, an estimation of  $n_0$  is possible by using the equation:  $n_0 = V_{\Omega} \theta \epsilon_r \epsilon_0 V / (dq)$ , where  $q$  is the electron charge. The density of the thermally generated free carriers has a value of  $4.25 \times 10^8 \text{ cm}^{-3}$ . The resulting value of the hole mobility is  $1.11 \times 10^{-5} \text{ cm}^2 \text{ V}^{-1} \text{ s}^{-1}$  in the free carrier regime. For  $V < V_{\text{TFL}}$ , the effective charge carrier mobility  $\mu_{\text{eff}} = \theta \times \mu_h = 2.74 \times 10^{-7} \text{ cm}^2 \text{ V}^{-1} \text{ s}^{-1}$ . The rather low value of  $\mu_h$  is due to the structural disorder of the organic layer [112]. The small molecules, that form the organic thin film, do not create an efficient path to transport the charge carriers. The long distance between two single transport units implies that the holes should have enough energy to hop between the delocalized states and then reach the interface.

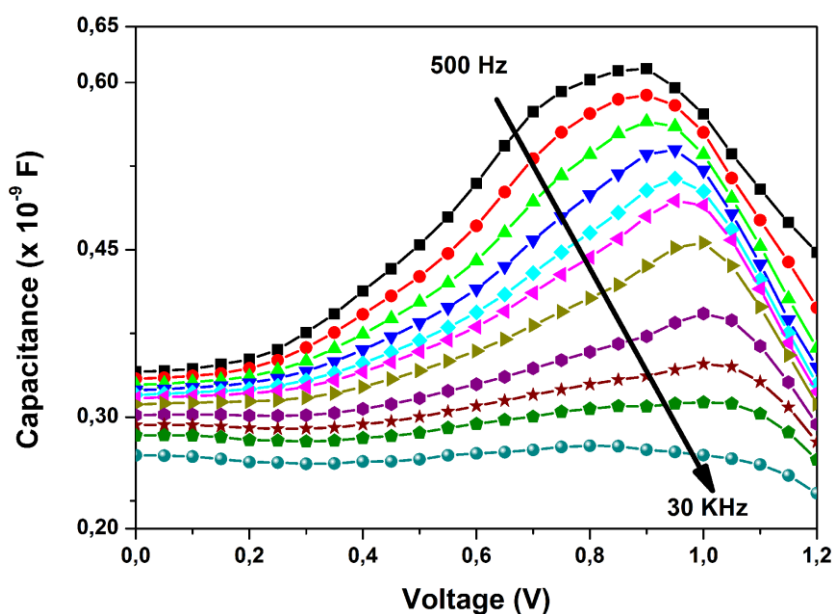


**Fig. 10.** Room temperature capacitance-voltage characteristics of the  $\text{Zn(OC)}_2/\text{n-Si}$  heterojunction diode at frequencies between 500 Hz and 30 kHz.

An investigation of the solvent concentration and type is under way. The hysteresis is due to a capacitive effect. The frequency dependence of the capacitance at different bias voltages is shown in Fig. 9. In reverse bias ( $V \leq 0 \text{ V}$ ), the charge amount due to the perturbation ac signal depends on the  $C_{\text{depl}}$  of the silicon. The contribution of the

capacitance of the organic layer is negligible. For larger values of the forward bias voltage ( $0 < V < 0.9$  V) the injected holes, from the top metal contact, in the organic layer follow the external electric field ( $E^{\text{ext}}$ ). The increase of the capacitance indicates a re-distribution of the injected carriers with a finite transit time [113]. In this voltage region, no charge recombination has been observed. At still higher voltage forward voltages ( $V > 0.9$  V) the holes are injected into the silicon layer and the recombination charge becomes dominant [114]. The recombination process consumes the injected carriers, resulting in a rapid decrease of the capacitance values. The dependence of the capacitance on voltage at various frequencies is shown in Fig. 10. A marked peak is evident at  $V = V_{\text{bi}} = 0.9$  V. In Fig. 10 the dependence of the C-V curves on the ac characteristic time  $\tau_{\text{ac}} = 1/f$  is also shown. At high frequencies the carriers are not able to follow the ac signal, resulting in a capacitance value independent of the applied voltage.

#### **4.3.5. Comparison of the charge carrier mobility in-plane and perpendicular to the organic layer**

The schematical molecular structure of  $\text{Zn}(\text{OC})_2$  is shown in Fig. 11 a. The Zn-atom connects the two arms in which the carbazole unit (C) transports the holes and the oxadiazole unit (O) transports the electrons. In the inset b of Fig. 12 the band diagram of the device with the  $\text{Zn}(\text{OC})_2$  active layer is shown. The energy values are referred to the vacuum energy level. Under forward bias, the holes are injected into the Zn-compound via the PEDOT:PSS layer, which functions as a hole transport layer (HTL), forming a good ohmic contact with the Indium Tin Oxide (ITO). The energy value for the HOMO level is estimated as 4.44 eV (as reported in section 4.3.4.). Since the active layer is a blue emitting molecule [115], the energy level of the LUMO is relatively low. In order to enhance the injection of the electrons into the LUMO level, the cathode is formed by the deposition of a thin layer of calcium, which is then immediately covered by a capping aluminum layer in order to avoid the degradation by oxidation [116].

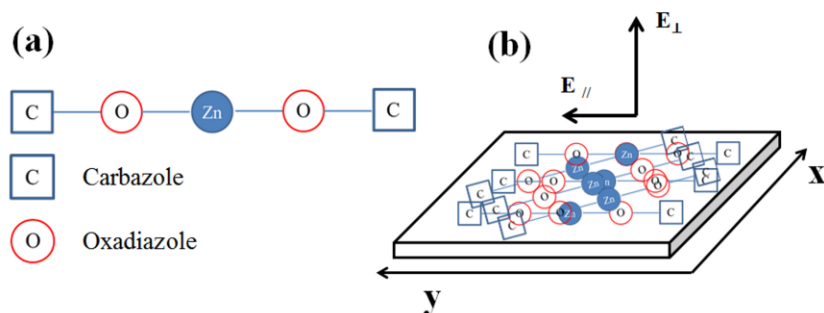


**Fig. 11.** a) Schematic molecular structure of the small molecule  $Zn(OC)_2$  (The carbazole transports the holes and the oxadiazole transports the electrons). b) Configuration of the parallel and the perpendicular electric field,  $E_{//}$  and  $E_{\perp}$  respectively, regarding to the x-y plane where the organic thin film has been deposited.

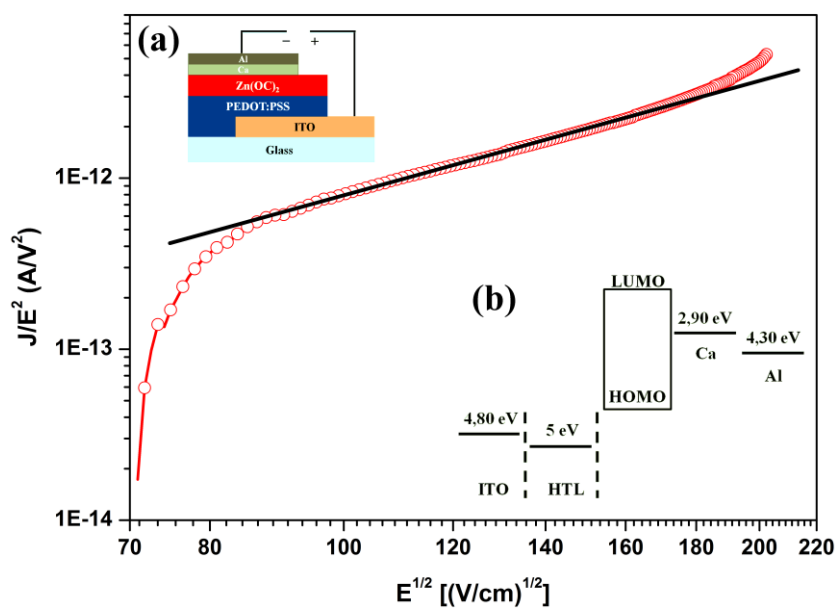


**Fig. 12.** Space-charge limited current characteristics (see straight line) for the diode with  $Zn(OC)_2$  as active layer. In inset (a) the cross section of the device and in inset (b) the band diagram structure of the diode are shown. The energy levels are referred to the vacuum level.

As a consequence, the electron injection barrier at the cathode is lowered. The electric field is applied orthogonal to the film surface and the voltage-dependence of the current density reveals a conduction mechanism based on the space-charge limited-current (SCLC) and follows the Mott-Gurney law:  $J = 9/8 \epsilon_0 \epsilon_r \mu_{\perp h} E^2/d$ , where  $E$  is the applied electric field,  $d$  the thickness of the active layer,  $\epsilon_0$  the permittivity of the free space,  $\epsilon_r = 4.66$  the dielectric constant of the small molecule (as reported in section 4.3.4.) and  $\mu_{\perp h}$  the hole mobility.

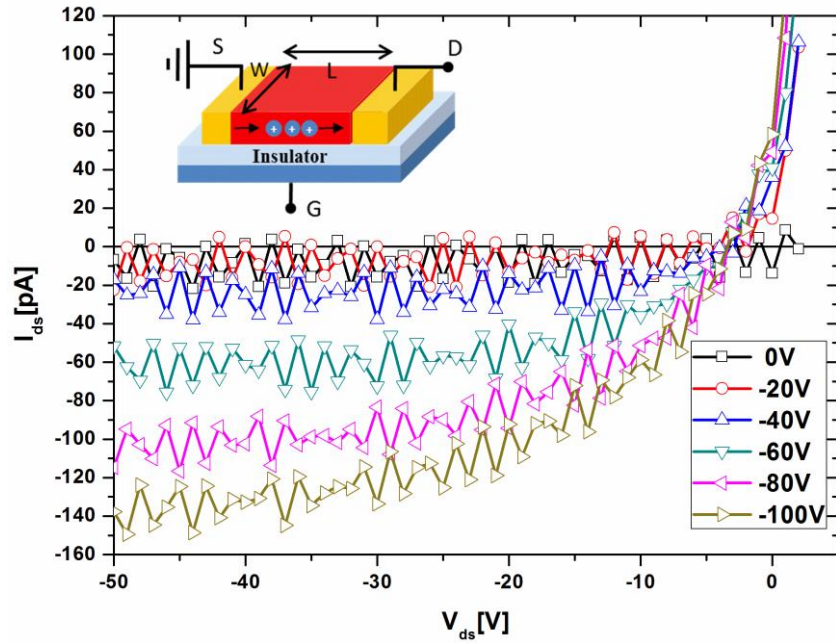


**Fig. 13.** Output characteristics for different gate voltages for the organic field effect transistor with  $Zn(OC)_2$  active layer. In the inset the schematic illustration of the device, where S, D and G are the source, the drain and the gate terminal respectively, is shown.

$\mu_{\perp h}$  is influenced by the electric field and obeys to the follow equation [117]:

$$\mu_{\perp h}(E) = \mu_0 e^{\gamma\sqrt{E}} \quad (26)$$

where  $\mu_0$  is the mobility at zero-field. This means that the barrier at the cathode prevents the electron injection and the diode becomes a

single carrier hole-only device. By fitting the linear part of the curve in Fig. 12 value of  $\mu_{\perp 0} = 2.78 \times 10^{-9} \text{ cm}^2 \text{ V}^{-1} \text{ s}^{-1}$  and  $\gamma = 2.35 \text{ cm}^{-0.5} \text{ V}^{0.5}$  have been obtained. In Fig. 13 the output characteristics of the OFET with the  $\text{Zn(OC)}_2$  as active layer for different  $V_g$  values is shown. From the saturation  $I_{\text{ds}}-V_{\text{ds}}$  characteristics, the hole mobility  $\mu_{\text{h}} = 2L [\partial(I_{\text{ds}})^{0.5}/[\partial(V_g)]^2]/(WC_i)$  and the threshold voltage  $V_{\text{th}}$  have been extracted (where  $C_i$  is the capacitance of the  $\text{SiO}_2$  layer). The obtained characteristic parameters are  $\mu_{\text{h}} = 1.09 \times 10^{-9} \text{ cm}^2 \text{ V}^{-1} \text{ s}^{-1}$  and  $V_{\text{th}} = 57 \text{ V}$ . The low hole mobility and the high  $V_{\text{th}}$  suggest a low crystallinity of the thin organic film [118]. The asymmetric behavior in the output characteristics is due to the existence of the gate leakage current in the forward  $V_{\text{ds}}$ .

#### 4.4. Summary

In summary, in this work we have reported the synthesis and the study of a Zn(II) complex,  $\text{Zn(OC)}_2$ , as the organic component for heterodiode structures. The synthesized complex is a blue emitting molecule, quite soluble in chlorinate organic solvents and processable into homogenous thin films. We have studied the electrical behavior of  $\text{Zn(OC)}_2$  as electron- or hole-conductor by the characterization of heterojunctions, where the organic layer has either been deposited by drop-casting on top of p-type or n-type crystalline silicon substrates. For Zn-organic compound and c-Si n type heterostructure an electrical characterization has been made by current-voltage and capacitance measurements. The barrier heights at the interfaces and the value of the dielectric constant for the organic layer ( $\epsilon_r = 4.66$ ) have been determined. The determined low value of the HOMO level energy (4.44 eV) allows to form a relatively good ohmic contact with the Ag front contact. The dominating electrical conduction mechanism for holes is the trap-controlled space charge limited current. The high value of the density of the traps of  $2.13 \times 10^{16} \text{ cm}^{-3}$  results in a low value of the hole mobility of  $2.74 \times 10^{-7} \text{ cm}^2 \text{ V}^{-1} \text{ s}^{-1}$  which increases up to a value of  $1.11 \times 10^{-5}$  when all traps are filled.



## Chapter 5

# Investigation of the characteristics of a combination of InP/ZnS-quantum dots with MWCNTs in a PMMA matrix

In this chapter we want to address if - from the optical point of view - another QD/CNT combination, based on the use of commercially available InP/ZnS quantum dots and MWCNTs without prior complex functionalization can be used for the improvement of polymer based solar cells. For this reason the two types of nanostructures were introduced into a non-conductive polymer matrix and the effects on the optical properties of the films were examined changing the concentration of MWCNTs and maintaining constant the QDs concentration. A detailed analysis of the results has been done, based on the method introduced by Wang et al., who treated a similar problem in the case of epoxy/CNT composite films [18].

### 5.1. Experimental details

#### 5.1.1. Materials

Dimethylformamide (DMF) is a solvent, commonly used for spin-coating of polymethyl-methacrylate (PMMA) with incorporated MWCNTs. It was produced by the Carlo Erba company. PMMA is an electrically insulating polymer and transparent in the whole visible spectral range [119]. The PMMA used was purchased in solid form as a white powder from Aldrich. The MWCNTs were commercially available non-functionalized type “3100” CNTs from NANOCYL, with a typical length of 0.1-10  $\mu\text{m}$  and a typical diameter of 10 nm. The quantum dots (QDs) were composed by an indium phosphide core with a zinc sulfate shell (InP/ZnS) and were purchased from NN-labs.

These nanocrystals (NCs) possess a luminescent quantum yield exceeding 60% [120]. The emission peak is located at around 650 nm and the absorption peak at 640 nm  $\pm$ 10 nm. The solution of PMMA with carbon nanotubes has been prepared using 5 mg of non-functionalized MWCNTs that were solved in 2 ml of DMF. The solution has been sonicated for 30 min at room temperature. For the 1% solution, few CNTs clusters were visible and for the 4% and 7% solutions more clusters were visible in the otherwise homogeneously black solution. Successively, the MWCNTs solution has been mixed with the PMMA solution in order to obtain the three different concentrations of MWCNTs. The three different solutions have then been sonicated for 60 min at a temperature of 40°C [121]. Another solution was processed in the same way without sonication directly after the CNTs addition. These have been used for the preparation of the solution containing CNTs as well as quantum dots. InP/ZnS quantum dots with a concentration of 5wt% have been added to these solutions with the three different MWCNTs. Also in this case subsequently the combined solutions with CNTs and QDs have been sonicated for 60 min at 40°C [122,123].

### 5.1.2. Characterization

The thickness of the spin-deposited PMMA films with the nanoparticles has been determined using a KLA Tencor profilometer and ranged typically from 200–300 nm. Photoluminescence measurements of the deposited films have been performed using a 10mW violet laser diode (405 nm) for excitation and a Lot Oriel “M-74000” monochromator, an UDT type “PIN10” large area silicon photodiode and a Stanford Research “SR830” Digital Lock-in Amplifier for detection. Photoluminescence measurements of the solutions has been done with a HORIBA “FluoroLog – Modular” Spectrofluorometer, using as well a 405 nm laser diode light for excitation. UV-VIS transmission measurements have been performed using a Perkin-Elmer “Lambda 800” Spectrophotometer. The SEM images have been taken using a GEMINI Scanning Electron Microscope.



### 5.1.3. Substrate preparation

Before the spin-coating deposition, the glass substrates were cut into of 25 mm x 25 mm squares, sonicated in acetone for 30 min at 40°C and subsequently dried with nitrogen. Subsequently the solutions have been deposited onto the substrates using a Laurell Technologies model “WS-650SZ-6NPP/LITE/IND” spin coater applying a single step with of 2000 rpm for 30 s and an acceleration of 1500 rpm/s. The samples have been before and after spin-coating annealed for 2 min at 170°C on a hot plate. Similar conditions have been proposed in literature for PMMA film deposition [124].

## 5.2. Results and discussion

### 5.2.1. Photoluminescence studies

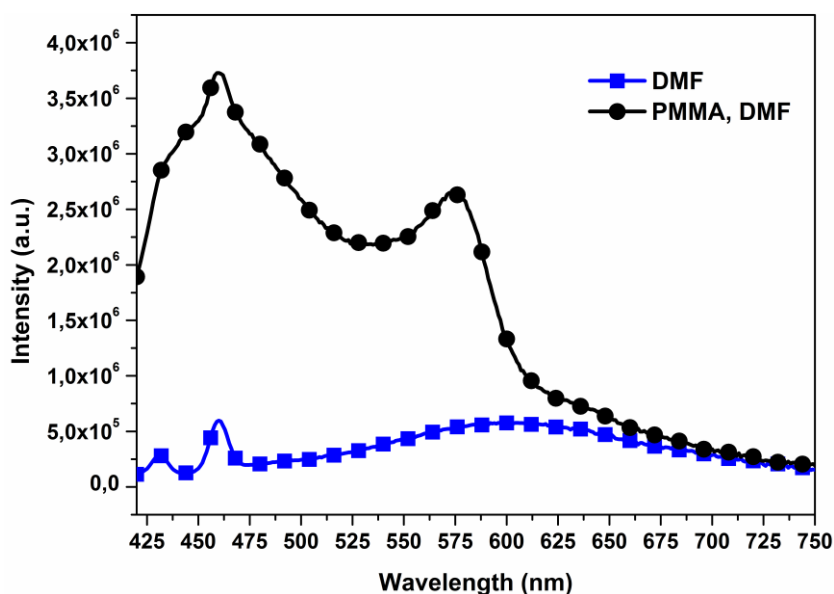


**Fig. 1.** Photoluminescence spectrum of the DMF solvent, with and without addition of PMMA.

The photoluminescence (PL) spectra of solutions and films of the composite with varied concentration of MWCNTs have been

compared in order to verify the incorporation of the QDs into the polymer matrix.

In Fig. 1, where the PL spectra of the DMF only and of the PMMA in DMF are shown, we observe three peaks related to the DMF solvent at 432 nm, 460 nm and a broader peak at 600 nm. Adding the PMMA we observe an additional peak around 575 nm and the two DMF peaks at 432 nm and 600 nm are only visible as small shoulders in the PL spectrum. In Fig. 2 for comparison the PL spectra of all the solutions, used in the fabrication of the films with 1% carbon nanotubes, are shown. It is clearly observable that the 670 nm peak is present only in the QD containing solution.

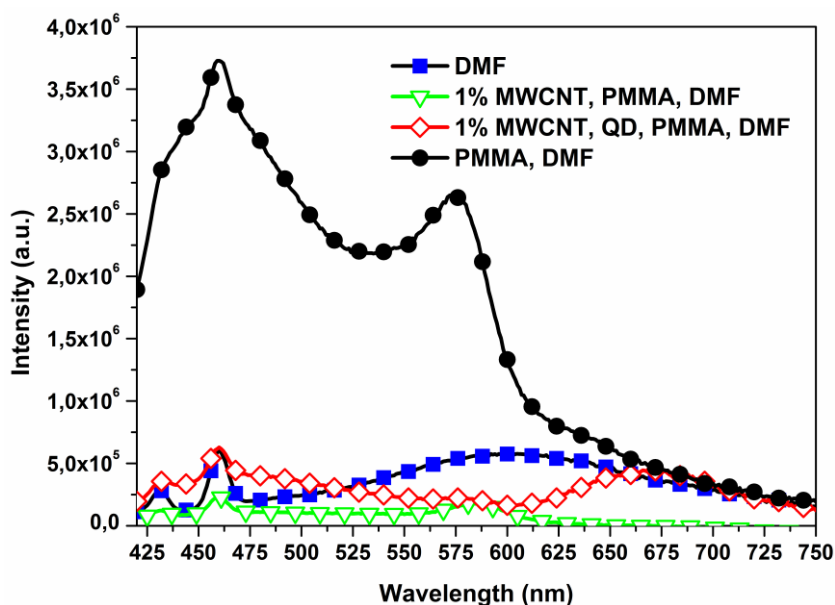


**Fig. 2.** Comparison of the photoluminescence spectra of all solutions used in the fabrication of the samples with 1% CNT content.

In Fig. 3 the photoluminescence peak, measured on the deposited films containing QDs and 1% MWCNTs, is shown. Basically a broad red emission peak at 664 nm with a full width half the maximum (FWHM) value of 67 nm, related to the QD emission is observed [125]. In Fig. 4 we plotted the PL peaks for the solutions, containing additionally as well the InP/ZnS quantum dots as different concentrations of carbon nanotubes. One can observe, that with increasing CNTs content the PMMA peak at 575 nm is decreasing,

while for all three CNT concentrations a relatively broad PL peak centered at 670 nm is visible.

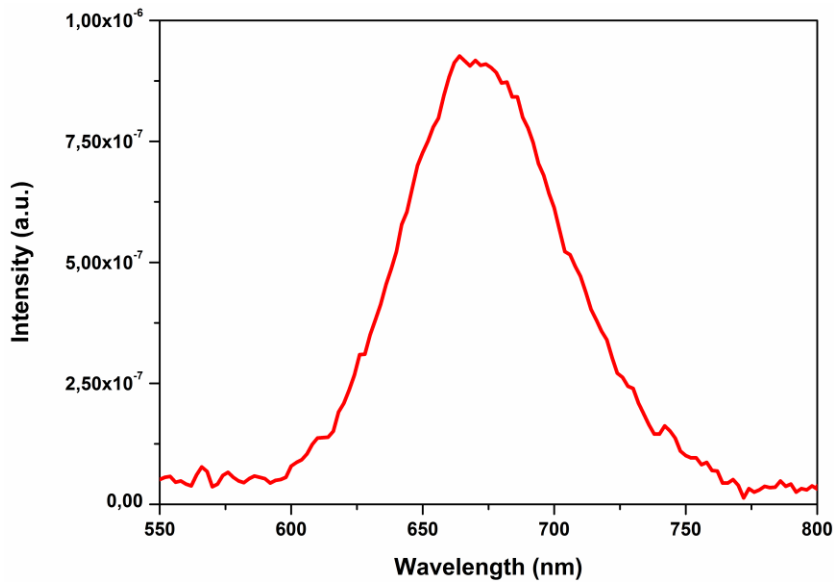


**Fig. 3.** Photoluminescence spectra of the nanocomposite film, deposited on a glass substrate with 1% CNTs and 5% QDs in the solution used for spin-coating.

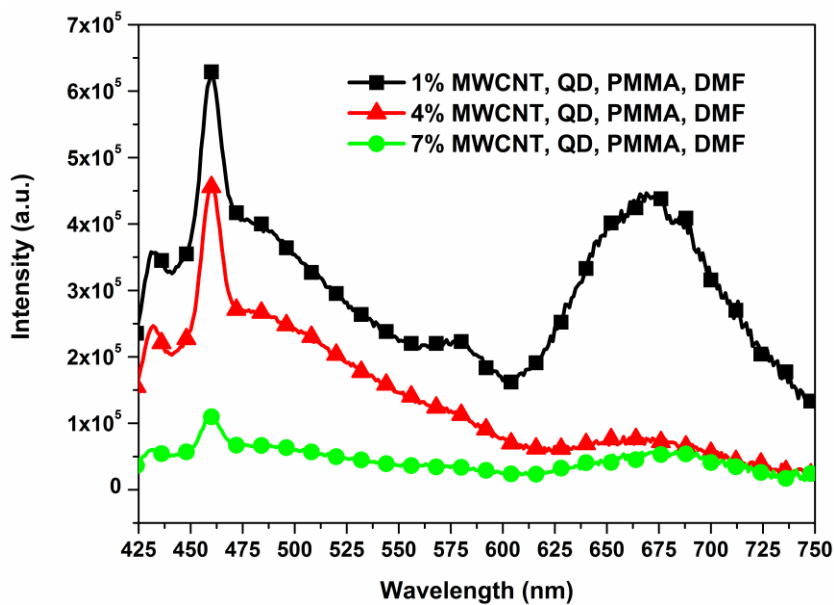


**Fig. 4.** Photoluminescence spectrum of the solutions containing 5% of QDs and different CNT concentrations.

This peak can be clearly identified as the emission peak of the InP/ZnS quantum dots [126]. This confirms the successful incorporation of the quantum dots into the deposited films.

This emission peak could, however, only be observed on the sample with a low content of carbon nanotubes. A possible explanation for this suppression of the QD photoluminescence with increasing CNTs content either a PL quenching due to efficient charge carrier separation or an optically shielding of the quantum dots by the CNTs. It is for example well known, that the photoluminescence of P3HT is quenched by the addition of PCBM [127].

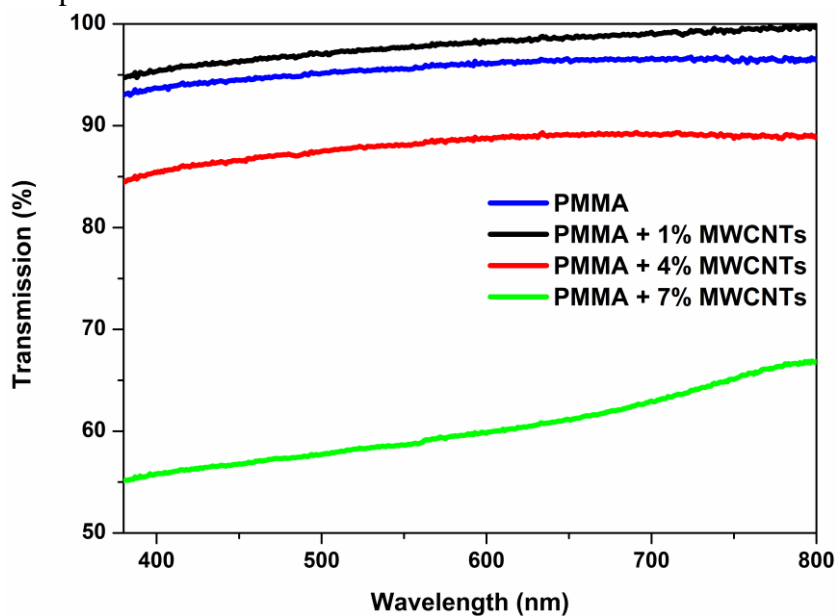
### 5.2.2. Optical transmittance measurements

Measuring the optical transmittance as a function of wavelength (as shown in Fig. 5a) in the case of the samples with 1% MWCNTs concentration an enhancement of the transmittance is observed as compared to the pure glass substrate. This can be explained by the composite film acting as an antireflective coating for the glass substrate. Increasing the carbon nanotube concentration further to a value of 4%, we observe an about 8% decrease of the optical transmittance in the whole investigated spectral range from 400 nm up to 800 nm. Increasing the CNT concentration further to 7%, the transmission loss, as compared to the uncoated substrate, is higher than 25%. By adding the QDs to the film, the behavior changes (as shown in Fig. 5b). We observe a decrease of the transmission only for the sample with the highest CNT concentration of 7%. This decrease is clearly less pronounced as compared to the case of the sample with the same CNT concentration but without quantum dots. This fact is a strong indication that the QDs incorporation is altering the CNT distribution. In order to exclude the influence of the PMMA polymer matrix on light transmittance, a normalized light transmittance,  $T_n(\lambda)$ , of thin film is calculated by:

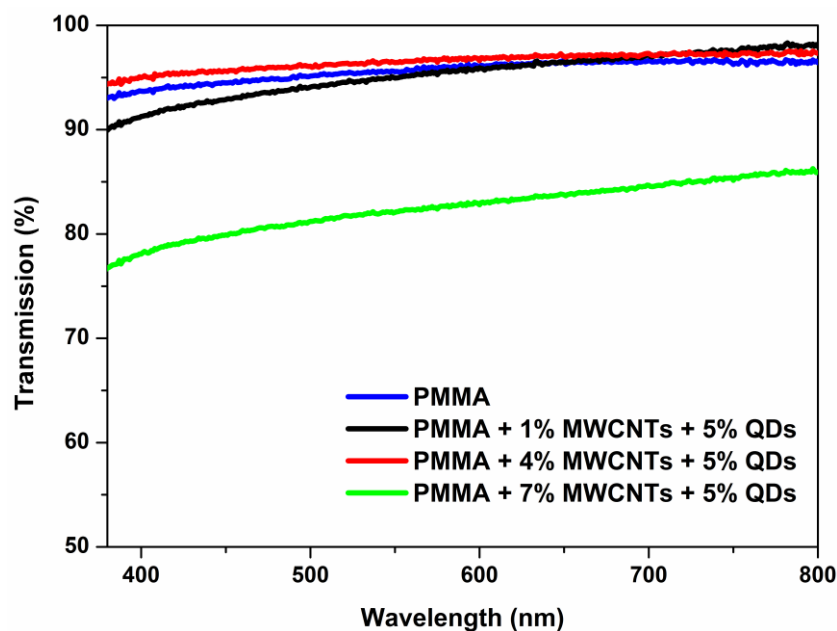
$$T_n(\lambda) = T_c(\lambda) / T_m(\lambda) \quad (27)$$

where  $T_c(\lambda)$  is the light transmittance of either the MWCNTs/polymer films or the films with the addition of 5% QDs, and  $T_m(\lambda)$  is the light

transmittance of the pure PMMA polymer film without incorporation of nanoparticles.



(a)



(b)

**Fig. 5.** Optical transmission spectra of PMMA and MWCNTs films on glass for different CNT concentrations (a) without and (b) with containing 5% of QDs.

Fig. 6 shows the plot of the normalized transmittance at 550 nm wavelength ( $T_n(550)$ ) versus the weight fraction ( $f_w$ ) of the MWCNTs. It can be observed that  $T_n(550)$  decreased with the increase of the MWCNTs content. Adding the QDs, the effect of CNTs on the optical transmittance is less marked and thin films are more transparent. In order to make the role of the CNTs more evident, the normalized transmittance for both the thin films have been interpolated with the following polynomial function  $y = 1 + a_1(\lambda)f_w + a_2(\lambda)f_w^2$  at different wavelengths. As shown in Figs. 7 and 8 the coefficients  $a_1(\lambda)$  and  $a_2(\lambda)$  follow a second order polynomial relationship.

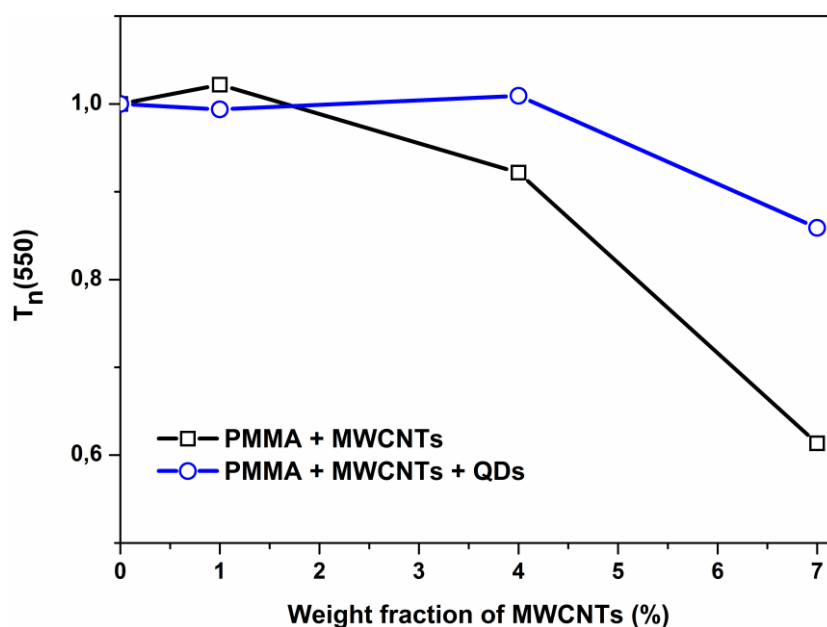


**Fig. 6.** Plot of the optical transmission at 550 nm as a function of the CNT concentration in the solution, normalized to the transmission of the PMMA film without nanoparticles.

The empirical equations, used for the PMMA/MWCNTs (Eqs. (28), and (29)) and for the PMMA/MWCNTs/QDs (Eqs. (30), and (31)) thin films are as follows:

$$a_1(\lambda) = -3.9331 + 0.025343 \lambda - 2.3484 \times 10^{-5} \lambda^2 \quad (28)$$

$$a_2(\lambda) = 30.927 + 0.37474 \lambda - 3.86 \times 10^{-4} \lambda^2 \quad (29)$$

$$a_1(\lambda) = 8.5129 - 0.015798 \lambda + 1.0625 \times 10^{-5} \lambda^2 \quad (30)$$

$$a_2(\lambda) = 174.25 - 0.30083 \lambda - 1.9861 \times 10^{-4} \lambda^2 \quad (31)$$

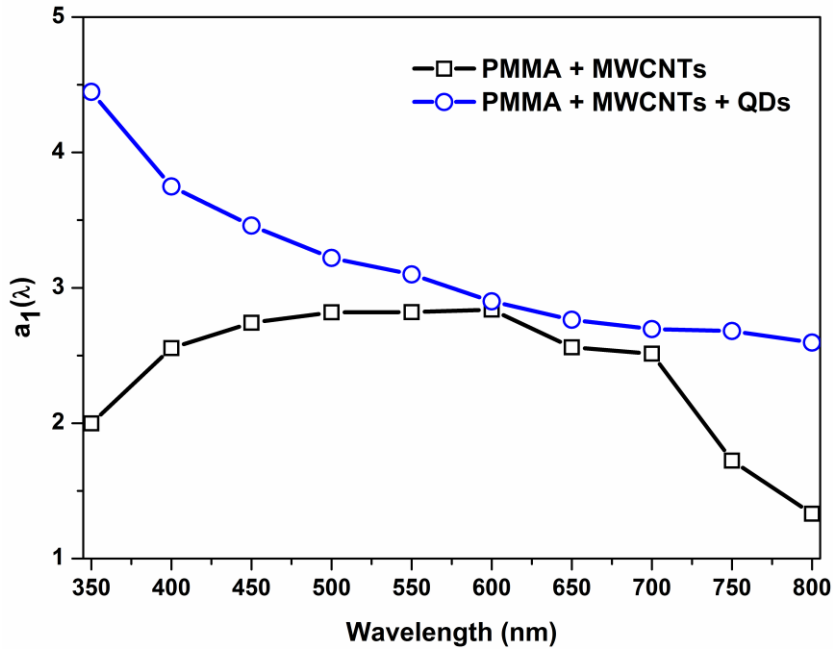


**Fig. 7.** Wavelength dependence of the  $a_1(\lambda)$  coefficient for the normalized transmittance for the PMMA/CNT thin films with and without QDs.

According to this empirical equations the predicted results of the normalized light transmittance of the thin film for the wavelength range between 380 nm and 800 nm are shown in Figs. 9 and 10. A good agreement between experimental data and empirical equations is found. Adding the QDs to the PMMA/MWCNT film, the experimental data are equally well fitted except for the film with the 1% CNT concentration. In order to clarify the influence of the QDs on the film transmittance, we plotted in Fig. 11 the optical transmittance of the films with QDs and various CNT concentrations normalized to the optical transmittance of the respective film without QDs. It can be clearly seen, that the decrease of the optical transmission with increasing CNT concentration is strongly reduced by the addition of the QDs. A possible explanation is that the QD addition induces a CNT agglomeration in small areas of the film and hence the effective CNT concentration in the remaining areas is strongly reduced.

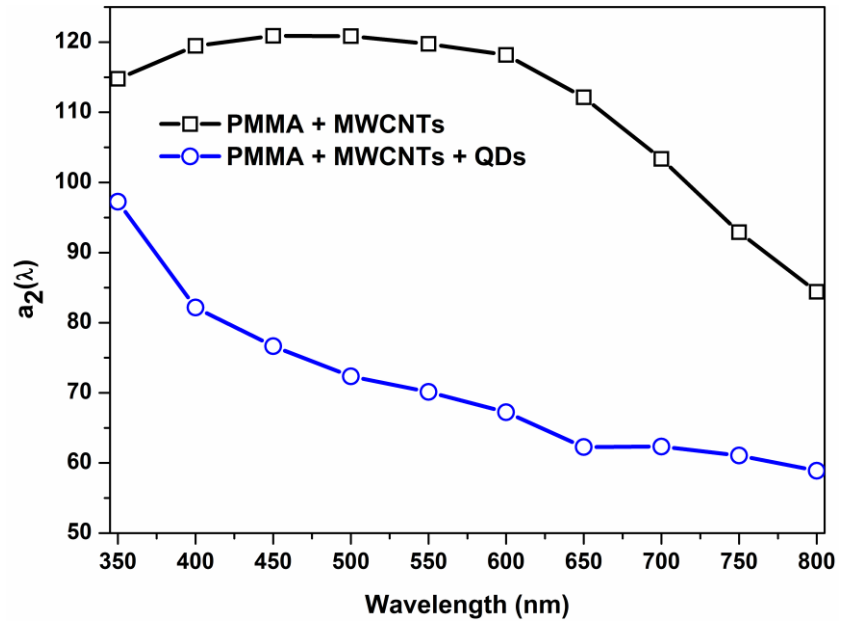


**Fig. 8.** Wavelength dependence of the  $a_2(\lambda)$  coefficient for normalized transmittance for the PMMA/CNT thin films with and without QDs.

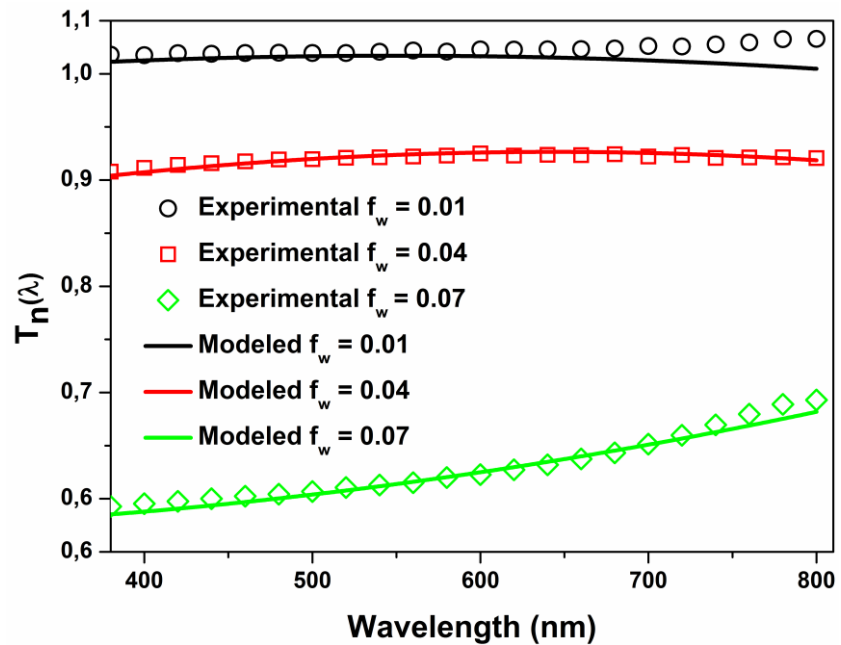


**Fig. 9.** Measured and simulated wavelength dependence of the light transmittance of PMMA/CNT thin films without QDs.



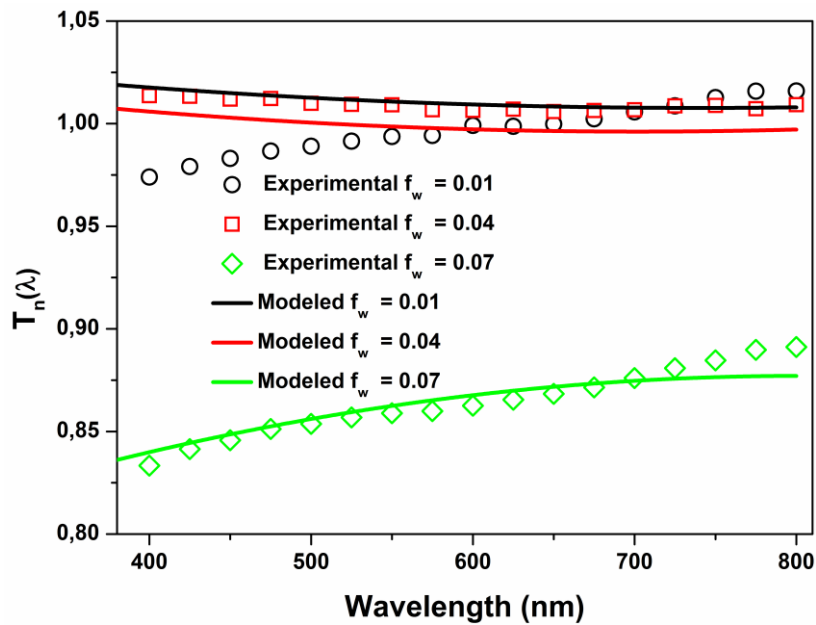


Fig. 10. Measured and simulated wavelength dependence of the light transmittance of PMMA/CNT thin films with QDs.

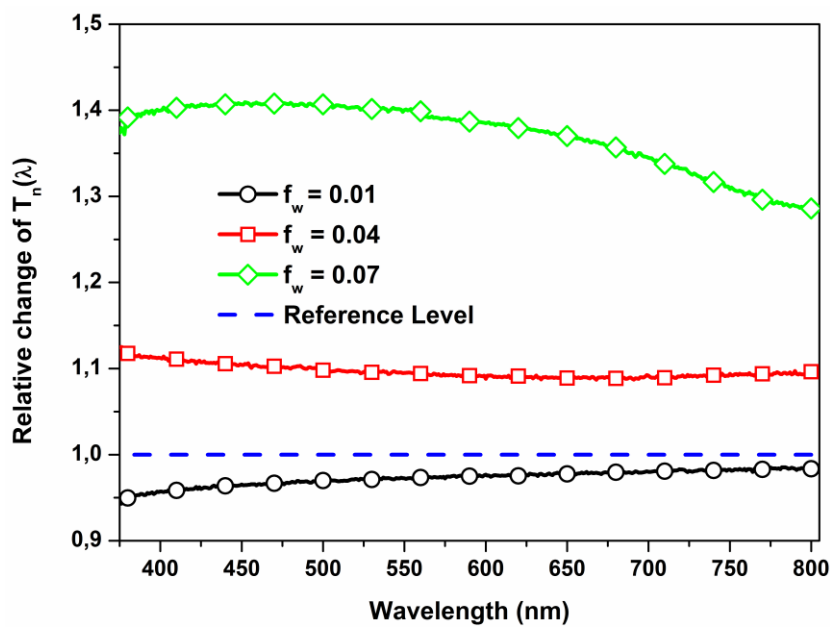
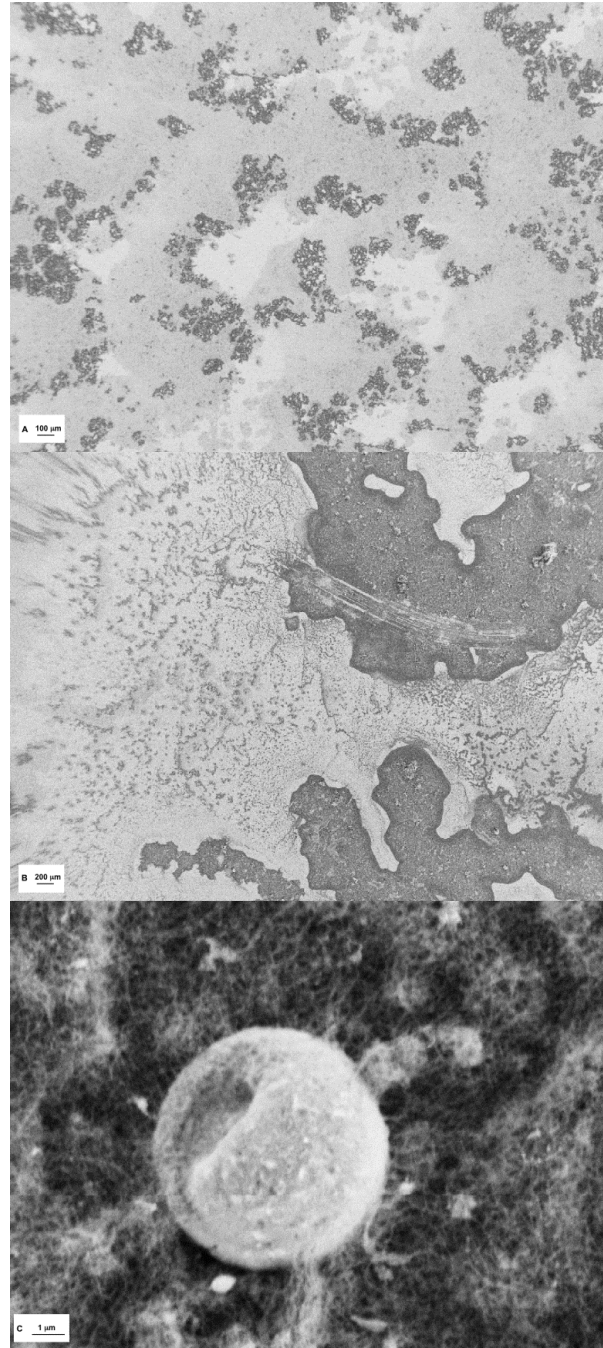


Fig. 11. Optical transmittance of the films with QDs and various CNT concentrations normalized to the optical transmittance of the respective film without QDs.



**Fig. 12.** SEM images of the samples with QDs and (a) 4% CNTs and (b-c) 7% CNTs.

This leads to an overall higher transmittance as compared to the more homogeneous films without QDs. In order to verify this hypothesis, we investigated the film morphology by SEM imaging. In Fig. 12 SEM images of PMMA/MWCNTs/QDs thin film with high CNT concentrations are shown. In the films with CNT weight fractions of 4% and 7% respectively, indeed a rather inhomogeneous distribution of the CNTs can be observed.

### **5.2.3. Electrical characterization of hetero-diodes with organic emitter**

Even if the present article is concentrated on the optical properties of the nanocomposite material, we add a result regarding the electrical properties of the organic material, that helps to understand some of the optical results, discussed above. Organic/inorganic hetero-diodes have been prepared by spin-coating the PMMA + MWCNTs and the PMMA + MWCNTs + QDs thin films on top of a highly doped n-type crystalline silicon (c-Si) substrate. The natural oxide on the Silicon wafers has been removed prior to the spin-coating process with a 2 s dip in 48% fluoridic acid (HF) and the substrates have subsequently been rinsed for 2 min with distilled water and then dried with nitrogen. Full area back contacts and small area front contacts (about  $2.5 \text{ mm}^2$ ) have been added using silver paste. While we did not succeed in producing electrically stable hetero-diodes with organic emitters based on the combination of PMMA, MWCNT and InP/ZnS quantum dots, we obtained reproducible results using a nanocomposite emitter without quantum dots and again different concentrations of multi-walled carbon nanotubes.

The resulting current–voltage characteristics for the devices with different CNT content are shown in Fig. 13. We observe a diode behavior with asymmetric forward and reverse bias current values and a rectification ratio of about 10 for the films with CNT addition, while in the observed voltage range for the device with pure PMMA emitter has current values below  $10^{-9} \text{ A}$ . This confirms also the good isolating properties of the organic matrix. The inset of conduction in forward and reverse bias direction lowers monotonically with the increase of the CNT content. In Fig. 14 the development of two fundamental diode characteristics, namely the ideality factor ( $n$ ) and the diode

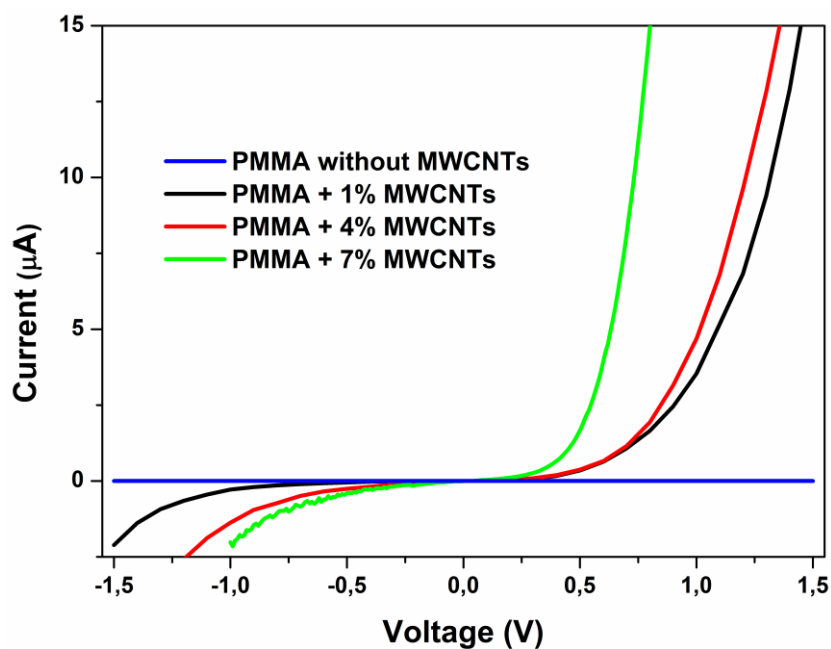


Fig. 13. Current–voltage characteristics PMMA (+CNT) on n-type crystalline Silicon heterojunction diode with and without different CNT concentrations.

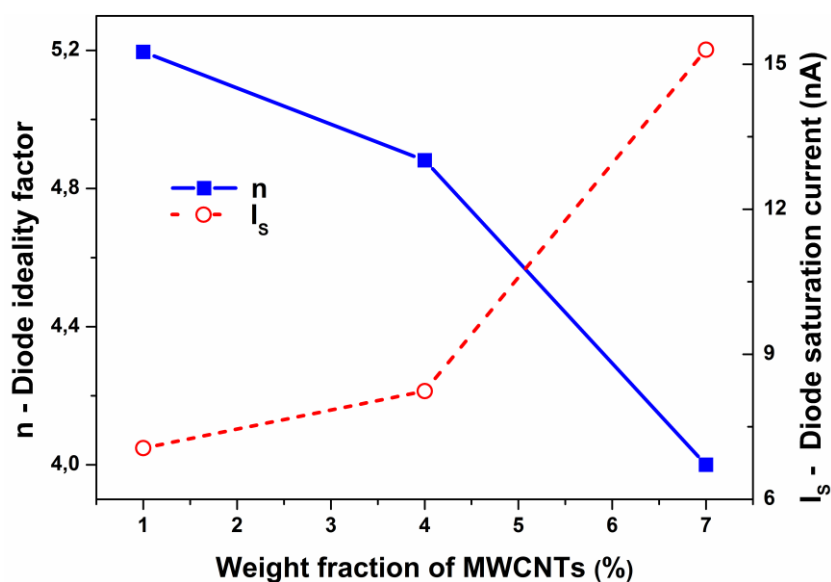


Fig. 14. Diode ideality factor and diode saturation current as a function of the CNT concentrations.

saturation current ( $I_s$ ) are shown as a function of the CNT concentration is shown. The ideality factor decreases monotonically from a value of 5.2 for the device with 1% CNTs to a value of 4.0 for the device with 7% CNTs and the diode saturation currents increase from  $7 \times 10^{-8}$  A to  $1.5 \times 10^{-9}$  A.

These values are reasonable for hetero-diodes with a crystalline silicon base, including also an isolation layer and in fact the here prepared devices can be seen as a mixture between a Silicon/CNT Schottky diode and an MIS diode. In literature, we find for example ideality factors higher than 2 for polyaniline/crystalline silicon heterojunctions [128].

Demonstrated by our results, the Schottky diode character becomes stronger with increasing CNT concentration. The PMMA polymer matrix serves only for the stabilization of the carbon nanotube network and does not contribute to the conduction.

### 5.3. Summary

Thin films, deposited by spin-coating, based on the incorporation of InP/ZnS quantum dots together with different concentrations of multi-walled carbon nanotubes in an isolating PMMA matrix have been characterized using optical transmittance and photoluminescence measurements. The optical transmittance in the visible range of the composite films with and without QDs can be described by an optical model expressed by second order polynomial equations. The addition of the QDs to the PMMA/MWCNTs matrix results, for the films with CNT concentrations higher than 1%, in an increase of the normalized optical transmittance with respect to the same film without quantum dot addition, thus giving an indication for the morphological inhomogeneity of the films. Only for the thin film with 1% CNTs and 5% of InP/ZnS QDs a strong photoluminescence signal related to the quantum dots has been observed. Only with the films without quantum dot addition we could realize stable crystalline Silicon/organic emitter hetero-diodes and the inset of forward bias conduction has been monotonically lowered with increasing CNT content.



## Conclusions

A non-destructive characterization technique, based on low-frequency noise spectroscopy, has been implemented in order to describe the diffusion and the recombination mechanisms in organic electronic devices. Important material parameters, i.e. the charge carrier lifetime and mobility, have been extracted directly from the noise spectra. In addition, it has been shown, that the noise analysis is very sensitive to the active layer and/or interface modifications and can be used as a new tool to optimize the process parameters of polymer solar cells.

In order to enhance the light absorption of the active layer in the red and infrared spectral region of organic solar cells, the addition of InP/ZnS quantum dots into the active polymeric layer have been considered. Because in this case, however, effective charge carrier transport is only possible for high concentrations of quantum dots, an alternative way has been considered, by combining the quantum dots with carbon nanotubes. As a first investigation, the interplay between quantum dots and nanotubes has been investigated by inserting them into an isolating matrix polymer, namely PMMA. Thin films of these composites have been deposited by spin-coating on glass and crystalline silicon substrates. A simple numerical model for the optical transmittance as a function of nanotube content has been developed. Furthermore a strong correlation between morphological inhomogeneities and the concentration of nanoparticles has been found. Only for the thin films with quantum dots and low content of carbon nanotube a photoluminescence signal could be detected. In addition, the electrical characterization of test heterodiode structures with silicon base and PMMA/CNT emitter has been done. A Schottky type model could be successfully applied to explain the resulting hetero-diodes characteristics for a series of devices with different carbon nanotube content.

A new blue emitting and ambipolar small molecule based on oxadiazole and carbazole molecules with a central Zn-atom has been synthesized and characterized regarding its optical and electrical properties. Again a heterodiode test structure with the organic, small molecule based, emitter deposited by solution-processing on top of the crystalline silicon base has been fabricated. The transport and

dielectric properties have been evaluated by capacitance and current-voltage measurements. Furthermore, the lateral charge carrier mobility has been measured with an organic bottom-gate field effect transistor and compared to the vertical mobility, measured on the heterodiode by space charge limited current analysis.



# Bibliography

- [1] G. Hadziioannou, P. van Putten, *Semiconducting Polymers*, Wiley-VCH, Weinheim, 2000.
- [2] J.H. Burroughs, D.D.C. Bradley, A.R. Brown, R.N. Marks, K. Mackay, R.H. Friend, P.L. Burns, A.B. Holmes, Light-emitting diodes based on conjugated polymers, *Nature*, **347**, 539, (1990).
- [3] R. Gaudiana, C. Brabec, Organic materials: fantastic plastic, *Nature Photonics*, **2**, 287, (2008).
- [4] G. Dennler, M. C. Scharber, C. J. Brabec, Polymer-fullerene bulk-heterojunction solar cells, *Advanced Materials*, **21**, 1323, (2009).
- [5] G.A. Chamberlain, Organic solar cells: a review, *Solar Cells*, **8**, 47, (1983).
- [6] C.W. Tang, Two-layer organic photovoltaic cell, *Applied Physics Letters*, **48**, 183, (1986).
- [7] G. Yu, J. Gao, J.C. Hummelen, F. Wudl, A.J. Heeger, Polymer photovoltaic cells: enhanced efficiencies via a network of internal donor-acceptor heterojunctions, *Science*, **270**, 1789, (1995).
- [8] W. Ma, C. Yang, X. Gong, K. Lee, A. J. Heeger, Thermally stable, efficient polymer solar cells with nanoscale control of the interpenetrating network morphology, *Advanced Functional Materials*, **15**, 1617, (2005).
- [9] G. Li, R. Zhu, Y. Yang, Polymer solar cells, *Nature Photonics*, **6**, 153, (2012).
- [10] Z. He, C. Zhong, S. Su, M. Xu, H. Wu, Y. Cao, Enhanced power-conversion efficiency in polymer solar cells using an inverted device structure, *Nature Photonics*, **6**, 591, (2012).
- [11] Y. Liang, Z. Xu, J. Xia, S. T. Tsai, Y. Wu, G. Li, C. Ray, L. Yu, For the bright future-bulk heterojunction polymer solar cells with power conversion efficiency of 7.4%, *Advanced Materials*, **22**, E135, (2010).
- [12] M. Skompska, Hybrid conjugated polymer/semiconductor photovoltaic cells, *Synthetic Metals*, **160**, 1, (2010).
- [13] L. E. Brus, Electron-electron and electron-hole interactions in small semiconductor crystallites: The size dependence of the lowest excited electronic state, *The Journal of Chemical Physics*, **80**, 4403, (1984).

- [14] N. C. Greenham, X. Peng, A. P. Alivisatos, Charge separation and transport in conjugated-polymer/semiconductor-nanocrystal composites studied by photoluminescence quenching and photoconductivity, *Physica B: Condensed Matter*, **54**, 17628, (1996).
- [15] Y. Zhou, M. Eck, C. Veit, B. Zimmermann, F. Rauscher, P. Niyamakom, S. Yilmaz, I. Dumsch, S. Allard, U. Scherff, M. Krüger, Efficiency enhancement for bulk-heterojunction hybrid solar cells based on acid treated CdSe quantum dots and low bandgap polymer PCPDTBT, *Solar Energy Materials and Solar Cells*, **95**, 1232, (2011).
- [16] S. Ravindran, S. Chaudhary, B. Colburn, M. Ozkan, C. S. Ozkan, Covalent Coupling of Quantum Dots to Multiwalled Carbon Nanotubes for Electronic Device Applications, *Nano Letters*, **3**, 447, (2003).
- [17] D. Wang, Baral J. K., H. Zhao, B. A. Gonfa, V. V. Truong, M. A. El Khakani, R. Izquierdo, D. Ma, Controlled Fabrication of PbS Quantum-Dot/Carbon-Nanotube Nanoarchitecture and its Significant Contribution to Near-Infrared Photon-to-Current Conversion, *Advanced Functional Materials*, **21**, 4010, (2011).
- [18] J. Wang, Z. Fang, A. Gu, Effect of multi-walled carbon nanotubes dispersity on the light transmittancy of multi-walled carbon nanotubes/epoxy composites, *Polymer Engineering and Science*, **46**, 635, (2006).
- [19] C. J. Brabec, S. Gowrisanker, J. J. M. Halls, D. Laird, S. Jia, S. P. Williams, Polymer–Fullerene Bulk-Heterojunction Solar Cells, *Advanced Materials*, **22**, 3839, (2010).
- [20] R. A. Street, Carrier mobility, structural order, and solar cell efficiency of organic heterojunction devices, *Applied Physics Letters*, **93**, 133308, (2008).
- [21] M. Hallermann, I. Kriegel, E. Da Como, J.M. Berger, E. von Hauff, J. Feldmann, Charge Transfer Excitons in Polymer/Fullerene Blends: The Role of Morphology and Polymer Chain Conformation, *Advanced Functional Materials*, **19**, 3662, (2009).
- [22] T.M. Clarke, J.R. Durrant, Charge photogeneration in organic solar cells, *Chemical Reviews*, **110**, 6736, (2010).
- [23] F. C. Chen, H. C. Tseng, C. J. Ko, Solvent mixtures for improving device efficiency of polymer photovoltaic devices, *Applied Physics Letters*, **92**, 103316, (2008).
- [24] L. Li, H. Tang, H. Wu, G. Lu, X. Yang, Effects of Fullerene Solubility on the Crystallization of Poly(3-hexylthiophene) and Performance of Photovoltaic Devices, *Organic Electronics*, **10**, 1334, (2009).

- [25] A. Moulé, K. Meerholtz, Controlling Morphology in Polymer–Fullerene Mixtures, *Advanced Materials*, **20**, 240, (2008).
- [26] C. Barone, S. Pagano, H. C. Neitzert, Effect of concentration on low-frequency noise of multi-wall carbon nanotubes in high-density polyethylene matrix, *Applied Physics Letters*, **97**, 152107, (2010).
- [27] R. Macku P. Koktavy, Analysis of fluctuation processes in forward-biased solar cells using noise spectroscopy, *Physica Status Solidi A*, **207**, 2387, (2010).
- [28] V. N. Savvate'ev, A. V. Yakimov, D. Davidov, R. M. Pogreb, R. Neumann, Y. Avny, Degradation of nonencapsulated polymer-based light-emitting diodes: Noise and morphology, *Applied Physics Letters*, **71**, 3344, (1997).
- [29] M. Bag, N. S. Vidhyadhiraja, K. S. Narayan, Fluctuations in photocurrent of bulk heterojunction polymer solar cells-A valuable tool to understand microscopic and degradation processes, *Applied Physics Letters*, **101**, 043903, (2012).
- [30] L.H. Nguyen, H. Hoppe, T. Erb, S. Günes, G. Gobsch, N.S. Sariciftci, Effects of Annealing on the Nanomorphology and Performance of Poly(alkylthiophene):Fullerene Bulk-Heterojunction Solar Cells, *Advanced Functional Materials*, **17**, 1071, (2007).
- [31] Y. Kim, S.A. Choulis, J. Nelson, D.D.C. Bradley, S. Cook, J.R. Durrant, Device annealing effect in organic solar cells with blends of regioregular poly(3-hexylthiophene) and soluble fullerene, *Applied Physics Letters*, **86**, 063502, (2005).
- [32] H. Hoppe, N. S. Sariciftci, Morphology of polymer/fullerene bulk heterojunction solar cells, *Journal of Materials Chemistry*, **16**, 45, (2006).
- [33] M. Reyes-Reyes, K. Kim, D. L. Carroll, High-efficiency photovoltaic devices based on annealed poly(3-hexylthiophene) and 1-(3-methoxycarbonyl)propyl-1- phenyl-(6,6)C<sub>61</sub> blends, *Applied Physics Letters*, **87**, 083506, (2005).
- [34] V. Bugatti, S. Concilio, P. Iannelli, S.P. Piotto, S. Bellone, M. Ferrara, H.C. Neitzert, A. Rubino, D. Della Sala, P. Vacca, Synthesis and characterization of new electroluminescent molecules containing carbazole and oxadiazole units, *Synthetic Metals*, **156**, 13, (2006).
- [35] M. H. Ho, M. Y. Liu, K. H. Lin, C. H. Chen, C. W. Tang, *SID Symposium Digest of Technical Papers*, **4**, 552, (2010).
- [36] A. N. Aleshin, E. L. Alexandrova, I. P. Shcherbakov, Electrical and optical properties of composites based on carbazole derivatives and silicon particles, *Physics of the Solid State*, **50**, 972, (2008).

- [37] D. H. Wang, J. S. Moon, J. Seifert, J. Jo, J. H. Park, O. O. Park, A. J. Heeger, Sequential processing: control of nanomorphology in bulk heterojunction solar cells, *Nano Letters*, **11**, 3163, (2011).
- [38] N. S. Sariciftci, L. Smilowitz, A. J. Heeger, F. Wudl, Photoinduced electron transfer from a conducting polymer to buckminsterfullerene, *Science*, **258**, 1474, (1992).
- [39] H. C. Neitzert, S. Concilio, P. Iannelli, P. Vacca, Electronic memory effect in a crystalline silicon/polyether heterostructure, *Physica Status Solidi C*, **7**, 988, (2010).
- [40] M. R. Lee, R. D. Eckert, K. Forberich, G. Dennler, C. J. Brabec, R. A. Gaudiana, Solar Power Wires Based on Organic Photovoltaic Materials, *Science*, **324**, 232, (2009).
- [41] B. E. Lassiter, J. D. Zimmerman, A. Panda, X. Xiao, S. R. Forrest, Tandem organic photovoltaics using both solution and vacuum deposited small molecules, *Applied Physics Letters*, **101**, 063303, (2012).
- [42] S. Grecu, M. Bronner, A. Opitz, W. Brutting, Characterization of polymeric metal-insulator-semiconductor diodes, *Synthetic Metals*, **146**, 359, (2004).
- [43] S. Steinberger, A. Mishra, E. Reinold, C. M. Müller, C. Urich, M. Pfeiffer, P. Bäuerle, A-D-A-D-A-type oligothiophenes for vacuum-deposited organic solar cells, *Organic Letters*, **13**, 90, (2010).
- [44] J. Meiss, F. Holzmueller, R. Gresser, K. Leo, M. Riede, Highly efficient semitransparent tandem organic solar cells with complementary absorber materials, *Applied Physics Letters*, **99**, 043301, (2011).
- [45] R. Fitzner, E. Reinold, A. Mishra, E. Mena-Osteritz, H. Ziehlke, C. Körner, K. Leo, M. Riede, M. Weil, O. Tsaryova, A. Weiß, C. Urich, M. Pfeiffer, P. Bäuerle, Dicyanovinyl-Substituted Oligothiophenes: Structure-Property Relationships and Application in Vacuum-Processed Small Molecule Organic Solar Cells, *Advanced Functional Materials*, **21**, 897, (2011).
- [46] H. C. Neitzert, S. Concilio, P. Iannelli, P. Vacca, Photocurrent Spectroscopy of UV-Photodiodes with an Active Layer consisting of small molecules that combine Oxadiazole and Carbazole groups, *AIP Conference Proceedings*, **1199**, 139 (2009).
- [47] H. C. Neitzert, S. Schwertheim, K. Meusinger, M. Leinhos, W. R. Fahrner, Heterojunction solar cell fabricated by spin-coating of a CNT/PEDOT:PSS heteroemitter on top of a crystalline silicon absorber, *Nanotechnology. IV, SPIE Proc. Ser.*, **7364**, 73640L, (2009).

- [48] D. Acierno, S. Concilio, A. Diodati, P. Iannelli, S. P. Piotta, P. Scarfato, Synthesis and liquid crystalline properties of low molecular mass compounds containing the 1,4-bis(5-phenyl-1,3,4-oxadiazolyl)benzene unit, *Liquid Crystals*, **29**, 1383, (2002).
- [49] D. Acierno, E. Amendola, S. Bellone, S. Concilio, P. Iannelli, H. C. Neitzert, A. Rubino, F. Villani, Synthesis and characterization of a new class of nematic photoluminescent oxadiazole-containing polyethers, *Macromolecules*, **36**, 6410, (2003).
- [50] S. Concilio, V. Bugatti, P. Iannelli, S. P. Piotta, Synthesis and characterization of new photoluminescent oxadiazole/carbazole-containing polymers, *International Journal of Polymer Science*, **2010**, 1, (2010).
- [51] W. Wang, E. A. Schiff, Polyaniline on crystalline silicon heterojunction solar cells, *Applied Physics Letters*, **91**, 133504, (2007).
- [52] G. Wang, Y. He, New oxadiazole complex with bipolar ligand for organic light-emitting devices, *Materials Letters*, **63**, 470, (2009).
- [53] H. Xu, Z. F. Xu, Z. Y. Yue, P. F. Yan, B. Wang, L. W. Jia, G. M. Li, W. B. Sun, J. W. Zhang, A Novel Deep Blue-Emitting Zn<sup>II</sup> Complex Based on Carbazole-Modified 2-(2-Hydroxyphenyl)benzimidazole: Synthesis, Bright Electroluminescence, and Substitution Effect on Photoluminescent, Thermal and Electrochemical Properties, *The Journal of Physical Chemistry C*, **112**, 15517, (2008).
- [54] M. S. A. Abdou, F. P. Orfino, Y. Son, S. Holdcroft, Interaction of Oxygen with Conjugated Polymers: Charge Transfer Complex Formation with Poly(3-alkylthiophenes), *Journal of the American Chemical Society*, **119**, 4518, (1997).
- [55] S. Hoshino, M. Yoshida, S. Uemura, T. Kodzasa, N. Takada, T. Kamata, K. Yase, Influence of moisture on device characteristics of polythiophene-based field-effect transistors, *Journal of Applied Physics*, **95**, 5088, (2004).
- [56] G. Garcia-Belmonte, A. Munar, E. M. Barea, J. Bisquert, I. Ugarte, R. Pacios, Charge carrier mobility and lifetime of organic bulk heterojunctions analyzed by impedance spectroscopy, *Organic Electronics*, **9**, 847, (2008).
- [57] G. Garcia-Belmonte, J. Bisquert, G. Popkurov, Determination of the electronic conductivity of polybithiophene films at different doping levels using in situ electrochemical impedance measurements, *Applied Physics Letters*, **83**, 2178, (2003).

- [58] L. Li, H. Tang, H. Wu, G. Lu, X. Yang, Effects of fullerene solubility on the crystallization of poly(3-hexylthiophene) and performance of photovoltaic devices, *Organic Electronics*, **10**, 1334, (2009).
- [59] A. De Sio, T. Madena, R. Huber, J. Parisi, S. Neyshtadt, F. Deschler, E. Da Como, S. Esposito, E. von Hauff, Solvent additives for tuning the photovoltaic properties of polymer-fullerene solar cells, *Solar Energy Materials and Solar Cells*, **95**, 3536, (2011).
- [60] C. Barone, A. Galdi, S. Pagano, O. Quaranta, L. Méchin, J. M. Routoure, P. Perna, Experimental technique for reducing contact and background noise in voltage spectral density measurements, *Review of Scientific Instruments*, **78**, 093905, (2007).
- [61] T. Ripolles-Sanchis, A. Guerrero, J. Bisquert, G. Garcia-Belmonte, Diffusion-Recombination Determines Collected Current and Voltage in Polymer:Fullerene Solar Cells, *The Journal of Physical Chemistry C*, **116**, 16925, (2012).
- [62] G. Perrier, R. de Bettignies, S. Berson, N. Lemaître, S. Guillerez, Impedance spectrometry of optimized standard and inverted P3HT-PCBM organic solar cells, *Solar Energy Materials and Solar Cells*, **101**, 210 (2012).
- [63] T. Kuwabara, C. Iwata, T. Yamaguchi, K. Takahashi, Mechanistic insights into UV-induced electron transfer from PCBM to titanium oxide in inverted-type organic thin film solar cells using AC impedance spectroscopy, *ACS Applied Materials and Interfaces*, **2**, 2254, (2010).
- [64] P.P. Boix, A. Guerrero, L.F. Marchesi, G. Garcia-Belmonte, J. Bisquert, Current-voltage characteristics of bulk hetero-junction organic solar cells: connection between light and dark curves, *Advanced Energy Materials*, **1**, 1073, (2011).
- [65] A. Guerrero, T. Ripolles-Sanchis, P. P. Boix, G. Garcia-Belmonte, Series resistance in organic bulk-heterojunction solar devices: modulating carrier transport with fullerene electron traps, *Organic Electronics*, **13**, 2326, (2012).
- [66] A. Guerrero, L. F. Marchesi, P. P. Boix, S. Ruiz-Raga, T. Ripolles-Sanchis, G. Garcia-Belmonte, J. Bisquert, How the charge-neutrality level of interface states controls energy level alignment in cathode contacts of organic bulk-heterojunction solar cells, *ACS Nano*, **6**, 3453, (2012).
- [67] S. Kogan, *Electronic Noise and Fluctuations in Solids*, Cambridge University Press, Cambridge, 1996.

- [68] G. Landi, C. Barone, A. De Sio, S. Pagano, H. C. Neitzert, Characterization of polymer:fullerene solar cells by low-frequency noise spectroscopy, *Applied Physics Letters*, **102**, 223902, (2013).
- [69] Z. Pomerantz, A. Zaban, S. Ghosh, J.-P. Lellouche, G. Garcia-Belmonte, J. Bisquert., Capacitance spectroelectrochemistry and conductivity of polarons and bipolarons in a polydicarbazole based conducting polymer, *Journal of Electroanalytical Chemistry*, **614**, 49, (2008).
- [70] H. Bässler, Charge Transport in Disordered Organic Photoconductors a Monte Carlo Simulation Study, *Physica Status Solidi B*, **175**, 15, (1993).
- [71] G. Garcia.-Belmonte, Carrier recombination flux in bulk heterojunction polymer:fullerene solar cells: Effect of energy disorder on ideality factor, *Solid-State Electronics*, **79**, 201, (2013).
- [72] P. Dutta, P. M. Horn, Low-frequency fluctuations in solids: 1/f noise, *Reviews of Modern Physics*, **53**, 497, (1981).
- [73] C. Bonavolontà, C. Albonetti, M. Barra, M. Valentino, Electrical mobility in organic thin-film transistors determined by noise spectroscopy, *Journal of Applied Physics*, **110**, 093716, (2011).
- [74] T. Tromholt, M. Manceau, M. Helgesen, J. E. Carlé, F. C. Krebs, Degradation of semiconducting polymers by concentrated sunlight, *Solar Energy Materials and Solar Cells*, **95**, 1308, (2011).
- [75] M. O. Reese, A. M. Nardes, B. L. Rupert, R. E. Larsen, D. C. Olson, M. T. Lloyd, S. E. Shaheen, D. S. Ginley, G. Rumbles, N. Kopidakis, Photoinduced degradation of polymer and polymerfullerene active layers: experiment and theory, *Advanced Functional Materials*, **20**, 3476, (2010).
- [76] F. Deschler, A. De Sio, E. von Hauff, P. Kutka, T. Sauermann, H. J. Egelhaaf, J. Hauch, E. Da Como, The effect of aging on exciton dynamics, charge separation, and recombination in P3HT/PCBM photovoltaic blends, *Advanced Functional Materials*, **22**, 1461, (2012).
- [77] S. Bertho, B. Campo, F. Piersimoni, D. Spoltore, J. D'Haen, L. Lutsen, W. Maes, D. Vanderzande, J. Manca, Improved thermal stability of bulk heterojunctions based on side-chain functionalized poly(3-alkylthiophene) copolymers and PCBM, *Solar Energy Materials and Solar Cells*, **110**, 69, (2013).
- [78] S. Lilliu, T. Agostinelli, E. Pires, M. Hampton, J. Nelson, J. E. Macdonald, Dynamics of crystallization and disorder during annealing of P3HT/PCBM bulk heterojunctions, *Macromolecules*, **44**, 2725, (2011).

- [79] W. C. Tsoi, S. J. Spencer, L. Yang, A. M. Ballantyne, P. G. Nicholson, A. Turnbull, A. G. Shard, C. E. Murphy, D. D. C. Bradley, J. Nelson, J. S. Kim, Effect of crystallization on the electronic energy levels and thin film morphology of P3HT:PCBM blends, *Macromolecules*, **44**, 2944, (2011).
- [80] M. Jørgensen, K. Norrman, F. C. Krebs, Stability/degradation of polymer solar cells, *Solar Energy Materials and Solar Cells*, **92**, 686, (2008).
- [81] H. Hintz, H. Peisert, H. J. Egelhaaf, T. Chassé, Reversible and irreversible light-induced p-doping of P3HT by oxygen studied by photoelectron spectroscopy (XPS/UPS), *Journal of Physical Chemistry C*, **115**, 13373, (2011).
- [82] C. Barone, C. Adamo, A. Galdi, P. Orgiani, A. Yu. Petrov, O. Quaranta, L. Maritato, S. Pagano, Unusual current dependence of resistance and voltage noise in  $\text{La}_{1-x}\text{Sr}_x\text{MnO}_3$  ultra-thin films, *Physical Review B*, **75**, 174431, (2007).
- [83] C. Barone, S. Pagano, I. Pallecchi, E. Bellingeri, M. Putti, C. Ferdeghini, Thermally and voltage activated excess 1/f noise in  $\text{FeTe}_{0.5}\text{Se}_{0.5}$  epitaxial thin films, *Physical Review B*, **83**, 134523, (2011).
- [84] A. A. Balandin, Low-frequency 1/f noise in graphene devices, *Nature Nanotechnology*, **8**, 549, (2013).
- [85] G. Garcia-Belmonte, P. P. Boix, J. Bisquert, M. Lenes, H. J. Bolink, A. La Rosa, S. Filippone, N. Martín, Influence of the Intermediate Density-of-States Occupancy on Open-Circuit Voltage of Bulk Heterojunction Solar Cells with Different Fullerene Acceptors, *Journal of Physical Chemistry Letters*, **1**, 2566, (2010).
- [86] T. G. M. Kleinpenning, Comment on “Low-frequency excess noise in  $\text{Nb-A}_{12}\text{O}_3\text{-Nb}$  Josephson tunnel junctions”, *Applied Physics Letters*, **50**, 1757, (1987)], *Applied Physics Letters*, **52**, 2001, (1988).
- [87] P. P. Boix, J. Ajuria, I. Etxebarria, R. Pacios, G. Garcia-Belmonte, J. Bisquert, Role of ZnO Electron-Selective Layers in Regular and Inverted Bulk Heterojunction Solar Cells, *Journal of Physical Chemistry Letters*, **2**, 407 (2011).
- [88] J. Bisquert, G. Garcia-Belmonte, J. Garcia-Canadas, Effects of the Gaussian energy dispersion on the statistics of polarons and bipolarons in conducting polymers, *The Journal of Chemical Physics*, **120**, 6726, (2004).
- [89] G. Garcia-Belmonte, P. P. Boix, J. Bisquert, M. Sessolo, H. J. Bolink, Influence of the Intermediate Density-of-States Occupancy on Open-Circuit Voltage of Bulk Heterojunction Solar Cells with Different Fullerene Acceptors, *Solar Energy Materials and Solar Cells*, **94**, 366, (2010).



- [90] T. Moehl, V. G. Kytin, J. Bisquert, M. Kunst, H. J. Bolink, G. Garcia-Belmonte, Relaxation of Photogenerated Carriers in P3HT:PCBM Organic Blends, *ChemSusChem*, **2**, 314, (2009).
- [91] P. P. Boix, G. Garcia-Belmonte, U. Munecas, M. Neophytou, C. Waldauf, R. Pacios, Determination of gap defect states in organic bulk heterojunction solar cells from capacitance measurements, *Applied Physics Letters*, **95**, 233302, (2009).
- [92] G. Dennler, A. J. Mozer, G. Juska, A. Pivrikas, R. Å Osterbacka, A. Fuchsbauer, N. S. Saricifti, Charge carrier mobility and lifetime versus composition of conjugated polymer/fullerene bulk-heterojunction solar cells, *Organic Electronics*, **7**, 229 (2006).
- [93] M. G. Helander, Z. B. Wang, J. Qiu, Z. H. Lu, Band alignment at metal/organic and metal/oxide/organic interfaces, *Applied Physics Letters*, **93**, 193310, (2008).
- [94] G. Li, V. Shrotriya, Y. Yao, Y. Yang, Investigation of annealing effects and film thickness dependence of polymer solar cells based on poly(3-hexylthiophene), *Journal of Applied Physics*, **98**, 043704, (2005).
- [95] T. Kirchartz, W. Gong, S. A. Hawks, T. Agostinelli, R. C. I. MacKenzie, Y. Yang, J. Nelson, Sensitivity of the Mott-Schottky analysis in organic solar cells, *Journal of Physical Chemistry C*, **116**, 7672, (2012).
- [96] S. M. Sze, K. K. Ng, *Physics of Semiconductor Devices*, Wiley-Interscience, New Jersey, 2007.
- [97] K. Norrman, S. A. Gevorgyan, F. C. Krebs, Water-induced degradation of polymer solar cells studied by H<sub>2</sub><sup>18</sup>O labeling, *Applied Materials and Interfaces*, **1**, 102, (2009).
- [98] M. Manceau, A. Rivaton, J. L. Gardette, S. Guillerez, N. Lemaître, The mechanism of photo- and thermooxidation of poly(3-hexylthiophene) (P3HT) reconsidered, *Polymer Degradation and Stability*, **94**, 898, (2009).
- [99] F. Yakuphanoglu, R. S. Anand, Charge transport properties of an organic solar cell, *Synthetic Metals*, **160**, 2250, (2010).
- [100] M. Giulianini, E. R. Waclawik, J. M. Bell, N. Motta, Temperature and electric field dependent mobility in poly(3-hexylthiophene) diodes, *Journal of Applied Physics*, **108**, 014512, (2010).
- [101] A. Pivrikas, M. Ullah, H. Sitter, N. S. Sariciftci, Electric field dependent activation energy of electron transport in fullerene diodes and field effect transistors: Gills law, *Applied Physics Letters*, **98**, 092114, (2011).

- [102] J. D. Servaites, M. A. Ratner, T. J. Marks, Organic solar cells: a new look at traditional models, *Energy and Environmental Science*, **4**, 4410, (2011).
- [103] A. L. Ayzner, D. D. Wanger, C. J. Tassone, S. H. Tolbert, B. J. Schwartz, Room to improve conjugated polymer-based solar cells: understanding how thermal annealing affects the fullerene component of a bulk heterojunction photovoltaic device, *Journal of Physical Chemistry C Letters*, **112**, 18711, (2008).
- [104] Z. Xu, L. M. Chen, G. Yang, C. H. Huang, J. Hou, Y. Wu, G. Li, C. S. Hsu, Y. Yang, Vertical phase separation in poly(3-hexylthiophene): fullerene derivative blends and its advantage for inverted structure solar cells, *Advanced Functional Materials*, **19**, 1227, (2009).
- [105] J. Bisquert, G. Garcia-Belmonte, J. Garcia-Cañadas, Effects of the Gaussian energy dispersion on the statistics of polarons and bipolarons in conducting polymers, *The Journal of Chemical Physics*, **120**, 6726, (2004).
- [106] A. V. Tunc, A. De Sio, D. Riedel, F. Deschler, E. Da Como, J. Parisi, E. von Hauff, Molecular doping of low-bandgap-polymer:fullerene solar cells: Effects on transport and solar cells, *Organic Electronics*, **13**, 290, (2012).
- [107] T. V. Sakhno, I.V. Korotkova, O. A. Khakhel, Influence of temperature on quenching of fluorescence in compounds of the coumarin series, *Theoretical and Experimental Chemistry*, **32**, 217, (1996).
- [108] A. M. Goodman, Metal—Semiconductor Barrier Height Measurement by the Differential Capacitance Method—One Carrier System, *Journal of Applied Physics*, **34**, 329, (1963).
- [109] P. Stallinga, H. L. Gomes, H. Rost, A. B. Holmes, M. G. Harrison, R. H. Friend, Minority-carrier effects in poly-phenylenevinylene as studied by electrical characterization, *Journal of Applied Physics*, **89**, 1713, (2001).
- [110] W. G. Osiris, A. A. M. Farag, I. S. Yahia, Extraction of the device parameters of Al/P3OT/ITO organic Schottky diode using J–V and C–V characteristics, *Synthetic Metals*, **161**, 1079, (2011).
- [111] O. Ostroverkhova, *Handbook of Organic Materials for Optical and (Opto)Electronic Devices*, Cambridge: Woodhead Publishing, 2013.
- [112] A. Sharma, P. Kumar, B. Singh, S. R. Chaudhuri, S. Ghosh, Capacitance-voltage characteristics of organic Schottky diode with and without deep traps, *Applied Physics Letters*, **99**, 2, 023301, (2011).
- [113] I. H. Campbell, D. L. Smith, J. P. Ferraris, Electrical impedance measurements of polymer light-emitting diodes, *Applied Physics Letters*, **66**, 3030, (1995).

- [114] L. Zhang, H. Nakanotani, C. Adachi, Capacitance-voltage characteristics of a 4,4'-bis[(N-carbazole)styryl]biphenyl based organic light-emitting diode: Implications for characteristic times and their distribution, *Applied Physics Letters*, **103**, 093301 (2013).
- [115] S. Concilio, V. Bugatti, H. C. Neitzert, G. Landi, A. De Sio, J. Parisi, S. Piotto, P. Iannelli, Zn-complex based on oxadiazole/carbazole structure: Synthesis, optical and electric properties, *Thin Solid Films*, **556**, 419, (2014).
- [116] V. Gupta, A. K. K. Kyaw, D. Hwan Wang, S. Chand, G. C. Bazan, A. J. Heeger, Barium: An Efficient Cathode Layer for Bulk-heterojunction Solar Cells, *Scientific Reports*, **3**, 1965, (2013).
- [117] Z. B. Wang, M. G. Helander, M. T. Greiner, J. Qiu, Z. H. Lu, Carrier mobility of organic semiconductors based on current-voltage characteristics, *Journal of Applied Physics*, **107**, 034506, (2010).
- [118] A. N. Aleshin, J. Y. Lee, S. W. Chu, J. S. Kim, Y. W. Park, Mobility studies of field-effect transistor structures based on anthracene single crystals, *Applied Physics Letters*, **84**, 5383, (2004).
- [119] H. Song, S. Lee, Photoluminescent (CdSe)ZnS quantum dot-polymethylmethacrylate polymer composite thin films in the visible spectral range, *Nanotechnology*, **18**, 055402, (2007).
- [120] L. Li, P. Reiss, One-pot synthesis of highly luminescent InP/ZnS nanocrystals without precursor injection, *Journal of the American Chemical Society*, **130**, 11588, (2008).
- [121] H. Chen, H. Muthuraman, P. Stokes, J. Zou, X. Liu, J. Wang, Q. Huo, S. I. Khondaker, L. Zhai, Dispersion of carbon nanotubes and polymer nanocomposite fabrication using trifluoroacetic acid as a co-solvent, *Nanotechnology*, **18**, 415606, (2007).
- [122] D. I. Son, C. H. You, W. T. Kim, J. H. Jung, T. W. Kim, Electrical bistabilities and memory mechanisms of organic bistable devices based on colloidal ZnO quantum dot-polymethylmethacrylate polymer nanocomposites, *Applied Physics Letters*, **94**, 132103, (2009).
- [123] P. K. Khanna, N. Singh, Light emitting CdS quantum dots in PMMA: synthesis and optical studies, *Journal of Luminescence*, **127**, 474, (2007).
- [124] N. G. Semaltianos, Spin-coated PMMA films, *Microelectronics Journal*, **38**, 754, (2007).

- 
- [125] A. Narayanaswamy, L. F. Feiner, P. J. van der Zaag, Temperature Dependence of the Photoluminescence of InP/ZnS Quantum Dots, *Journal of Physical Chemistry C: Nanomaterials and Interfaces*, **112**, 6775, (2008).
- [126] U. T. D. Thuy, P. T. Thuy, N. Q. Liem, L. Li, P. Reiss, Comparative photoluminescence study of close-packed and colloidal InP/ZnS quantum dots, *Applied Physics Letters*, **96**, 073102, (2010).
- [127] V. Biju, T. Itoh, Y. Baba, M. Ishikawa, Quenching of Photoluminescence in Conjugates of Quantum Dots and Single-Walled Carbon Nanotube , *The Journal of Physical Chemistry B*, **110**, 26068, (2006).
- [128] C. H. Chen, I. Shih, Hybrid organic on inorganic semiconductor heterojunction, *Journal of Materials Science: Materials in Electronics*, **17**, 1047, (2006).

## List of publications during the period of the preparation of the doctoral thesis

### Publications directly related to this dissertation

- [1] **G. LANDI**, W. R. FAHRNER, S. CONCILIO, L. SESSA, H. C. NEITZERT, **ELECTRICAL HOLE TRANSPORT PROPERTIES OF AN AMBIPOLAR ORGANIC COMPOUND WITH ZN-ATOMS ON A CRYSTALLINE SILICON HETEROSTRUCTURE**, *IEEE JOURNAL OF THE ELECTRON DEVICES SOCIETY*, 2,179-181, (2014).
- [2] MULTI-WALLED CARBON NANOTUBE NETWORK-BASED SENSORS AND DEVICES WITHOUT AND WITH ORGANIC MATRIX, W. R. FAHRNER, **G. LANDI**, H. C. NEITZERT, R. DI GIACOMO, CHAPTER IN: FECHT, WERNER, VAN DER VOORDE (EDS), **THE NANO-MICRO INTERFACE. BRIDGING THE MICRO AND NANO WORLD**, 2/E WILEY, (2014), *IN PRESS*.
- [3] **G. LANDI**, C. BARONE, S. PAGANO, A. DE SIO, AND H. C. NEITZERT, **INVESTIGATION OF THE SOLVENT INFLUENCE ON POLYMER-FULLERENE SOLAR CELLS BY LOW FREQUENCY NOISE SPECTROSCOPY**, *CANADIAN JOURNAL OF PHYSICS*, 92, 879-882, (2014).
- [4] S. CONCILIO, V. BUGATTI, H. C. NEITZERT, **G. LANDI**, A. DE SIO, J. PARISI, S. PIOTTO, AND P. IANNELLI, **ZN-COMPLEX BASED ON OXADIAZOLE/CARBAZOLE STRUCTURE: SYNTHESIS, OPTICAL AND ELECTRIC PROPERTIES**, *THIN SOLID FILMS*, 556, 419-424, (2014).
- [5] C. BARONE, **G. LANDI**, A. DE SIO, H. C. NEITZERT, AND S. PAGANO, **THERMAL AGING OF BULK HETEROJUNCTION POLYMER SOLAR CELLS INVESTIGATED BY ELECTRIC NOISE ANALYSIS**, *SOLAR ENERGY MATERIALS AND SOLAR CELLS*, 122, 40-45, (2014).
- [6] **G. LANDI**, M. HENNINGER, A. DE GIROLAMO DEL MAURO, C. BORRIELLO, T. DI LUCCIO, AND H. C. NEITZERT, **INVESTIGATION OF THE OPTICAL CHARACTERISTICS OF A COMBINATION OF INP/ZNS-QUANTUM DOTS WITH MWCNTS IN A PMMA MATRIX**, *OPTICAL MATERIALS*, 35, 2490-2495, (2013).

[7] **G. LANDI, C. BARONE, A. DE SIO, S. PAGANO, AND H. C. NEITZERT, CHARACTERIZATION OF POLYMER:FULLERENE SOLAR CELLS BY LOW-FREQUENCY NOISE SPECTROSCOPY, *APPLIED PHYSICS LETTERS*, 102, 223902, (2013).**

## **Other related publications**

[1] **R. DI GIACOMO, B. MARESCA, M. ANGELILLO, G. LANDI, A. LEONE, M. C. VACCARO, C. BOIT, A. PORTA, H. C. NEITZERT, BIO-NANO-COMPOSITE MATERIALS CONSTRUCTED WITH SINGLE CELLS AND CARBON NANOTUBES: MECHANICAL, ELECTRICAL, AND OPTICAL PROPERTIES, *IEEE TRANSACTIONS ON NANOTECHNOLOGY*, 12, 1026-1030, (2013).**

[2] **R. DI GIACOMO, G. LANDI , C. BOIT , AND H. C. NEITZERT, MONITORING OF THE FORMATION OF A PHOTSENSITIVE DEVICE BY ELECTRIC BREAKDOWN OF AN IMPURITY CONTAINING OXIDE IN A MOS CAPACITOR *PROC. SPIE 8249*, 824919, (2012).**

## **Conferences**

[1] **H. C. NEITZERT, G. LANDI, INFLUENCE OF THE METALLIZATION ON THE ELECTRICAL CHARACTERISTICS OF TEMPERATURE SENSORS BASED ON EPOXY/MWCNT COMPOSITES, POSTER PRESENTATION, SECONDO CONVEGNO NAZIONALE SENSORI, ROMA - UNIVERSITÀ LA SAPIENZA 19 - 21 FEBRUARY 2014**

[2] **G. LANDI, K. BROSZIO, F. WÜNSCH, M. KUNST, AND H. C. NEITZERT, EVALUATION OF HIGH EFFICIENT SILICON SOLAR CELLS WITH MONO-CRYSTALLINE SILICON ABSORBER AND THE IMPACT OF HIGH ENERGY PARTICLE DAMAGE BY ELECTROLUMINESCENCE MEASUREMENTS UNDER FORWARD BIAS. SOLAR ENERGY FOR WORLD PEACE, 17-19 AUGUST 2013. ISTANBUL (TURKEY). POSTER PRESENTATION, ABSTRACT BOOK.**

- 
- [3] A. MESCHELOFF, C. BOUNIOUX, **G. LANDI**, M. GABAI, I. VISOLY-FISHER, AND E. A. KATZ. 2012. **LIGHT-INDUCED DEGRADATION IN PHOTOACTIVE LAYER OF ORGANIC SOLAR CELLS STUDIED WITH CONCENTRATED SUNLIGHT**. THE 3RD INTERNATIONAL NANOTECHNOLOGY CONFERENCE & EXHIBITION (NANOISRAEL 2012), TEL-AVIV , ISRAEL . ABSTRACTS, CD-ROM.





## **Acknowledgements**

First and foremost, I owe particular thanks to my supervisor Prof. Dr. Wolfgang R. Fahrner, for the trust he placed in me, and for his constant stimulation. My most sincere appreciation goes to my mentor Prof. Dr. Heinrich Christoph Neitzert for his careful, insightful and efficient supervision during my studies. Without his generous and indispensable help the conduct of the Ph.D. study would have been impossible. I'm very thankful to Prof. Dr. Detlev Hackstein for his help. I owe a particular debt of gratitude to all of my colleagues for their generous support: Dr. Simona Concilio, Dr. Lucia Sessa, Dr. Antonietta De Sio, Dr. Ali Veysel Tunc, Prof. Dr. Jürgen Parisi, Dr. Carlo Barone, Prof. Dr. Sergio Pagano, Mark Henninger, Dr. Anna De Girolamo Del Mauro, Dr. Tiziana Di Luccio, Dr. Carmela Borriello. I offer special thanks to family and friends. This work is dedicated to my wife Anna and my son Alfonso.

Giovanni Landi  
June 2014



# Curriculum Vitae

## Personal items

**First Name:** Giovanni

**Last Name:** Landi

**Nationality:** Italian

**Place of Birth:** Salerno

**Date of Birth:** 22.5.1983

**Address:** Via Madonna di Fatima, 45, 84084, Fisciano (Salerno)

**Tel.:** +39-0892858508

**Mobile phone:** +393292625509

**e-mail:** [landigiova@yahoo.it](mailto:landigiova@yahoo.it)

## Titles of Study

**November 2011:** MSc Degree in Electronic Engineering, received from Salerno University (marks: 110/110 with honours)

**Title of the MSc thesis:** “Intermediate Band Solar Cells based on Chalcogenide material”

**December 2006:** BSc Degree in Electronic Engineering, received from Salerno University (marks: 108/110)

**Title of the BSc thesis:** “Electronic internal of a commercial multivibrator”

**July 2002:** High school degree, received from the High School for Technical Industrial Studies “Basilio Focaccia” in Salerno (marks: 100/100)

## Working Experience

**From 1 October 2011 to 31 December 2011:** Research contract at the Department of Solar Energy and Environmental Physics, J. Blaustein Institutes for Desert Research, Ben-Gurion University of the Negev, Sede Boqer Campus, 84990 Israel

**From 16 November 2009 to 31 May 2010:** Master thesis at the

---

Helmholtz-Zentrum Berlin für Materialien und Energie

**From 4 August 2008 to 26 September 2008:** International Summer School for Materials and Energy Research at the Helmholtz-Zentrum Berlin für Materialien und Energie